EUROPEAN ORGANIZATION FOR NUCLEAR RESEARCH

CERN-SR-XXX

March 21, 2017

Yearly progress report on WA105/ProtoDUNE dual-phase (2017)

The ProtoDUNE Dual Phase Collaboration

Abstract

WA105/ProtoDUNE dual-phase aims at fully demonstrating the concept of a very large dual-phase LAr TPC and calibrating it with a charged particles test beam, in view of the application of this detector design for the construction of DUNE 10$kton$ far detector modules. In this document we report the general progress of the dual-phase experimental activities at CERN since the last SPSC yearly report.

Contents

1 Introduction

As reported in the 2016 WA105 SPSC report, the construction and operation of the large WA105 dual-phase detector in EHN1 became, at the end of 2015, officially an integral part of the DUNE project. This technology is considered by the DUNE collaboration as directly relevant for the instrumentation of the 10kt detector modules to be installed in the SURF (Homestake, South Dakota) underground laboratory.

A complete symmetry between ProtoDUNE Dual-Phase (ProtoDUNE DP) and Single-Phase (ProtoDUNE SP) was then established in the management structure of DUNE. The single-phase and dual-phase prototyping efforts were organized in parallel coordination structures since December 2015 and an EOI call was organized within DUNE in order to integrate new groups willing to join these prototyping activities. New groups, also from the US, have been joining Dual-phase ProtoDUNE and contributing significantly during this last year to the detector construction and software and analysis efforts. Several synergies between single and dual-phase ProtoDUNEs were in addition identified during 2016 and are now firmly established for mutual benefits on the construction and operation efforts of the two detectors. These synergies concern the beam plug, beam-line instrumentation, high voltage, field cage, slow-control, online and offline processing. They brought to the definition of a common working groups and of a common environment. ProtoDUNE-DP has been developing a field cage design which, although having a different geometry and requirements, is based on the same basic structural elements as the single-phase field cage design. Similarly ProtoDUNE-SP benefited of components predefined in the DP developments such as the High Voltage system and the slow control system.

The full integration in the DUNE collaboration had direct implications on the $6 \times 6 \times 6\mathrm{m}^3$ design which was optimized, with respect to the original WA105 TDR design, in order to make it as much as possible representative of a full scale test of the DUNE 10 kton dual-phase module design (see Figure 1) as described in the DUNE Conceptual Design Report Volume 4 [1].

The DLAr and the dual-phase $10kton$ detector are expected to share the same detector elements, in particular the $3 \times 3\ m^2$ Charge Readout Plane modules. This process of integration in DUNE impacted as well the assembly procedure of DLAr adopting a construction procedure and a definition of the basic detector elements to be prefabricated and transported to the final assembly as close as possible to the one which will be used for the underground construction of the $10kton$ detector at SURF by exploiting a Clean Room Buffer attached to the cryostat Temporary Construction Opening. This effort will allow performing a full assessment of the final DUNE $10kton$ detector construction chains and of the related QA/QC procedures.

The main goal achieved by the end of November 2016 was the completion of the executive mechanical

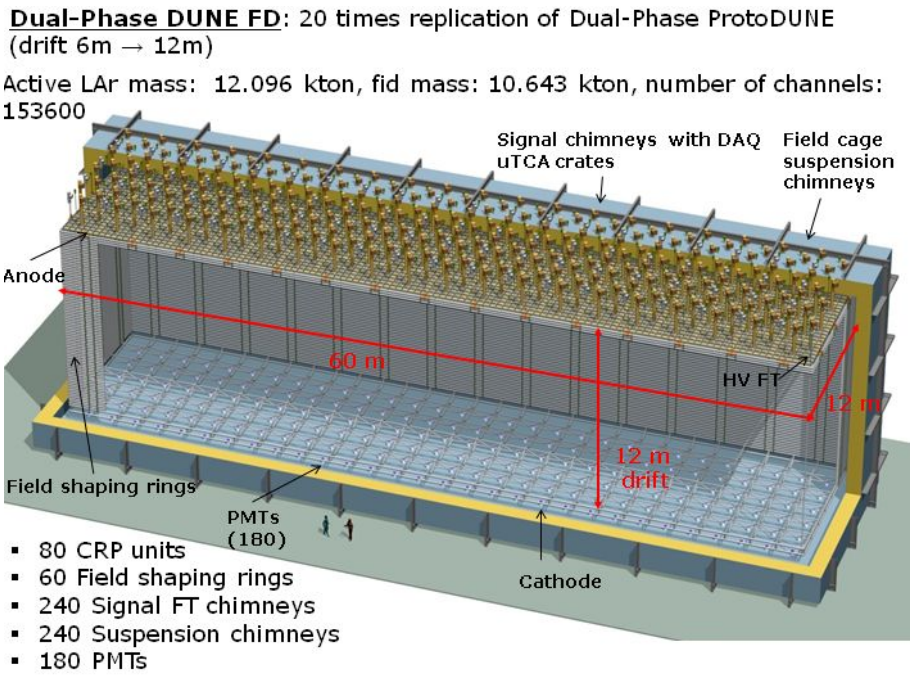

FIG. 1: The 10 kton dual-phase module for DUNE.

design of the $6 \times 6 \times 6$ m^3 detector corresponding to this final configuration optimized for DUNE. This process concerned three main detector elements: the 3 m^2 Charge Readout Planes, the Field Cage and the cathode.

Other detector elements largely benefited from the construction activities benefited of the experience acquired with the LAr-Proto detector in building 182 during 2016 and the related QA/QC test chain. The LAr-Proto detector allowed for the implementation of a subset of the full FE electronics, DAQ and online processing chains and for a full prototyping of the following critical elements: the slow control system, CRP motorization, signal chimneys, HV system and HV feedthrough and of the other feedthroughs. An important milestone in 2016 was the achievement of $300kV$, the nominal working voltage for the $6 \times 6 \times 6$ m^3 detector, in a dedicated test setup including the final HV power supply and HV feedthrough. This feedthrough has been then deployed on the LAr-Proto detector.

The $3 \times 1 \times 1$ m^3 detector was assembled in the Spring 2016 and then inserted into the cryostat in July 2016 for an expected operation during the fall 2016. The related large progress in the detector construction and commissioning is fully documented in this report. Due to delays in the installation and commissioning of the cryogenic system and to an unexpected formation of external ice that was observed on the cryostat during its cool-down, the $3 \times 1 \times 1$ m^3 could unfortunately not yet be filled with liquid argon. We expect further progress on the detector commissioning to remain stalled until the cryostat and cryogenic issues are resolved. The complete list of issues postponing the detector commissioning, some of which were already reported to the SPSC in October 2016 and in January 2017,

are recalled in the LAr-Proto section together with the most recent ones affecting the commissioning of the nitrogen cryogenic line and related to the (so far unsolved) formation of the cold spot with presence of ice in a corner of the cryostat exoskeleton.

Meanwhile the construction of EHN1 extension has been completed, the dual-phase cryostat exoskeleton has been built and the installation of the insulation panels started. The cryostat should become eventually available to start the detector installation by the beginning of June 2017. The infrastructure in EHN1 is in an advanced state of preparation. The beam-line design and of its instrumentation has been completed and moved to construction phase. Full simulations of the final configuration have confirmed the fluxes which were used in order to formulate the beam requests of the 2016 SPSC report. We therefore reiterate those requests for the 2018 beam time, as they were originally presented in the 2016 report and have been kept unchanged for this report.

The ProtoDUNE-DP schedule has been revised by taking into account the updated situation concerning the foreseen accessibility of the cryostat by June 2017 and the availability of ICARUS clean room in building 185 by the beginning of April 2017. The information from the executive design of the detector elements, the experience acquired during 2016 in dedicated tests and in the LAr-Proto construction and in its commissioning, have been integrated as well in the re-evaluation of the schedule and associated resources. Construction and procurement activities for the $6 \times 6 \times 6\ m^3$ already started for the HV system, Front-End electronics, DAQ, Online processing, and photomultipliers. Construction activities for the CRP, field cage and cathode are starting. The updated schedule foresees the end of the detector installation by February 2018.

Large progress was made as well on the software and analysis activities and from the implementation and commissioning of a subset of the online storage/processing farm for LAr-Proto. These activities are documented in the last section of this document.

2 General organization of the Collaboration

Since the last SPSC report of April 2016, the WA105 Experiment has been fully integrated in the DUNE organizational structure as ProtoDUNE Dual Phase (ProtoDUNE-DP). Several new institutions have joined the experiment, increasing the number of collaboration institutes from 15 institutions including CERN from 7 Countries to 22 institutions including CERN from 10 Countries. See Figure 2. The Spokesperson of the experiment is André Rubbia (ETHZ, Switzerland). Each institution is represented in the Institutional Board, chaired by Thomas Patzak (CNRS/IN2P3/APC and University of Paris Diderot). The overall management of the experiment is ensured by the Executive Committee. EC members are: André Rubbia (ETHZ, Switzerland), Dario Autiero (CNRS/IN2P3/IPNL, France), Dominique Duchesneau (CNRS/IN2P3/LAPP, France), Jae Yu (UTA, USA), Jukka Maalampi (Univer-

sity of Jyväskylä, Finland), Mario Campanelli (UCL, UK), Sebastien Murphy (ETHZ, Switzerland); Takuya Hasegawa (KEK, Japan) and Thomas Patzak (CNRS/IN2P3/APC and University of Paris Diderot). The contributions of each institution belonging to WA105 have been defined and agreed in details. The overall funding situation presently adequately covers the anticipated needs of the experiment.

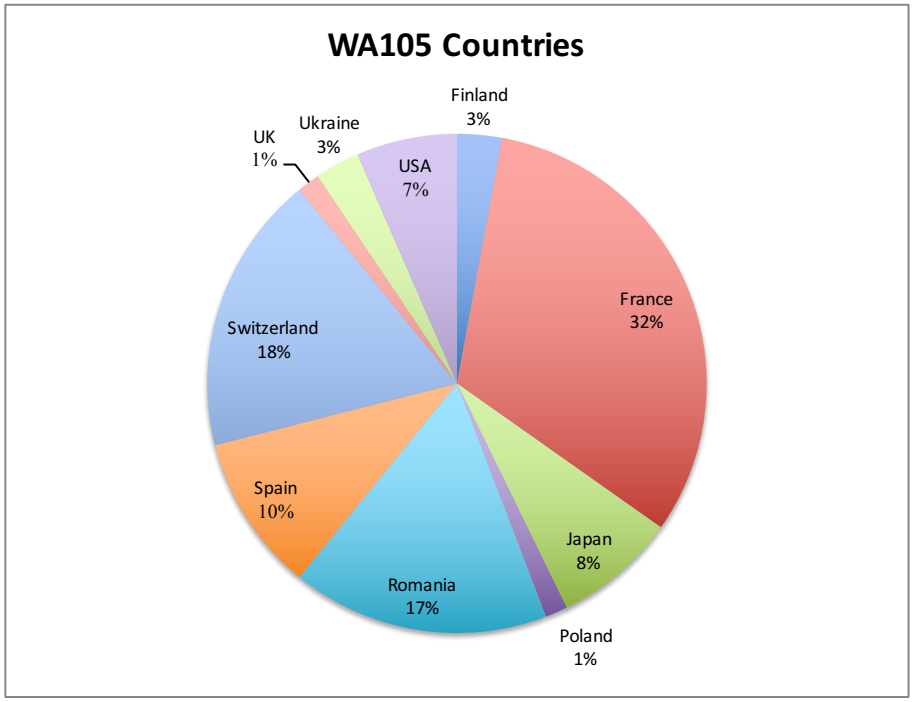

FIG. 2: Man-power by Country except CERN of the WA105 Collaboration 2017.

As of February 2017 the WA105 Collaboration is composed of 22 institutions including CERN from 10 Countries:

CEA/IRFU, France; CIEMAT, Spain; CERN, Switzerland; CNRS/IN2P3/APC, France; CNRS/IN2P3/IPNL, France; CNRS/IN2P3/LAPP, France; CNRS/IN2P3/LPNHE, France; CNRS/IN2P3/OMEGA, France; ETH Zurich, Switzerland; IFAE, Spain; IFIN-HH, Romania; KEK, Japan; NCBJ, Poland; NIT Kure College, Japan; Princeton University, USA; University College London, UK; University of Bucharest, Romania; University of Bern, Switzerland; University of Iwate, Japan; University of Jyväskylä, Finland; University of Kiev, Ukraine; University of Texas Arlington, USA.

A detailed view of the man-power contribution by Country is shown in Figure 2. The collaboration

has roughly 40% students, postdocs and junior faculty, which shows the large interest for the experiment and the related science as well as the high value of teaching and training for the next generation of physicists.

As mentioned above, the WA105 project is now fully recognized in the DUNE experiment as one of the two prototype efforts towards the deployment of four 10 kt FD detectors at SURF. Within the DUNE management, the ProtoDUNE Dual Phase activities are coordinated by Dario Autiero (CNRS/IN2P3, France) and Takuya Hasegawa (KEK, Japan). Working meetings occur regularly every week, organized by the Technical Board and the Science Board in alternance.

To accomplish the installation of the detector in the North Area and in parallel run the 3x1x1 prototype, the organization of the experiment has been adapted. Two new working groups have been created: The 3x1x1 operations group, coordinated by Laura Molina Bueno (ETHZ, Switzerland) and Laura Manenti (UCL, UK) and the 6x6x6 EHN1 integration group, coordinated by Sebastien Murphy (ETHZ, Switzerland) and Dominique Duchesneau (CNRS/IN2P3/LAPP, France). A detailed view of the organization is shown in Figure 3.

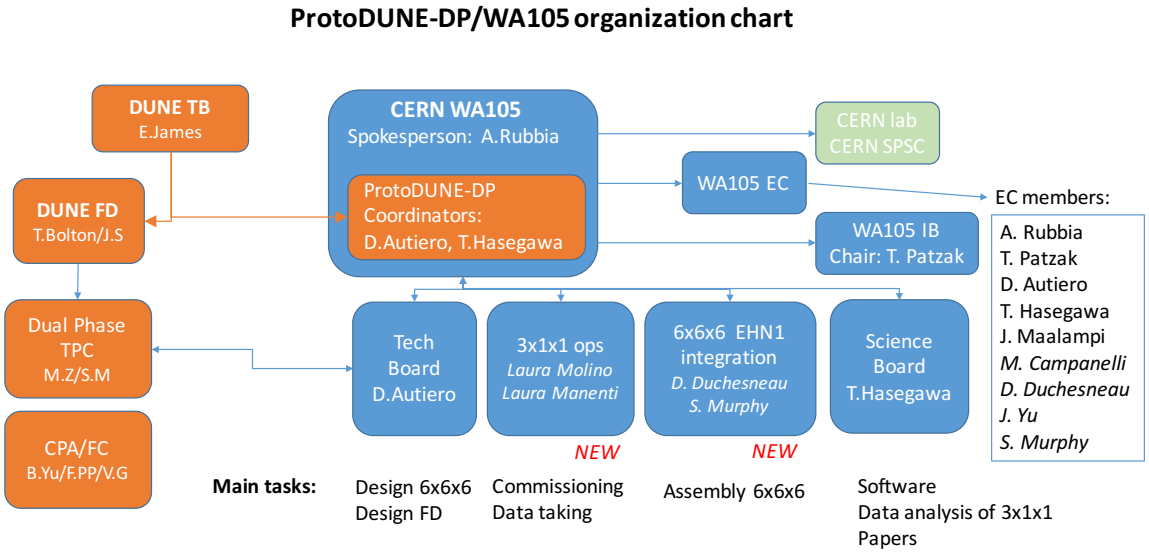

FIG. 3: Organization of the WA105 Collaboration 2017.

3 Status of the 3×1×1 m^3 prototype

A significant effort was deployed in 2016 to successfully complete the installation of the 3×1×1 m^3 prototype. By July 4$^{\text{th}}$ the TPC had been fully constructed and lifted into the cryostat. The second half of the year was dedicated to the installation and commissioning of the cryogenic system by the

CERN Neutrino Platform. The entire setup was effectively ready for start of operations by the end of 2016. The gas argon piston purge started at the end of January and lasted approximately one month until sub ppm levels of oxygen and nitrogen gas were measured inside the tank. The cool down was initiated on February 24$^{\text{th}}$ at a rate of about 2 K/hour. Pictures of the setup in building 182 during assembly and in final configuration are shown in Figure 4.

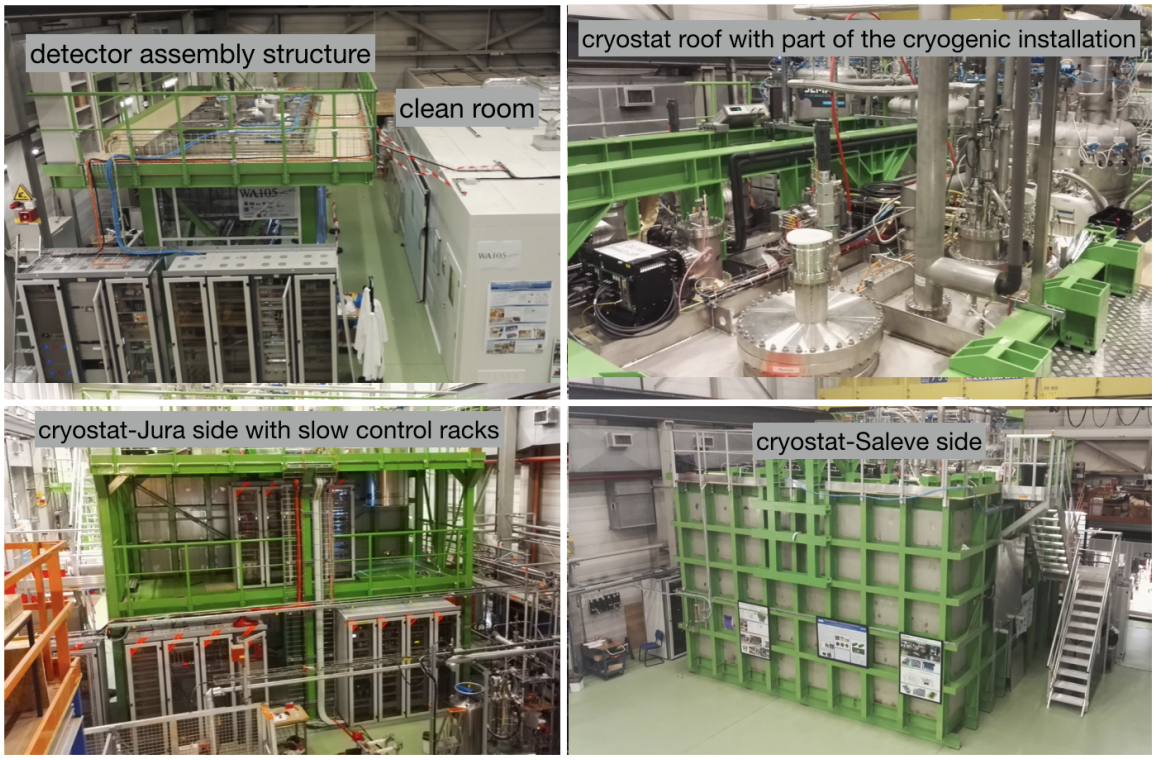

FIG. 4: Overview of the installation in building 182.

One week into the cool down procedure, on March 3$^{\text{rd}}$ a ~30×30 cm^2 formation of ice was noticed on the bottom south east corner of the cryostat outer structure. At that time the minimum recorded temperature inside the tank was about 170K and thermal images of the outer structure indicated coldest spot of -40°C near the center of the iced area. After multiple checks and discussion with GTT experts on site it was concluded there could be a leak from the inner membrane to the insulation space near this corner. Therefore decision was taken to stop cooling and start warming up the tank, in view of an inspection by CERN and GTT. At the time of writing the tank has been warmed up to room temperature, flushed with dry air and the manhole has been opened. Four visits inside have so far taken place in order to perform detailed inspection of the membrane status. This included close visual inspections of membrane panels and specifically the welds, leak testing by injecting Helium gas in the insulation space. We do not have further details at the moment and discussions are ongoing with CERN and GTT experts to understand the reason for this formation of ice on the outer structure.

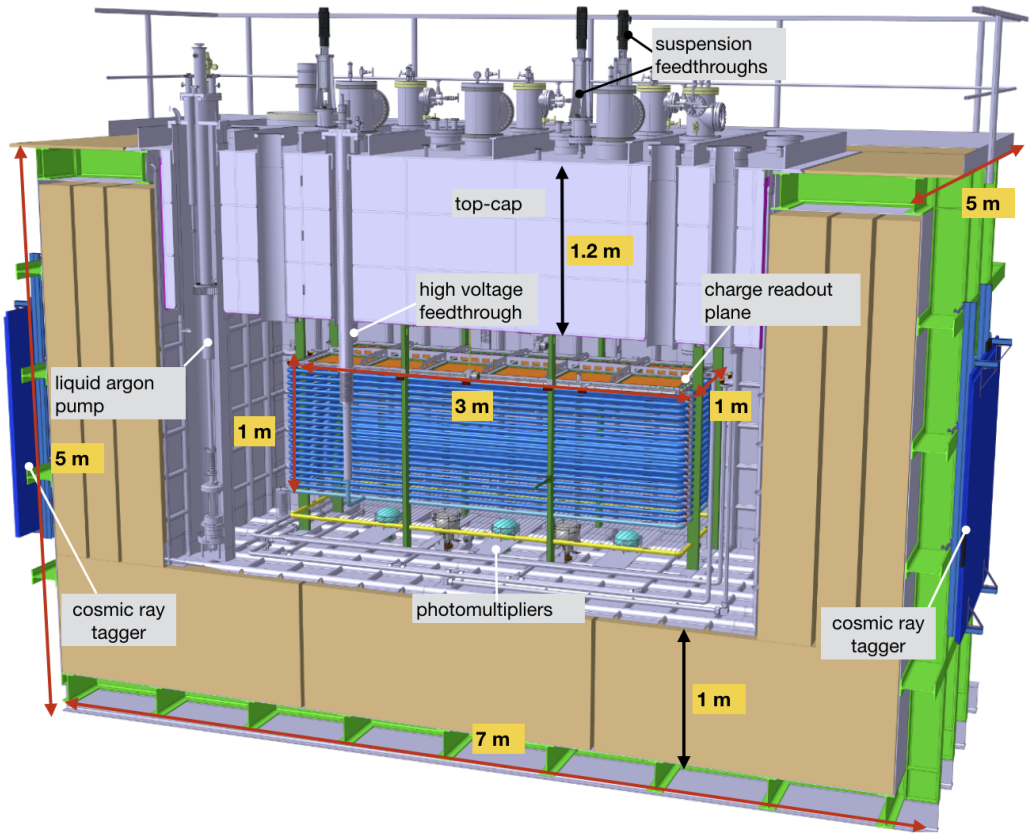

FIG. 5: Overview of the 3×1×1 m^3 detector inside the cryostat.

This incident will obviously impact the overall schedule of the 3×1×1 m^3 operations by several weeks. The construction and installation of the TPC itself went smoothly and according to plan. In this section we will describe in detail those aspects and the large progress made since the last status report [2].

3.1 Overview of the setup

The setup was described in detail in the previous status report [2]. Figure 5 shows an updated illustration of the 3×1×1 m^3 detector inside the membrane tank. The detector consists of a one meter high field cage made of 20 field shapers placed at a constant spacing of 50 mm and a metallic grid cathode. A uniform drift field is provided by a resistor divider chain situated between the cathode and the First (top) Field Shaper (FFS). At the top the drifting charges are extracted into the gas phase where they are amplified and collected in a 3×1 m^2 charge readout plane. Five photomultiplier tubes (PMTs) are fixed under the cathode. To be sensitive to the 128 nm scintillation light from argon, they have been coated with the wavelength shifter tetraphenyl butadiene (TPB). PMTs may provide the reference time for the drift of ionisation charges as well as the event trigger. An external cosmic ray trigger is also given by two 1.8 ×1.8 m^2 scintillating fiber panels fixed on both sides of the cryostat

external structure (more details on this in Section 3.3.3). The two panels are setup in coincidence to collect a sample of quasi-horizontal muons in the TPC. The entire detector is hung under a 1.2 m thick insulating top-cap. The field cage is fixed by eight FR4 bars and the CRP is suspended by means of three adjustable cables inserted in dedicated suspension feedthroughs. The top-cap is part of the cryostat structure providing the functionality of reducing heat input and minimizing the liquid and gas argon convection. The thermal insulation of both top-cap and cryostat is based on GRPF (glass reinforced polyurethane foam) layers, interspersed with pressure distributing layers of plywood. The tank volume should be maintained at a positive pressure with respect to the insulation volume to avoid excessive stress on the membrane layer. This is achieved by a controlled flow of nitrogen gas through the insulation space. Since nitrogen has a lower boiling point than argon, it will not liquefy. In addition it removes the humidity from inside the insulation. The thickness and composition the insulation are designed to limit the residual heat input to less than 5 W/m^2 during cryostat operation. The inside of the cryostat is covered with 1.2 mm thick corrugated steel panels that are precisely shaped to absorb the thermal contractions.

3.2 Summary of the 3×1×1 m^3 construction

The detector construction started at the beginning of 2016 with the assembly of the CRP in the clean room of building 182. The entire CRP was then suspended under the top-cap in a detector assembly structure that was custom built in order to provide a clean environment with sufficient space to construct the entire 3×1×1 m^3 TPC. A subset of the monitoring racks were also positioned and fully cabled to the detector allowing to perform multiple verification and testing at each step of the detector assembly (see Figure 4). This included the verification of the feedthrough electrical connections, adjusting the CRP height and calibrating the motorisation, checking the high voltage contacts as well as most of the instrumentation including temperatures sensors, cryo-camera image, level meters and heaters (these tests were also repeated later once the whole detector had been placed inside the cryostat).

The detector assembly effectively ended on July 4$^{\text{th}}$ 2016, date at which the entire detector suspended under the top-cap was lifted from the assembly structure and inserted in the cryostat. Once in place the detector inside the cryostat was accessed when needed through the 600 mm diameter manhole in order to finalise some electronic connections, make dedicated surveys and perform visual checks. Picture of the detector inside the tank are provided in Figure 6. The second part of 2016 was mainly dedicated to the installation by the Neutrino Platform of the cryogenic system as well as the installation and commissioning of the charge readout DAQ. Table I summarises the main milestones

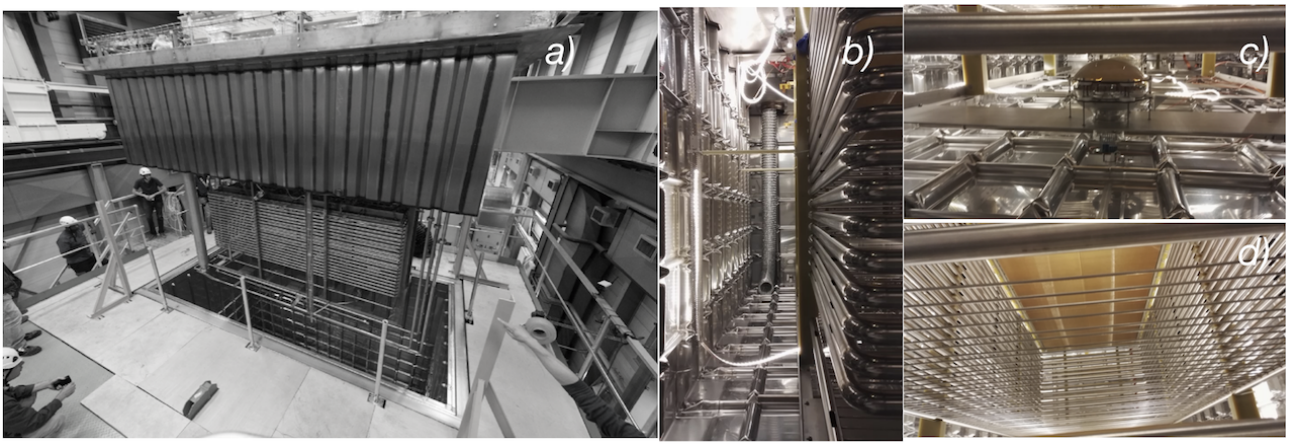

FIG. 6: a) Top-cap being inserted in cryostat; b) west side of the field cage inside the cryostat; c) one of the PMTs installed on the bottom of the tank; d) view of the cathode grid and field cage from bottom to top.

of the 3×1×1 m^3 construction.

During the assembly process many individual components were stress-tested to ensure optimal operation at cryogenic temperatures. This included for instance shock cooling the entire Charge Readout Plane (CRP) in an open cryogenic bath. An important point is that most of the detector parts are either identical or smaller scale versions of those that are about to be installed on protoDUNE-Dual-Phase. In particular the high voltage and signal feedthroughs, the CRP suspension system, the slow control sensors and their acquisition racks, the charge readout front end electronics, and the data processing farm. From that perspective, all the tests performed during the 3×1×1 m^3 assembly have enabled us to fine tune or optimise the design of larger detectors.

3.2.1 Assembly of the 3×1×1 m^3 TPC

Pictures of the TPC installation are shown in Figure 7. The TPC is essentially composed of two independent structures: the charge readout plane and the drift cage, the latter being composed of the field shaping rings, the cathode, the ground grid and the PMTs fixed underneath. The CRP is the most delicate component of the detector to assemble. Its role is to efficiently extract the drifting charges from the liquid to the gas phase, multiply them in the Large Electron Multipliers (LEMs) holes and collect them on a two dimensional anode. The electric field to extract the charges is provided by an extraction grid placed 1 cm below the LEMs. The CRP therefore consists of the 2D anodes, the LEMs and the extraction grid assembled with precisely defined inter-stage distances and inter-alignment. The extraction grid is made from 100 micron diameter wires matching the readout pitch of 3 mm and tensed across the 3×1 m^2 area of the CRP. The anodes and LEMs come in individual units of 50×50 cm^2 PCBs. Twelve of each are precisely positioned on the frame to provide a fully active amplification and readout area. Both the anodes and LEMs are rather standard printed circuit boards (PCBs) that can easily be

Period	Activity
January 2016	Successful high voltage test on an individual 50×50 cm^2 LEM in ultra pure argon vapor at 87 K. Detector assembly structure ready
February	Thickness measurement, QA/QC and selection of 12 LEMs for installation on CRP. Top-cap arrives at CERN and installed in detector assembly structure.
March	CRP fully assembled in clean room, flatness measurement. Signal feedthrough blade insertion successfully tested.
April-May	Cabling on top-cap and insertion of most feedthroughs. CRP suspended under top-cap. liquid nitrogen bath test of the CRP. Cabling all CRP to feedthroughs and test of HV contacts along with some instrumentation.
June	Installation of drift cage and cathode. Installation of photomultiplier tubes and testing response in dark boxes. Membrane cryostat leak testing finished; inside of tank fully cleaned.
July-August	Lifting of detector from assembly structure to cryostat. First entry through manhole and visual check + survey of detector inside tank. 300 kV high voltage feedthrough delivered and test inserted. Insertion of first front end amplifier cards and test of electronic noise with oscilloscope. Move and re-cable racks in final position.
September	All instrumentation (cameras, level meters, temperature..) operational and recording data successful test of the 300 kV feedthrough in separate setup. Installation of the CRT panels. Start assembly of cryogenic system.
October-November	Installation of entire DAQ and data processing farm; first recording of noise with complete system.
December	System ready for commissioning, first pressurisation of the tank to 1000 mbar and leak checking.

TABLE I: Detector installation schedule under the temporary assembly structure in 2016.

mass-produced in the industry at affordable costs. Their design is the outcome of many years of R&D and is well documented in literature [3, 4]. Furthermore their quality assurance process is well under control as reported in previous status reports [2, 5]. Once the LEMs and anode have been cleaned and selected they are assembled as individual 50×50 cm^2 modules with 29 precisely machined spacers to guarantee a uniform 2 mm gap between the LEM and anode. The modules are then fixed on the CRP frame. During this process the CRP is laying on a flat optical table inside the clean room. The frame is then suspended above the table and the extraction grid is installed. For ease of installation the grid comes as group of 32 wires pre-soldered under tension on specifically designed PCBs. The PCBs are then fixed one by one on the frame and their tension can be individually adjusted to provide a uniform plane of wires 1 cm under the LEMs. The flatness of the CRP is surveyed in the clean room with the frame suspended above the optical table. Once fully assembled the CRP is brought inside the detector assembly structure and suspended under the top-cap via cables controlled by three motorised feedthroughs. The role of those feedthroughs is to precisely adjust the height of the CRP to the liquid

FIG. 7: Main step of the detector assembly. The CRP is first assembled in the clean room (a) then suspended under the top-cap with the motorised suspension feedthroughs *(b,c)*. The CRP underwent a shock cryogenic test in liquid nitrogen bath *(d)* and lifted back into nominal position so that the drift cage and other detector components could be installed *(e,f)*.

argon level during operation. Before assembling the drift cage, the fully assembled CRP with some of the electrical connections is dipped in an open bath of liquid Nitrogen to verify that (1) no grid wires may rupture due to the thermal stress, (2) the mechanical tolerances of flatness are respected in cold, and (3) that the electrical contacts of the anodes hold at cryogenic temperatures. The mechanical tolerance on the flatness was performed employing photogrammetric techniques by the CERN survey group, the test was successful and the results from the survey are reported in [6].

The CRP is lifted back into nominal position to allow installation of the drift cage along with the cathode and grounding grid. The process is rather straightforward. The final step consists in fixing the five photomultiplier tubes (PMTs). The PMTs are coated with TPB wavelength shifter, three of them directly on the glass and for the other two the TPB is evaporated on a circular PMMA window placed a few mm above the PMT. Two types of electronic circuits are employed: three PMTs are biased with negative high voltage and have a separate signal cable and the other two have one single cable where the signal is decoupled from the high voltage outside of the cryostat. The latter design is the one that will be employed for protoDUNE-Dual-Phase. The coating and testing of their quantum efficiency was performed in 2015 at the CERN thin film laboratory. They were subsequently shock cooled in liquid nitrogen and tested at room temperature in gas argon.

Once installed under the grounding grid, the PMTs are electrically connected and their response is again tested by covering them and measuring their dark current rate. The electrical contacts and leakage currents of all high voltage components is also tested; this includes the LEMs, the extraction grid, the drift cage divider and most of the slow control instrumentation (temperature probes, cameras, level meters,..).

3.2.2 Assembly and test of feedthroughs

In parallel to the TPC construction lots of activity took place above the top-cap to test and insert all the feedthroughs. The feedthroughs are crucial components that serve as interface for signal, high voltage and slow control sensors between the inside of the detector and the experimental acquisition. They are all situated on the top-cap and have to at least penetrate the 1.2 m insulation thickness to reach the various parts of the detector (see Figure 5). Almost all the feedthroughs installed in the 3×1×1 m^3 are based on innovative concepts, they have been tested during assembly and commissioning and their design will either be copied or scaled up for future detectors. Since the requirements on vacuum tightness, high voltage breakdown limits, cryogenic compatibility, are stringent most of them had to be custom designed in close collaboration with industry. As example we show in Figure 8 a picture of the high voltage feedthrough and of one of the signal feedthroughs.

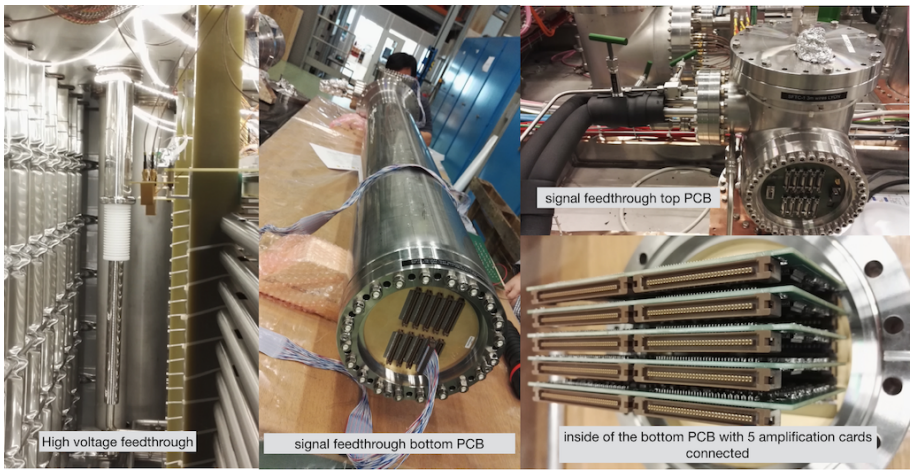

FIG. 8: The 300 kV high voltage feedthrough connected to the cathode of the detector inside the cryostat (left). A complete view of a signal feedthrough (middle) and close up pictures showing the top part of the feedthrough as well as the inside of the bottom PCB with the preamplifier boards connected.

The role of the high voltage feedthrough is to safely guide the high voltage from the power supply cable to the cathode of the detector. It requires a very careful design and precise manufacturing to minimise all local electric fields in argon and to keep its heat input to a minimum to avoid formation of bubbles. The prototype that is installed in the 3×1×1 m^3 was manufactured by the company CINEL Strumenti Scientifici s.r.l. Last September it was successfully tested up to -300 kV in pure argon in a dedicated setup [7]. The ability to withstand a voltage of 300 kV was guided by the requirements of being able to provide a feedthrough for 6 meters drift in the $6 \times 6 \times 6$m^3 detector. For the 3×1×1 m^3 the feedthrough will be operated at about 50 kV and will provide feedback on its long term stability.

An excellent signal-to-noise-ratio is crucial to reach the required physics performances and fully exploit the imaging capabilities of the TPC, especially for the low energy neutrino physics. In this

context an innovative design of signal feedthroughs will be tested. They allow to place the amplification stage close to the anodes, thereby also profiting from the cold environment, while still being able to extract the boards for maintenance without accessing the main vessel. Each feedthrough reads out 320 channels and consists of a ~ 2 m long stainless steel "chimney" sealed on both ends by circular multilayer printed circuit boards (PCBs) with connectors welded on both sides. The PCBs are carefully designed to provide ultra-high vacuum leak-tightness. The bottom PCB serves as interface between the connection to the anode and the five amplifier boards located inside the chimney. Each board is guided from the top thanks to specially designed FR4 blades. A complete insertion of the blade guaranties that the amplifier board is electrically connected to the bottom PCB. The top PCB then serves as interface between the amplified signals and the digital electronics located on top of the cryostat.

3.2.3 Slow control sensors

The slow control system for the 3×1×1 m^3 detector is part of a continued progressive prototyping effort aiming at developing a system dedicated to multi-kton liquid argon double phase detectors. It provides precise monitoring of temperatures, pressures, high voltages and liquid argon level. Innovative developments include the construction of very precise level meters, a motorised suspension system capable of adjusting the CRP frame with a sub mm precision, special thermometers to measure temperature gradient in the gas phase, and custom made cryogenic cameras. The cryogenic cameras are

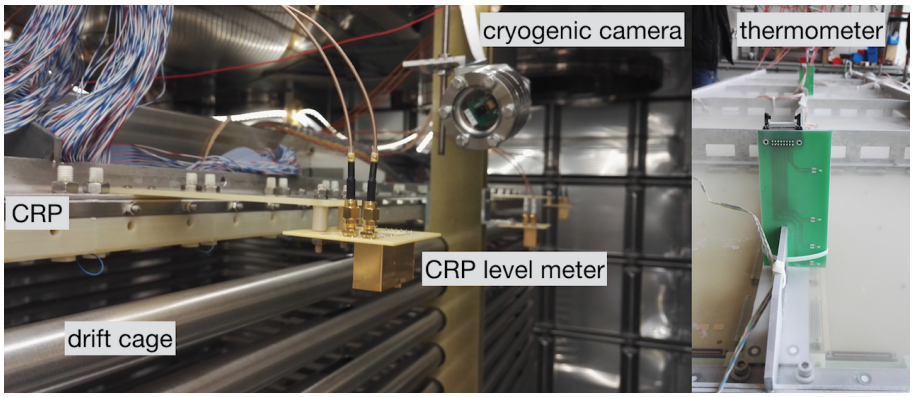

FIG. 9: Left: picture of the top of the 3×1×1 m^3 detector inside the cryostat. The CRP and part of the drift-cage along with some slow control sensors are clearly visible. Right: picture of a thermometer during an open cryogenic bath test of the CRP-frame

essential parts as they provide a direct view during operations and are useful for instance to monitor the level and stability of the liquid argon level. A picture of some of the sensors installed in the 3×1×1 m^3 is shown in Figure 9. The monitoring system has been developed in collaboration with CERN, a reliable and cost effective solution has been found by using National Instruments modules mounted in standard experimental racks. This system is fully scalable to meet the needs of future larger detectors.

The CRP has to be precisely positioned so that liquid level is right in the middle between the extraction grid and the bottom electrode of the LEM. For that purpose eight parallel plate capacitors are installed on the CRP and another six on on the drift cage. The level meters and their electronics were custom designed and manufactured. The electronics board which convert the level meter capacitance to a 0-10 V value are modular and can be fitted in standard NIM crates. They are coupled to the motorised suspension system which acts to adjust the CRP position. The entire system (level meter resolution + motors) allows to adjust the CRP to the liquid argon level with a precision of about 100 microns.

3.2.4 Installation of cryogenic system

The principal goal of the cryogenics system during the detector operation is to safely condense the boiling-off gas and simultaneously provide purification to both the gas and liquid argon phases. A liquid argon purity better than 0.1 parts-per-billion (ppb) oxygen equivalent is required to achieve an electron lifetime better than 3 ms. At a drift field of 500 V/m, the electron drift time in the 3×1×1 m^3 is 0.63 ms. The 3 ms electron lifetime corresponds to a maximal charge attenuation of 20% over a 1 m drift length.

Due to the non-evacuable properties of the membrane cryostat, a specific system was designed to remove the air, provide uniform cooling down, and efficiently recirculate gas and liquid argon while keeping the inner cryostat close to the ambient atmospheric pressure. A picture of the cryogenics setup is shown in Figure 10 and the piping and instrument diagram (P&ID) is available on CERN-EDMS [8]. The external and proximity cryogenic system is under the responsibility of CERN while all cryogenic parts inside the detector cryostat are provided by the experiment. For the 3×1×1 m^3, the experiment is also responsible for the liquid argon recirculation pump due to limited resources from CERN. The pipes handling liquid argon/nitrogen and cold argon/nitrogen gas are vacuum insulated to reduce the heat input by convection and covered with multilayer insulation (MLI) to minimise radiation heat transfer. By design, the cryogenics system groups multiple valves and pipes into cold boxes with common vacuum insulation. Such a vacuum vessel is called a valve box. In total, there are 4 valve boxes:

- **The condenser valve box (CVB).** The CVB contains a condenser to condense the boil-off argon gas coming from the liquid argon cryostat and from the purification process. The total heat load from the membrane tank, the pipes entering the liquid argon from outside the tank and the vacuum insulated transfer pipes is around 700 W (see Section 3.3.2). The CVB is designed to deliver a maximal cooling power of 10 kW, via a liquid nitrogen heat exchanger. The cooling

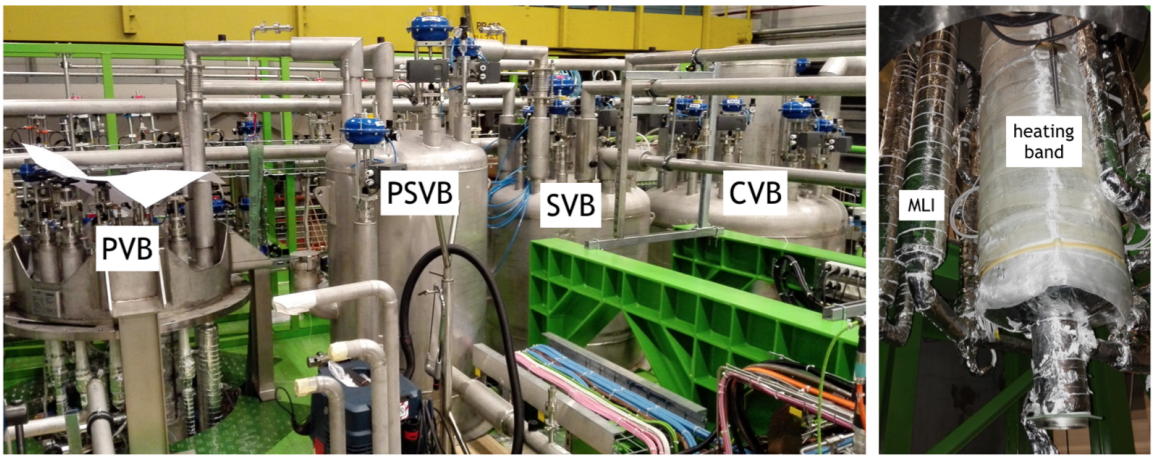

FIG. 10: Left: picture of the four valve boxes; right: internal view of the PVB, the purification cartridge is surrounded by a heating band for the regeneration of the filters.

power of the heat exchanger is controlled by setting the temperature and pressure of the liquid nitrogen. The different flows in the valve box are regulated with the help of seven pneumatic cryogenic valves.

- **The phase separator valve box (PSVB).** The PSVB contains a phase separator to separate the gaseous and liquid argon after purification. The liquid argon returns to the cryostat, while the gaseous argon goes to the condenser where it is re-condensed. To handle the argon flow under the different process conditions, the argon circuit in this valve box is equipped with a phase separating volume and three pneumatic cryogenic valves.

- **The purifier valve box (PVB).** The PVB contains a purification system to purify the liquid argon. The purification is based on copper pellets[1] to remove the oxygen: O_2+2Cu→2CuO and molecular sieve[2] to remove the water by physical absorption. The regeneration of the filters is based on the reaction: CuO+H_2 →Cu+H_2O which takes place at around 200C. To regenerate the purification system, the valve box is equipped with regeneration gas inlet and outlet process pipes. To arrange the argon flow under well-defined conditions, the argon circuit in this valve box is equipped with six hand valves. Figure 10-right shows the internal purification vessel equipped with a heating band and other process pipes surrounded with MLI.

- **The simple valve box (SVB).** The SVB contains pipes to regulate nitrogen and argon flows. For this reason, the SVB is equipped with five pneumatic cryogenic valves.

[1] BASF CU 0226 S 8x14MESH
[2] BASF 4A 8x12 mesh

The overall cryogenics system can be sub-divided into systems that perform specific tasks during each stage of the operation. There are three major tasks and thus three sub systems that are discussed below.

The Purge and Gas Purification system. The objective of the purge system is to remove the air from the tank and fill it with pure argon gas. This is performed by distributing the pure argon gas through a manifold of 4 pipes with 3 holes each placed at the bottom of the tank as shown in Figure 11-left. The exhaust gas is vented to the air through a non-return valves preventing air back flow. During the purge process, the gas impurities are continuously monitored and recorded with three trace analysers for oxygen, moisture and nitrogen. The sample gas to the trace analysers is taken with the help of a double diaphragm pump with a maximal capacity of 4.5 l/min. In order to compensate the gas taken by the sampling pump, a make-up gas line to inject pure argon gas through a purifier[3] is introduced. For the gas argon recirculation, a double diaphragm pump[4] takes the gas from the vessel at a speed of 200 l/min, then the gas argon passes through a commercial gas purifier[5] where impurities including H_2O, O_2, CO, CO_2, H_2, etc.. are removed.

The Boiling-Off gas Compensation and Purification system. The system uses the CVB to re-condense the boil-off argon gas. With a heat input of 1000 W during operation, the flow rate is ~150 l/min gas at room temperature. The boil-off gas is pumped by the gas recirculation pump which has a maximal capacity of 280 l/min, sent through the gas purifier before entering the CVB where it becomes liquid argon and returns to the tank through the phase separator. In case of failure of the gas recirculation pump, the boil-off gas can be diverted through an emergency line to reach the CVB. In this emergency scenario however the gas is not purified. Instead of returning to the main tank, the liquid argon is redirected into the pump tower where it is pumped out by the submersed liquid argon pump and purified through the PVB before returning to the tank.

The Liquid Argon Recirculation and Purification system. The LAr is recirculated with the help of a submersed cryogenic liquid pump and gets purified inside the PVB. This pump has a Net Positive Suction Head (NPSH) of only 5 cm which is the required liquid height above the pump impeller. The pump has a maximal flow capacity of 30 l/min and an efficiency of ~ 40% at the maximal flow rate. The pump efficiency is defined as the ratio between the power transferred to the liquid (either in the form of kinetic or potential energy) to the power of the shaft rotation. The motor efficiency is about 90% which is the ratio between the shaft power and the provided electric power. At a flow capacity of 30 l/min, the shaft power is ~440 W. The heat generated by the pump from both the motor

[3] SAES MicroTorr MC400
[4] KNF 0150.1.2 AN.12 E
[5] SAES MicroTorr MC4500

and pump efficiency is ~300 W. At normal operations, the LAr recirculation speed is around ~20 l/min corresponding to 2 volume changes per day. The unique design of the liquid pumping system is that the pump can be extracted from the tank without polluting the main vessel. As seen in Figure 11-right, the whole liquid recirculation system is confined in a 350 mm diameter (DN-350) vessel welded under a 400 mm Conflat flange (CF-400). This DN-350 vessel is inserted into the main tank. The vessel is equipped with 2 long stem cryogenics valves to control the flow of LAr and to equalise the pressure between the pump vessel and the main vessel.

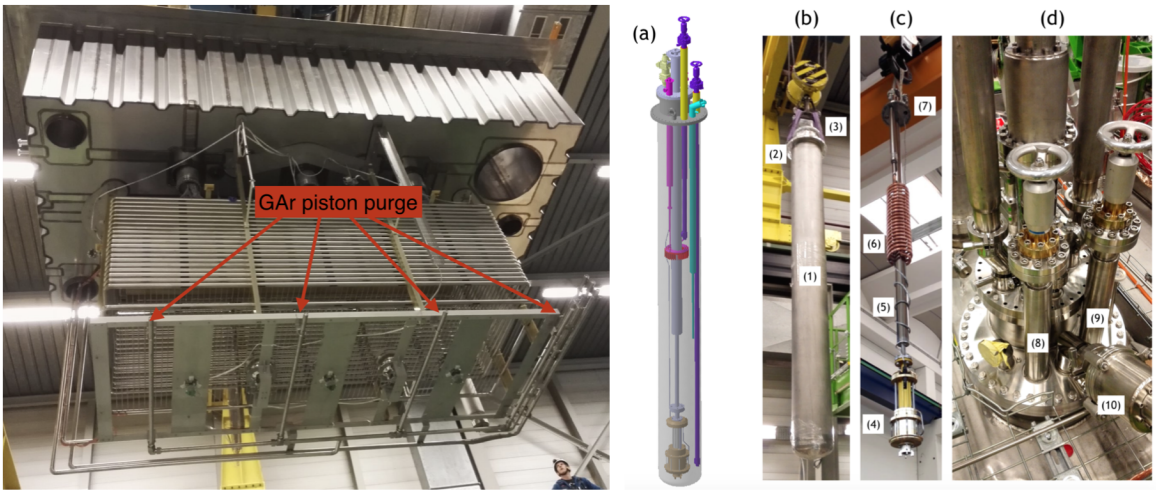

FIG. 11: Left: bottom picture of the detector showing the manifold for the gas argon piston purge. Right: the extractable LAr pumping system: (a) the 3D drawing with the DN350 vessel set as transparent in order the view the extractable part inside; (b) the fixed part with (1) the DN350 vessel, (2) the CF400 flange, (3) the CF250 flange; (c) the extractable part with (4) the ACD TC34.2 LAr pump, (5) the vacuum insulated LAr pipe, (6) the liquid nitrogen heat exchanger, (7) the CF250 flange; (d) the system installed at the main vessel with the cryogenics valve for gas argon (8) and liquid argon (9) and (10) the vacuum insulated condensed liquid argon return pipe from the CVB.

The installation of the cryogenic system was performed in essentially three phases. The first phase which consists in installing all the cold piping was done by an external company (Demaco) selected after an invitation to tender sent by CERN at the beginning of January 2016. The entire cold piping was successfully installed in about 1.5 months in September/October 2016. The second part consists in fixing all the warm piping, this was performed by CERN and a local company. After some delays, which occurred essentially due to late arrival of material, the entire warm piping was finished by the end of November. The last phase was dedicated to installing all the monitoring and process hardware and software (racks, PVSS, cabling,...) as well as performing all the functional and safety tests. To be noted that many activities were performed in parallel, for instance the racks cabling had started in the summer and some testing was also performed during installation of the warm piping. By the end of December the entire cryogenic system was ready.

3.3 Detector commissioning and first performance

Commissioning of the detector started with the cryostat in January 2017 and it has so far consisted of three phases: purging in open loop, purging in closed loop, and cool down. The fourth stage, involving filling, is still to be fulfilled. Details of the cryostat commissioning are given in Section 3.3.1. During the above mentioned stages, several tests were performed to assess the detector was ready for operations. Here we briefly describe the main ones:

- **High voltage (HV) connections:** We have a total of 31 connections, 24 to power the LEMs, five to power the PMTs, one to power on the extraction grid, and one to power the first field shaper (FFS) of the field cage. All of them were tested in gas Argon, when we were in closed loop, before the cooling down of the detector. In particular, after checking the absence of offsets in all the channels of the CAEN power supply unit (PSU), we verified no leakage currents were present on the LEMs.

- **Very high voltage (VHV) connections:** First of all, we verified the absence of leakage current across the field cage divider and on the Heinzinger PSU. Then, a voltage of -2 kV was applied to the cathode through a VHV connection and the current across the field cage was monitored directly on the Heinzinger power supply. The current recorded was as expected at that voltage.

- **Temperature and pressure sensors:** We have a total of 139 temperature sensors: one to measure the ambient temperature, 45 in the insulation, 88 inside the cryostat, and 5 to control the temperature on the heaters located on the charge readout plane. Additionally, we have 8 thermocouples inside each one of the signal feedthrough (SGFT) chimneys. To monitor the pressure we have a total of 15 sensors: six in the insulation space, four in the tank, four in the SGFT chimneys, and an external one to measure the atmospheric pressure. All the sensors were tested and are constantly monitored through a slow control system. We also develop a user-friendly custom-made website[6] (including temperature and pressure sensors, HV connections...) which can be accessed lively by the whole collaboration. This has been equipped with the possibility of making plots for one or more sensors for a user-defined period of time.

- **Cameras:** We have four cameras inside the cryostat, one pointing towards the LEMs and other three directed towards the CRP. Their correct operation was assessed before and during operations. Pictures may be recorded every one minute.

[6] https://wa105data.web.cern.ch/wa105data/

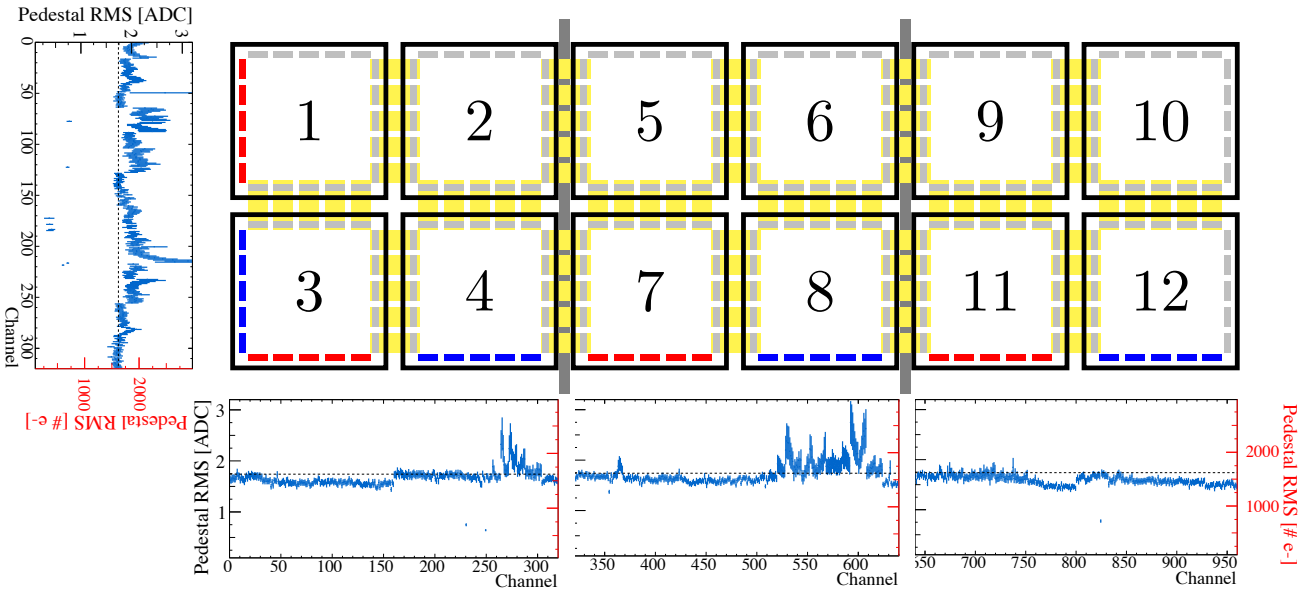

FIG. 12: Noise level in ADC and electrons for each view.

- **Level meters:** We have a total of nine level meters to measure the liquid argon level, of which seven around the CRP, one coaxial capacitive level meter fixed onto the drift cage, and one in the pump tower. All level meters were calibrated in gas argon.

- **Charge readout system:** As previously described in Table I, the DAQ system for charge readout was successfully installed on December 2nd. A pulsing system was also installed on the calibration flange to pulse all the channels on the charge readout plane. We have a total of 1280 channels, 320 per signal feedthrough chimney. In the 3 meter view, called "view 0", we have 320 channels, while along the 1 m view, called "view 1", we have 960 channels. We tested all channels by pulsing them in groups 32 at a time, and we found 35 problematic channels (either dead or showing a lower amplitude than expected) out of 1280. Several campaigns of noise measurements have been regularly performed since July 2016 to address the effect of the different elements on the pedestal RMS value. On February 22nd, we performed the measurements with the detector in its final cabling configuration. The RMS value in ADC as a function of the channel for all the charge readout plane is illustrated in Figure 12.

3.3.1 Start of purge in open and closed loop.

During the first phase of open loop purge, argon gas coming from evaporating the LAr from the LAr tank was introduced to the cryostat through 12 holes uniformly distributed at the bottom of the tank through a manifold as described in Section 3.2.4. In the meantime, the gas was vented directly to the outside. The impurity levels are constantly monitored with the help of the 3 trace analysers

described in Section 3.2.4. The impurities dropped from resp. 6%, 100 ppm (upper measurable range) and 50 ppm (upper measurable range) at the beginning of the open loop to 0.4 ppm, 1.7 ppm and 43 ppm to the end of open loop for resp. oxygen, nitrogen and moisture, as seen from Figure 13.

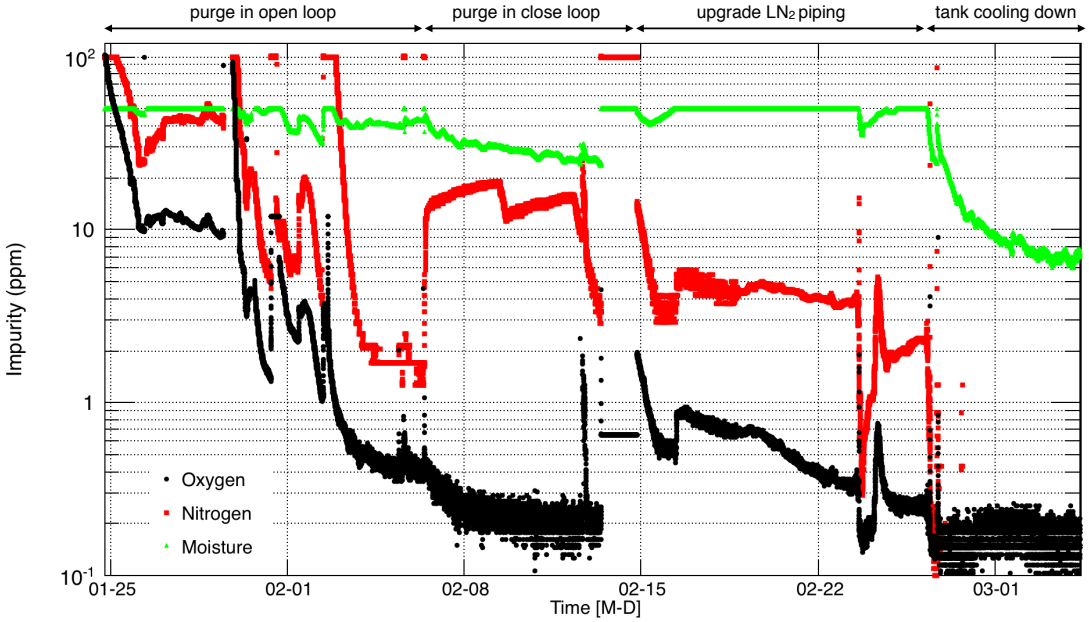

FIG. 13: Impurity evolution with time since starting purge in open loop.

The moisture level is mainly due to out-gassing from the detector components inside the cryostat. The low oxygen and nitrogen levels indicate good tightness of the tank. During the open loop purge, various diagnosis and tests were performed. A leak before the SAES getter was found and repaired close to the end of open loop.

The second phase is to recirculate and purify the gas using the large capacity double diaphragm pump (see Section 3.2.4). The purifier removes oxygen, moisture, but has no expected effect on nitrogen. The impurities dropped to 0.2 ppm and 25 ppm at the end of the closed loop for oxygen and moisture, respectively as seen from Figure 13. From time to time, we injected pure argon gas through the makeup gas line to dilute the impurities. By the end of the closed loop we had reached 3.5 ppm nitrogen.

3.3.2 Start of cooling down: calculated heat input and monitored temperatures.

The cool down of the cryostat began on February 27$^{\text{th}}$ at an initial rate of about 2 Kelvin per hour. Figure 14 shows the evolution of the temperature gradient in gas recorded by a ribbon of sensors placed along the drift cage. The 36 probes spaced ~ 4 cm apart record the gradient over a height of about 1.5 meters.

The cooling down is performed by a mixture of argon gas at 300 K and LAr at 87 K which is injected

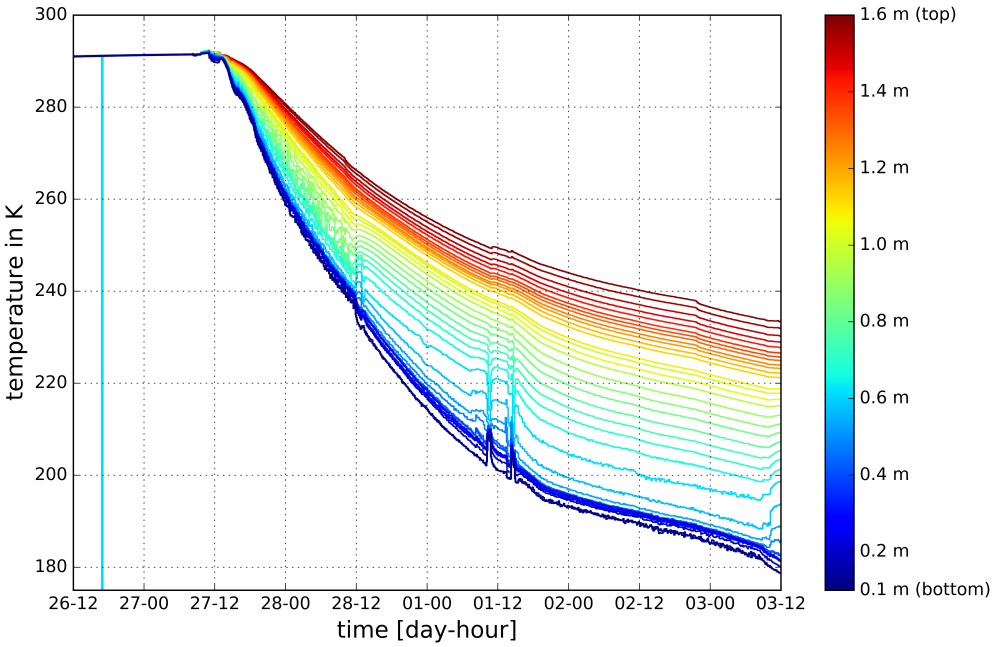

FIG. 14: Evolution of the gas temperature inside the tank during cooling down process. The probes are fixed along the drift cage, the bottom-most probe is located about 10 cm from the membrane floor and the top one is situated just above the CRP.

through four gas atomizing nozzles located at the bottom of the cryostat with flow rates of 500 l/min and 21.1 l/h respectively. This method provides a uniform and steady cooling down by generating a spray of liquid argon, as used at FNAL for the 35 ton cryostat[9]. Sufficient cooling power should be provided to compensate for the total heat input from the detector feedthroughs, electronics, cables and cryostat. The sources of heat input depend on the different phases of commissioning or operation of the experiment. For instance during cool down there is an additional heat load arising from the injection of the warm argon gas through the atomising nozzles. In operation mode this source is no longer present but the operation of the liquid pump generates about 300 W of extra heat input. By design the insulation guaranties a uniform 5W/m^2 on the entire membrane and top-cap surface at liquid argon temperature. The values of the estimated heat inputs during cool down and operation can be found in Table II.

From these values we obtain a total heat transfer during cool down of $\dot{Q}$ = - 1956 W + 14.87 W/K×ΔT. With the simple assumption that the internal energy of the gas inside the tank is proportional to its temperature (which, strictly speaking would only be valid for a constant chemical potential, i.e. the tank can be regarded as a closed system), we obtain the following differential equation:

$$-\frac{d\Delta T}{dt} \propto -a + b \times \Delta T \tag{3.1}$$

Source	Heat input during cool down	Heat input during operation at 87 K
Membrane surface	$0.972\frac{\mathrm{W}}{\mathrm{K}} \times \Delta\mathrm{T}$	200 W
Chimneys	$1.94\frac{\mathrm{W}}{\mathrm{K}} \times \Delta\mathrm{T}$	400 W
Top-cap	$0.29\frac{\mathrm{W}}{\mathrm{K}} \times \Delta\mathrm{T}$	60 W
Wires	$0.028\frac{\mathrm{W}}{\mathrm{K}} \times \Delta\mathrm{T}$	5.8 W
Electronics	0 W	23 W
Pump	300 W	300 W
Warm gas pumped in	$7.1\frac{\mathrm{W}}{\mathrm{K}} \times \Delta\mathrm{T}$	0 W
Evaporation of liquid	- 1344 W	0 W
Warming up of evaporated liquid	$4.28\frac{\mathrm{W}}{\mathrm{K}} \times (\Delta\mathrm{T} - 206\mathrm{K})$	0 W
Total	$-1956\,\mathrm{W} + 14.87\,\frac{\mathrm{W}}{\mathrm{K}} \times \Delta\mathrm{T}$	982 W

TABLE II: Summary of all sources of heat inputs during cool down and operation. ΔT is equal to $\mathrm{T_{lab}} - \mathrm{T_{tank}}$, where $\mathrm{T_{lab}} = 293\,\mathrm{K}$.

with a = 1956 W and b = 14.87 W/K calculated from the values in Table II. The solution to this equation is a bounded exponential function. This calculation is verified experimentally as shown in Figure 15: a plot of the average gas temperature near the CRP during the cool down is fitted with and exponential function. The obtained values from the least squares fit are a = 2472 W and b = 11.03 W/K.

In addition to the temperature in the cryostat, the temperature in the surrounding insulation is also monitored during cool down. The insulation is equipped with 44 temperature sensors, arranged in 3 layers around the tank on all 4 sides as well as the bottom. A plot of the average temperature of all sensors in each layer as well as the minimum temperature inside the cryostat is given in Fig. 16. The average temperature inside the innermost insulation layer steadily follows the inside tank temperature whereas the temperature on the outer-structure stays close to room temperature.

3.3.3 Cosmic Ray Taggers

The Cosmic Ray Tagger (CRT) system is designed to provide a configurable trigger signal from passing-through cosmic muons near horizontal direction with an angular acceptance of ±13.5 degrees in azimuth with respect to the horizon. The CRT consists of two planes fixed on either side of the cryostat external structure walls (see Figure 5). Each CRT plane is composed of two modules providing the particle hit coordinate (x or y). The module contains 16 scintillator strips equipped with wavelength-shifting fibers and Silicon Photomultipliers (SiPMs) for light readout. The CRT plane provides the

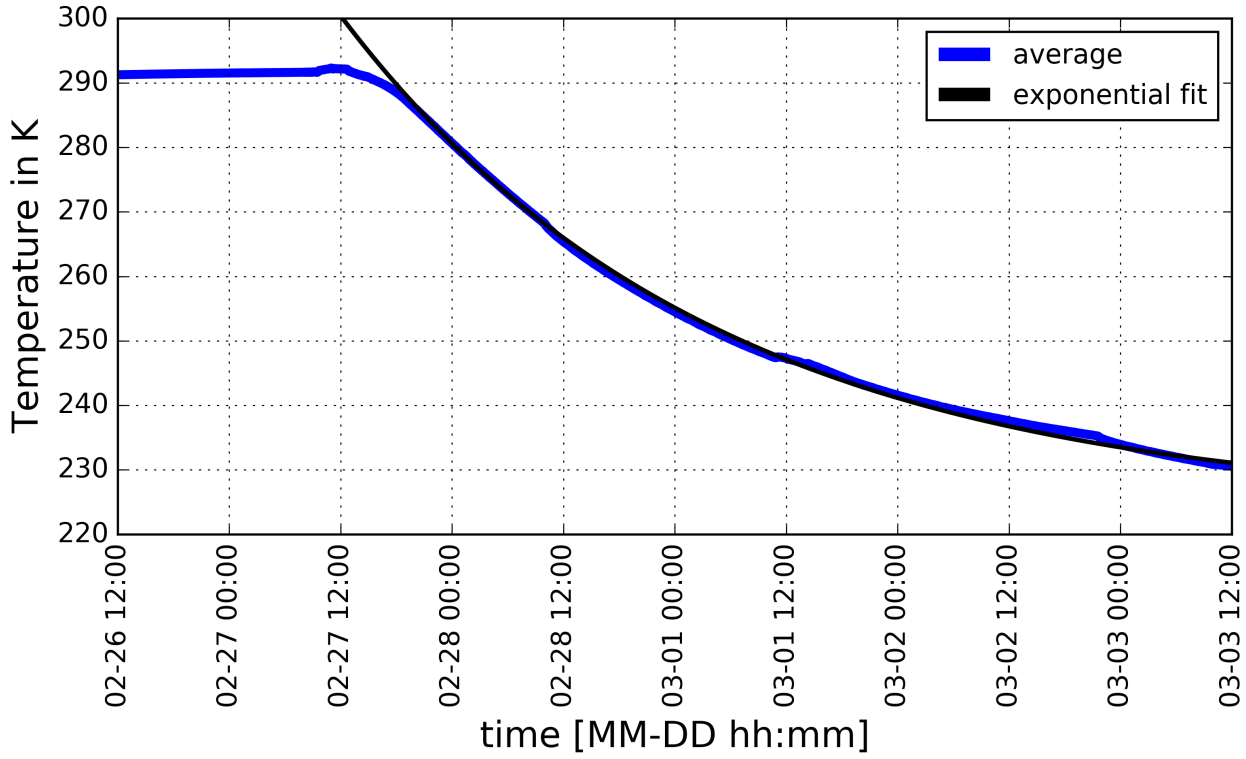

FIG. 15: In blue, evolution of recorded temperatures on CRP during cooling down process; in black, exponential fit.

coordinate of hit in the direction perpendicular to the strip length with the accuracy of ≈1.8 cm RMS. More details on the structure of the modules can be found in [10]. Each scintillating strip is read out by two SiPMs. Their signal is amplified, processed, and digitized by dedicated Front-End Board (FEB), which provides programmable bias, gain, shaping time, and a number of other parameters that ensure an efficient acquisition. The back-end of the FEB is connected to the DAQ computer via an Ethernet daisy-chain. Detailed description of the FEB structure and operation can be found in [11]. When traversed by a muon, each CRT module provides a 160 ns CMOS pulse. The pulses from the four modules are processed and combined into a 500 ns output trigger that is sent to the charge and light data acquisition systems. Both NIM and 3.3 V LVCMOS signals can be provided. The average trigger rate is about 0.3 Hz with the full system activated. For each trigger, the CRT provides information on the SiPM signal amplitudes as well as the absolute timing of the hits with respect to a PPS signal originating from the Caesium GPS-disciplined clock generator. The accuracy of the trigger time stamp is ≈ 3 ns (standard deviation).

The CRT panels were installed on September 6$^{\text{th}}$ 2016 and since then have collected several millions of passing-through muon events. Distinct peaks due to muons going South-North and opposite directions are seen. Coordinate and angular resolution is illustrated in Figure 17, where muon flux from

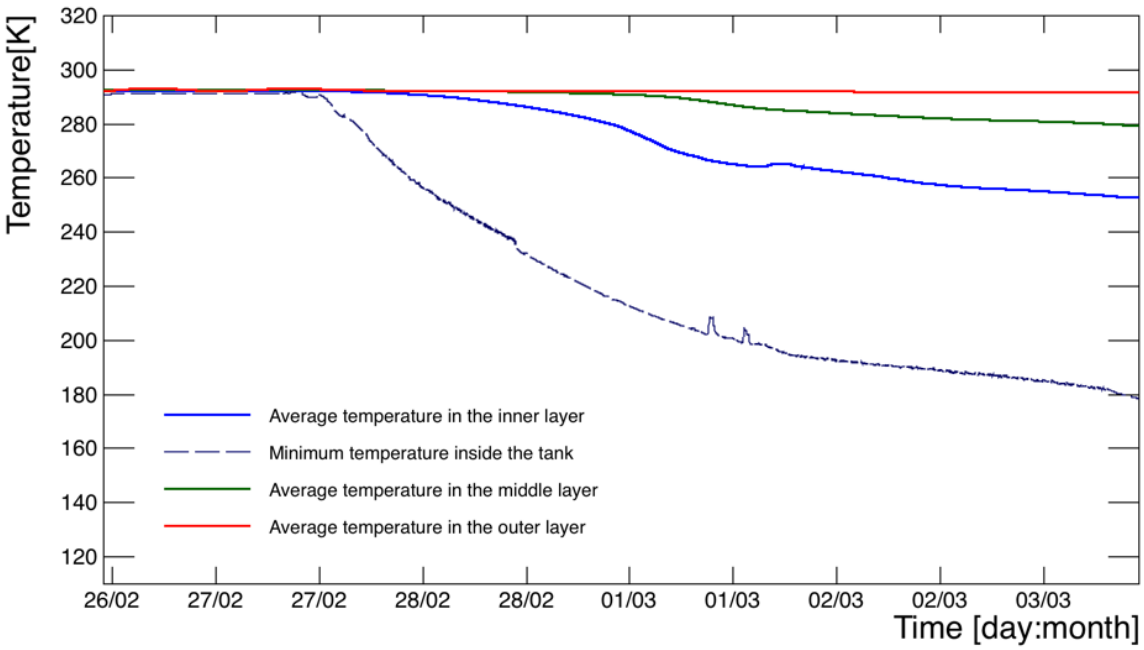

FIG. 16: Evolution of the average temperature in each of the insulation layer surrounding the cryostat during the cooling down process. The probes in the inner layer are located 40 cm away from the membrane, the middle ones 70 cm and the outer ones 100 cm away. The outer ones are thus in direct contact with the outer structure surface.

two opposite directions is shown. The flux is normalized to detector acceptance and elapsed time.

3.3.4 Photomultipliers, light readout DAQ

As already explained, the light readout system for the $3{\times}1{\times}1\,\mathrm{m}^3$ consists in five Photomultipliers (PMTs) installed below the TPC. Their signals are digitized with a CAEN v1720 board readout via optical link to a PC equipped with a CAEN A2818 PCI CARD. The DAQ software is based on the MIDAS framework and runs on the same PC. The board is readout upon receiving an external trigger from the CRT via a LEMO connection. A self trigger on the signal amplitude of one or more PMTs may also be used. In fact, while CRTs are better at triggering long track events, PMTs can provide a separate trigger system for short or stopping tracks. CRT events are retrieved through a socket connection and merged to the PMTs data stream for later use during analysis. In order to prepare the system for commissioning, different tests have been performed during the detector cool down in GAr:

1. Dark pulses have been observed for each PMTs with an oscilloscope for HV values starting from 1000 V.

2. DAQ readiness has been tested in “dry run”, i.e. the with PMTs HV switched off in order to test software stability, fine tune the digitiser parameters, and check noise levels.

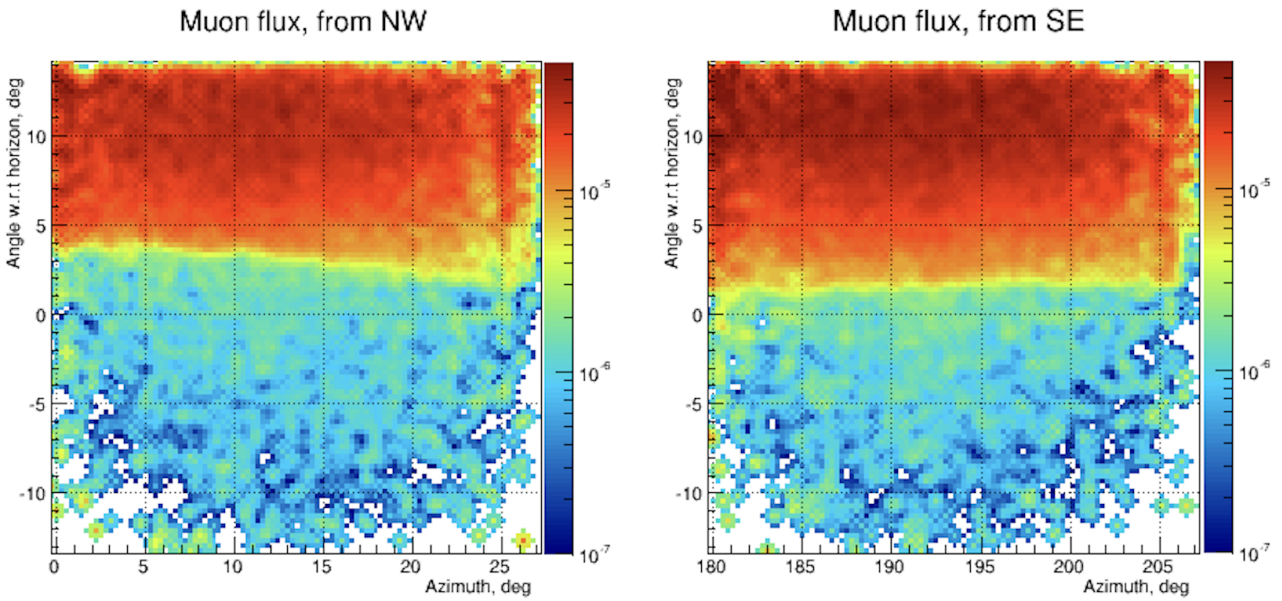

FIG. 17: Normalised muon flux on the two CRT panels in $cm^{-2}sr^{-1}s^{-1}$.

3. A three hour run (3913 events) has been taken with the HV of the PMTs close to the nominal tension to test the PMTs response as well as the external trigger provided by the CRT.

The rate of event readout from the DAQ, upon receiving the CRT trigger, is on average 0.35±0.04 evt/s. This is consistent with the trigger delivered by the CRT, and thus validates the correct distribution of the trigger signal.

The plot in Figure 18 shows an averaged waveform from cosmic muons from one PMT. A few thousand waveforms have been processed in the following way: (1) for each event the baseline is calculated over a pre-trigger region of 400 ns and subtracted to each amplitude sample in the waveform, (2) the waveforms are then averaged. The resulted waveform has been fit with a function that is the sum of a Gaussian, parametrised by t_0 and σ, and three exponential, with decay time constants τ_1, τ_2 and τ_3, and normalisation factors A, B and C. The three decay constants correspond respectively to a fast, an intermediate [12], and a slow component of GAr scintillation light. The Gaussian arises instead from the fact that the muon track light is not a point source and, as such, the photons arrive at different timings to the PMT. From simulations this spread in time is compatible with the 10 ns (σ in the plot) obtained from the fit. Since the sampling time of the digitiser is 4 ns, we are not sensitive to the fast component (6 ns). Hereby, τ_1 is not a free parameter of the fit, and has been fixed to 6 ns. The measured value of the slow component is consistent with litterature and supports the evidence of a very clean gas argon inside the cryostat.

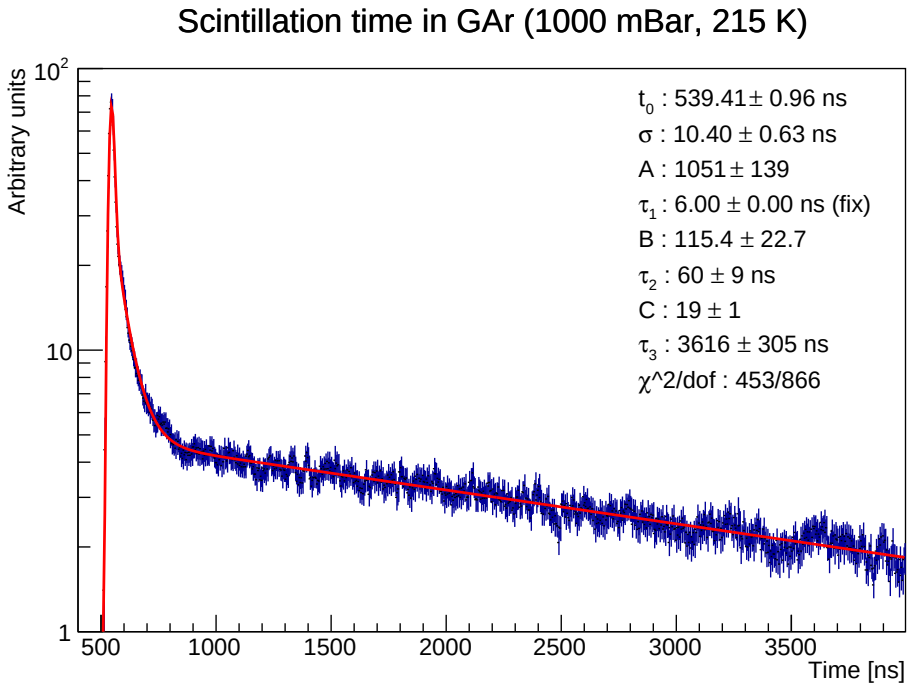

FIG. 18: Averaged waveform from cosmic muons from one PMT, fit with a function (red line) that is the sum of a Gaussian, parametrised by t_0 and σ, and three exponential functions, with decay time constants τ_1, τ_2 and τ_3, and normalisation factors A, B and C.

3.4 Summary of infrastructure scheduling and commissioning

The entire detector was assembled and lifted into the cryostat at the beginning of July 2016, according to the initial schedule. The installation of the cryogenic system by the CERN Neutrino Platform and its commissioning phase however took significantly longer than initially anticipated. The selected cryogenic company, Demaco, had internal delays in production and as a consequence the installation of the cold piping[7] started mid-September instead of July as initially planned. The on-site installation by Demaco was performed according to schedule but a subsequent one month setback in the installation of the warm piping meant that the piston purge and filling of the cryostat could not be started before the annual CERN closure. After an initial pressurisation of the tank, a few leaks were found near the pump tower unit. Once those leaks were repaired the piston purge was performed smoothly over a one month period as reported in Section 3.3.2. After a first cooling down trial it was noticed that the flow of liquid nitrogen inside the condenser could not be precisely regulated due to the formation and accumulation of gas pockets inside the piping. The issue was solved by adding a purge valve on the liquid nitrogen line near the entrance of the condenser. A second cool down phase stared

[7] see Section 3.2.4 for definition of cold and warm piping.

Activity	**start date**	**end date**	**observations**
cold piping installation	Sept 19th	Oct 13th	duration of on-site installation according to schedule. 1.5 month delay on start date.
warm piping installation	Oct 13th	Nov 25th	one month longer than foreseen due to late arrival of some material. As a consequence it was not possible to fill before CERN annual closure
cryogenic functional tests	Nov 25th	Dec 9th	testing of remote valve operations, verification of P&ID, pressure test of piping
closing of manhole and first pressurisation of the tank	Dec 19th	Dec 21st	leaks identified at the pump tower
repairing pump tower leaks	Jan 5th	Jan 24th	leaks on the pump tower flanges + internal leak inside the tower due to a broken bellow. 3 weeks delay introduced.
piston purge in open loop	Jan 24th	Feb 7th	stable at about 2 liters per second, roughly 80 volume changes
gas argon closed loop recirculation	Feb 8th	Feb 15th	stable at ~4 liters per second corresponding to ~80 volume changes
safety clearance for liquid filling	Feb 3rd	Feb 3rd	
first cool down trial	Feb 15th	Feb 16th	
fixing LN2 piping	Feb 16th	Feb 26th	formation of gas pockets preventing stable liquid nitrogen flow inside the condenser. This would have a direct consequence on the stability of the gas argon pressure inside during operation. Fixed by adding a purging valve at the entrance of the condenser. Introduced about 1.5 weeks of delay.
cooling down	Feb 27th	March 3rd	cooling down with spraying nozzles mixture of GAr at 500 l/min and LAr 21.2 l/h. Cooling down interrupted due to presence of ice on the south east corner of the cryostat outer structure.
warming up + dry air flushing	Marchrd	March 12th	in view of a visual inspection inside the tank
visits inside tank by GTT + and membrane inspection	March 13th	ongoing	visual inspections followed by sniffer tests performed by injecting Helium inside the insulation space and sniffing on the south side of the membrane surface and the bottom corners. Where accessible the sniffing was also performed with specifically designed vacuum plug enhancing the sensitivity of the leak check from 1e-5 mbar.l/s to 1e-8 mbar.l/s. No evidence of leak found so far. Discussion on next steps ongoing.

TABLE III: Main dates of the cryogenic system installation and commissioning during 2016-2017.

on February 27^{th}. The temperature was going down steadily until the formation of ice was noticed as reported in the introduction of Section 3. A summary of the main steps related to the cryogenics installation and commissioning phase are summarised in Table III. When applicable, the problems encountered along with the quantification of the introduced delays are also summarised.

4 Progress with DLAr

During 2016 there was a steady and remarkable progress on the design and construction of the DLAr ($6 \times 6 \times 6\ m^3$) detector in the North Area.

The civil engineering works for the extension of the EHN1 hall were completed by September 2016. The impressive construction of the external steel structure of the dual-phase cryostat has been completed as well. The installation of the insulation panels and the corrugated membrane started on March 13th 2017, with the goal of having the cryostat available for the detector installation since the beginning of June 2017.

In parallel the activities related to the detector infrastructure (EHN1 equipments and services, H2 and H4 beam-lines, cryostat and cryogenic equipments) are in an advanced implementation or preparation state. The H2 beam-line design and the design of the beam instrumentation have been completed and their construction phase started. The counting and computing rooms have been built and their related infrastructure equipments (cable-trays, racks, cooling system, electricity, network) are in advanced state of implementation. The cryogenic system contracts have been as well awarded and the final design of the cryogenic installation layout produced.

The WA105 dual-phase DLAr prototyping effort was fully integrated in DUNE since January 2016 as ProtoDUNE dual-phase (ProtoDUNE-DP) in view of developing and testing the design to be deployed in DUNE $10kton$ dual-phase modules. The $6 \times 6 \times 6\ m^3$ detector was optimized in order to take into account the design aspects of the DUNE Far Detector [1] and space limitation at SURF. These optimization aspects have represented a further evolution with respect to the detector design already presented in the WA105 TDR. The DLAr and the dual-phase $10kton$ detector are expected to share the same detector elements, in particular the $3 \times 3\ m^2$ Charge Readout Plane modules. This process of integration in DUNE impacted as well the assembly procedure of DLAr adopting a construction procedure and a definition of the basic detector elements to be prefabricated and transported to the final assembly as close as possible to the one which will be used for the underground construction of the $10kton$ detector at SURF. This will allow performing a full assessment of the final DUNE $10kton$ detector construction chains and of the related QA/QC procedures.

The pre-assembled $6 \times 6 \times 6\ m^3$ detector elements will be transported to the EHN1 hall with similar boxes as the ones foreseen for the underground installation and the installation procedure will as well

mimic the one expected at SURF. An EOI call was organized at the beginning of 2016 in order to integrate new groups willing to join the ProtoDUNE-DP activities. This processed converged by June 2016. Several synergies, as mentioned already in the 2016 yearly SPSC report, were identified and carried on with the single-phase effort within this new environment (beam plug, beam-line instrumentation, high voltage, field cage, slow-control and online processing) and brought to the definition of a common working environment. A notable example of impact of these synergies on the final design of ProtoDUNE-DP has been the field cage design which, although having a different geometry and requirements is based on the same basic structural elements as the single-phase field cage design.

In parallel, the detector construction activities benefited of the experience acquired with the LAr-Proto detector in building 182 during 2016 and the related QA/QC test chain. The LAr-Proto detector allowed for the implementation of a subset of the full FE electronics, DAQ and online processing chains and for a full prototyping of: the slow control system, CRP motorization, signal chimneys, HV system and HV feedthrough and of the other feedthroughs. A detailed description of the experience acquired with the LAr-Proto detector is provided in this report.

Synergies and sharing of basic detector elements among the DLAr with the LAr-Proto detectors were as well already described in details in the 2015 and 2016 yearly reports to the SPSC. An important milestone in 2016 was the achievement of $300kV$, the nominal working voltage for the $6 \times 6 \times 6$ m^3 detector, in a dedicated test setup including the final HV power supply and HV feedthrough. This feedthrough has been then deployed on the LAr-Proto detector. A main goal in 2016 was the finalization of the executive design for the production of three main detector elements such as the Charge Readout Planes (CRP), the field cage and the cathode which was achieved by the end of November 2016. Construction and procurement activities already started for the HV system, FE electronics, DAQ, Online processing and photomultipliers.

4.1 EHN1 hall infrastructure, cryostat and beam-line

The civil engineering works for the EHN1 hall extension were completed in September 2016. Figure 19 shows a picture of the EHN1 hall extension taken just after the completion of the works. from the picture one can appreciate the dimensions of the pit designed to host the two ProtoDUNE detectors. The construction of the steel exoskeleton of the ProtoDUNE dual-phase cryostat was completed during the week of March 6th 2017, in order to follow immediately after with the installation of the insulation panels and the GTT membrane by GABADI on March 13th. Figure 20 shows recent pictures of the $6 \times 6 \times 6$ m^3 detector steel structure of the cryostat. The cryostat, together with the Clean Room Buffer (CRB), which will allow for the insertion of the detector elements during installation, should

become available to the collaboration at the beginning of June 2017, in order to start the detector installation setting-up. Other parts of the infrastructure such as the barracks for the counting room and DAQ and online processing have been already completed as well.

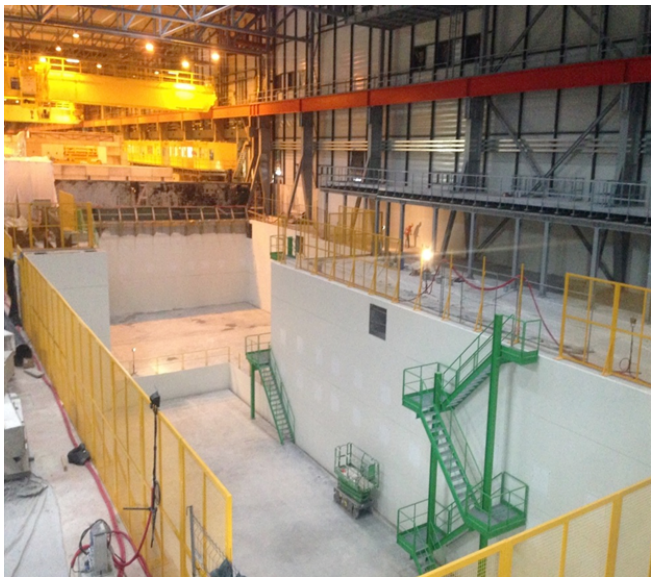

FIG. 19: The pit designed to host the two ProtoDUNE detectors after the completion of the EHN1 hall extension works in September 2016

The H2-VLE tertiary beam-line design has been completed including all the beam-line instrumentation and its construction activities have started. The tertiary beam-line (Figure 21) includes 3 collection quadrupoles, located after the T22 secondary target, followed by: a pair of bending magnets, a two jaws collimator, a quadrupole, a second pair of bending magnets and two final focusing quadrupoles. These two last quadrupoles are installed on a straight section of about 11 m which leads to the beam window of ProtoDUNE-DP.

A 3D model of the layout is presented on Figure 22. The dipoles are represented in red while the quadrupoles in blue. The dipoles are mounted on supports tilted by 33.5 degrees in order to ensure a simultaneous bending on the vertical and horizontal planes. The beam is then shifted on the horizontal plane, from the Jura side edge of EHN1 to the Saleve side, in order to meet the entrance window of WA105 and to have at that point a direction parallel to the diagonal of the field cage. On the horizontal plane, since WA105 is hosted in a pit, the beam goes down from the level of the H2 line to the WA105 beam window with a slope of 7.735 degrees. The secondary target and the first quadrupole are installed in a shielding tunnel made of concrete blocks.

A typical tertiary rate of 100-200 Hz is achieved on the H2-VLE beam-line with a H2 secondary beam intensity of 1×10^6 particles per spill impinging on the T22 target. This low intensity is far from the maximal intensity allowed by radioprotection rules for H2 which corresponds to a few 10^7

FIG. 20: Recent pictures of the ProtoDUNE-DP cryostat exoskeleton: global view from the bottom of the pit (left), top view of the cryostat with the Temporary Construction Opening (right)

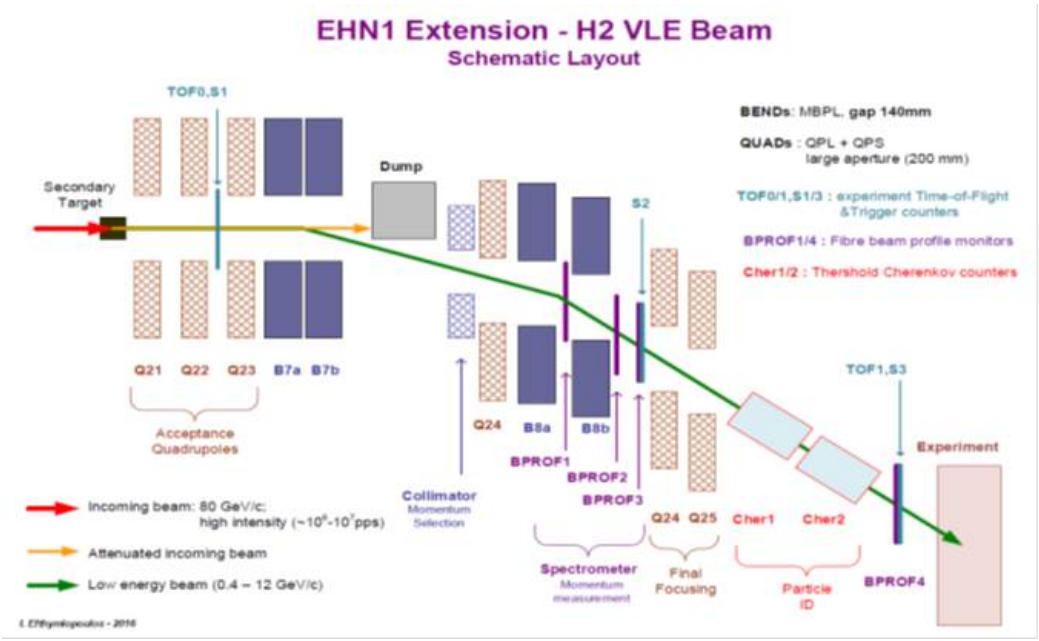

FIG. 21: H2-VLE beam-line design

FIG. 22: 3D CAD view of the H2-VLE beam-line

particles per spill. The beam momentum can be selected by changing the currents in the magnets from about 1 GeV/c to 12 GeV/c. The momentum bite corresponds to 5%. It can be reduced to 1% by exploiting the measurements from the spectrometer integrated in the beam-line. The production and transport of particles corresponding to the beam-line final configuration has been completely simulated. The tertiary beam simulated composition, corresponding to a secondary beam of positive particles at $80 GeV/c$ impinging on T22, is shown as example in Figure 23. The final beam fluxes are compatible with and validate those already used to formulate the beam requests for 2018 in the 2016 SPSC yearly report. Hence, we reiterate our beam exposure request.

Momentum [GeV/c]	anti-p	e-	e+	K-	K+	mu-	mu+	p	pi-	pi+
0.4	0.00%	0.00%	97.61%	0.00%	0.00%	0.00%	0.00%	0.48%	0.00%	1.91%
1	0.00%	0.00%	74.20%	0.00%	0.00%	0.00%	0.00%	14.94%	0.00%	10.86%
2	0.00%	0.00%	45.83%	0.00%	0.67%	0.00%	0.96%	20.04%	0.00%	32.50%
3	0.00%	0.00%	68.29%	0.00%	0.64%	0.00%	0.42%	7.72%	0.00%	22.94%
4	0.00%	0.00%	53.72%	0.00%	1.46%	0.00%	0.65%	7.56%	0.00%	36.61%
5	0.00%	0.00%	42.38%	0.00%	2.47%	0.00%	0.83%	9.18%	0.00%	45.14%
6	0.00%	0.00%	31.42%	0.00%	3.83%	0.00%	0.73%	10.10%	0.00%	53.92%
7	0.00%	0.00%	24.70%	0.00%	4.08%	0.00%	0.85%	9.92%	0.00%	60.46%
8	0.00%	0.00%	19.36%	0.00%	5.11%	0.00%	0.97%	11.33%	0.00%	63.24%
9	0.00%	0.00%	15.12%	0.00%	5.67%	0.00%	0.82%	11.10%	0.00%	67.29%
10	0.00%	0.00%	12.36%	0.00%	6.02%	0.00%	0.71%	12.25%	0.00%	68.66%
11	0.00%	0.00%	10.46%	0.00%	6.95%	0.00%	0.82%	13.57%	0.00%	68.20%
12	0.00%	0.00%	8.90%	0.00%	6.89%	0.00%	0.66%	14.26%	0.00%	69.30%

FIG. 23: Tertiary beam composition for a secondary positive beam at $+80 GeV/c$ impinging on the T22 target

The beam instrumentation includes 4 beam profile monitors (BPROF) acting also as trigger counters, they are based on fibers hodoscopes with $1mm$ pitch coupled to $2mm$ thick scintillator tiles and two Cerenkov threshold detectors C1 and C2, filled with CO_2 and operating respectively at low

($\leq 3bar$) and high pressure ($\leq 15bar$). The BPROF can act as a Time Of Flight system (TOF) with $32m$ lever arm and $1ns$ resolution as well as an integrated spectrometer by exploiting the scintillating fibers hodoscopes.

The line will operate as a mixed hadrons beam or as a pure electrons beam. When operating as mixed hadrons beam, particles identification is provided by combining the measurements of the TOF with the two Cerenkov counters C1 and C2 as shown in Table IV. The baseline identification assumes no K/p separation in between $3.0-5.0GeV/c$ and no electron tagging in the high energy range ($5.0-12.0GeV/c$). Residual contamination of electrons and muons in the hadron beam can be identified in the liquid argon itself. In the electron operation mode, which can be selected by changing the T22 target, H2-VLE will provide a high purity electron beam. Its energy spectrum will be characterized with a lead glass calorimeter, as mentioned in more details later, which will allow measuring the beam energy spectrum and the fraction of electrons showering in the materials along the beam-line.

Momentum GeV/c	e	π	K	p
0.4-3.0	C1 (CO_2 $1bar$)	TOF	absent	TOF
3.0-5.0	C1 (CO_2 $1bar$)	C1 (CO_2 $3.5bar$)	No C2	No C2
5.0-12.0		C1 (CO_2 $1bar$)	C2 ($CO_2 \leq 14bar$)	No C1, No C2

TABLE IV: Particle identification criteria as a function of the momentum range by combining the information from the TOF system and the two Cerenkov threshold counters (C1 and C2)

The data acquisition of the beam-line instrumentation has been integrated with the ProtoDUNE-DP DAQ by using the White-Rabbit timing distribution system which will allow the two DAQ systems to time-stamp triggers on a common time basis and merge the information offline by performing queries to the beam instrumentation database.

In ProtoDUNE-DP the beam is entering from the corner of the detector, which is a structurally weak region. GTT recommended not to alter the integrity of the $2mm$ stainless steel membrane with a beam pipe penetration. Given this constraint from GTT and given the fact that most of the passive material crossed by the beam particles would be represented by the LAr itself present in between the membrane and the field cage, it was decided to simplify the beam window/ beam pipe design. The beam window design is then focusing on the major contributions in terms of passive materials while leaving the stainless steel membrane and the foam of the insulation panels untouched. The beam penetration is therefore mostly affecting the exoskeleton. The exoskeleton is modified by drilling a hole in the 10 mm external stainless steel plate and by installing on that penetration a gate valve and a thin beam window connected to the beam pipe. These modifications to the cryostat structure are hence

minimal. The beam should point to the 3D center of the drift volume with a slope of about 7 degrees, given by the constraints from the beam-line layout. Once gone through the beam window, the beam will then cross the insulation foam and the 2 mm stainless steel membrane reaching, immediately after the membrane, a beam plug which is going all across the dead LAr volume and through the field cage rings. The design of the beam-plug is in common with the single-phase ProtoDUNE. The design for the dual-phase protoDUNE is based on an adaptation of the one developed for the single-phase cryostat which takes into account the longer length of the beam plug and the installation in the detector corner. The voltage present on the field cage in correspondence to the beam plug penetration height is slightly lower than in the case of the single-phase set-up.

The beam plug will be made in insulator materials in order to avoid interferences with the high voltage present on the field cage on which the beam plug is integrated and supported. A voltage degrader is present in order to go from the ground potential to the one of the field cage. The beam plug will also be supported with insulating arms connected to the cryostat membrane, similarly as the cryogenic piping supports, and it is not mechanically supported by the field cage itself (see Figure 24).

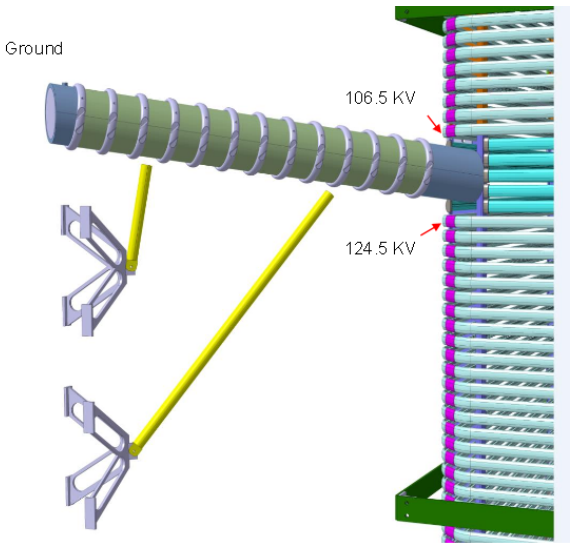

FIG. 24: Beam plug design adapted from the single-phase design

The beam plug will minimize the amount of LAr crossed after the $2mm$ stainless steel membrane from more than $1.5m$ to about a couple of mm. The effect of passive materials before reaching the LAr active volume is particularly relevant for electrons.

It is foreseen to characterize the effect of passive materials along the beam-line down to the cryostat by performing, during the period foreseen in the general EHN1 schedule for beam commissioning, some exposures with a portable lead glass calorimeter to be put just upstream the beam window. The tails of the electron spectrum in the energy spectrum measured by the lead glass will allow calibrating

precisely the effects of dead materials along the beam-line for various momenta. This device has been already employed to characterize other beam lines at CERN and at DESY and it is completely linear with a well understood response.

The same kind of exposure can be repeated during the beam commissioning period also inside the cryostat,during detector installation. The H2 beam commissioning window corresponds to the middle of the detector WA105 construction period. This additional measurement would allow calibrating the energy losses in the insulation materials and in the beam plug, which could be temporarily installed inside the cryostat explicitly for this measurement. The timescale for this measurement depends on the precise interplay between beam instrumentation commissioning and detector installation schedule. This is not precisely defined at the moment

4.2 TPC instrumentation and electronics

The activities on $6 \times 6 \times 6\ m^3$ detector were focusing since April 2016 on the completion of the executive mechanical design of some remaining aspects of the detector, such as: the mechanical frames of the Charge Readout Planes integrating the LEM detectors, the field cage, which shares common structural elements with the single-phase ProtoDUNE and the cathode.

The executive design finalization was accomplished by the end November 2016. Figure 25 shows a general 3D view of the detector including all the detector elements corresponding to the final design. A cut view drawing is presented in Figure 26 reporting integration details such as the gas space above the anode level and the insulation space below the cathode which will host also the photomultipliers and their supports.

4.2.1 Photomultiplier design

The 36 cryogenic photomultipliers (PMTs) are fixed on the membrane floor in the areas within the membrane corrugations. The PMTs mechanical supports do not affect the membrane integrity but are using as basis stainless steel plates of about the same size of the membrane corrugations pitch. These supports can be then hosted in the flat regions of the membrane floor of the cryostat in between the corrugation pattern.

The arrangement of the photomultipliers has been optimized in order to be compatible with the presence of the cryogenic piping on the membrane floor. The weight of the support overwhelms the photomultiplier buoyancy. Given the large standing surface of the stainless steel plate support basis, these supports will ensure as well stability against lateral forces possibly acting on the photomultipliers due to the liquid flow (see Figure 27). Fourty photomultipliers were procured in December 2016. The

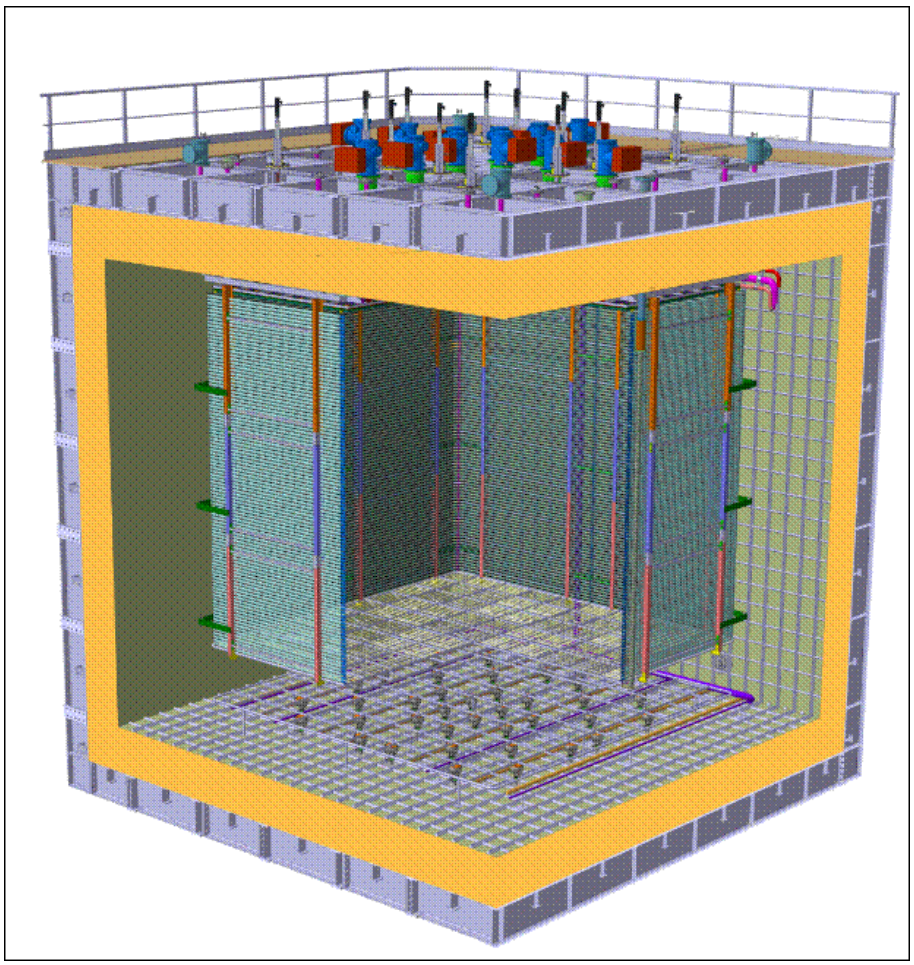

FIG. 25: 3D cut view of the ProtoDUNE-DP detector including the detector elements corresponding to the executive design.

TPB coating of the photomultipliers has been agreed by using the ICARUS facility at CERN. A light calibration system integrated in DLAr has been designed as well in order to monitor the calibration of the PMTs installed inside the detector. An optical fiber will be installed at each PMT in order to provide a homogeneous and configurable amount of light. Tests to check that the fibers stay in place at cryogenic temperature have been performed with satisfactory results. Several tests to study if there is any light loss due to adding a connector on the fiber or mechanical stress are on-going.

A design validation test setup with a laser and an optical fibers light distribution system was built in order characterize the response at room temperature and at the temperature of liquid nitrogen (see Figure 28). This setup allowed performing extensive tests and measurements such as: gain dependence on the high voltage, linearity, dark current rate and memory effects on response to two light pulses which are close in time. Two different HV divider base designs were tested. The positive base (PB) design which uses positive HV and only one cable was chosen over the negative base (NB) using negative HV and two cables (one for the signal and one for the HV) based on the following results: the light

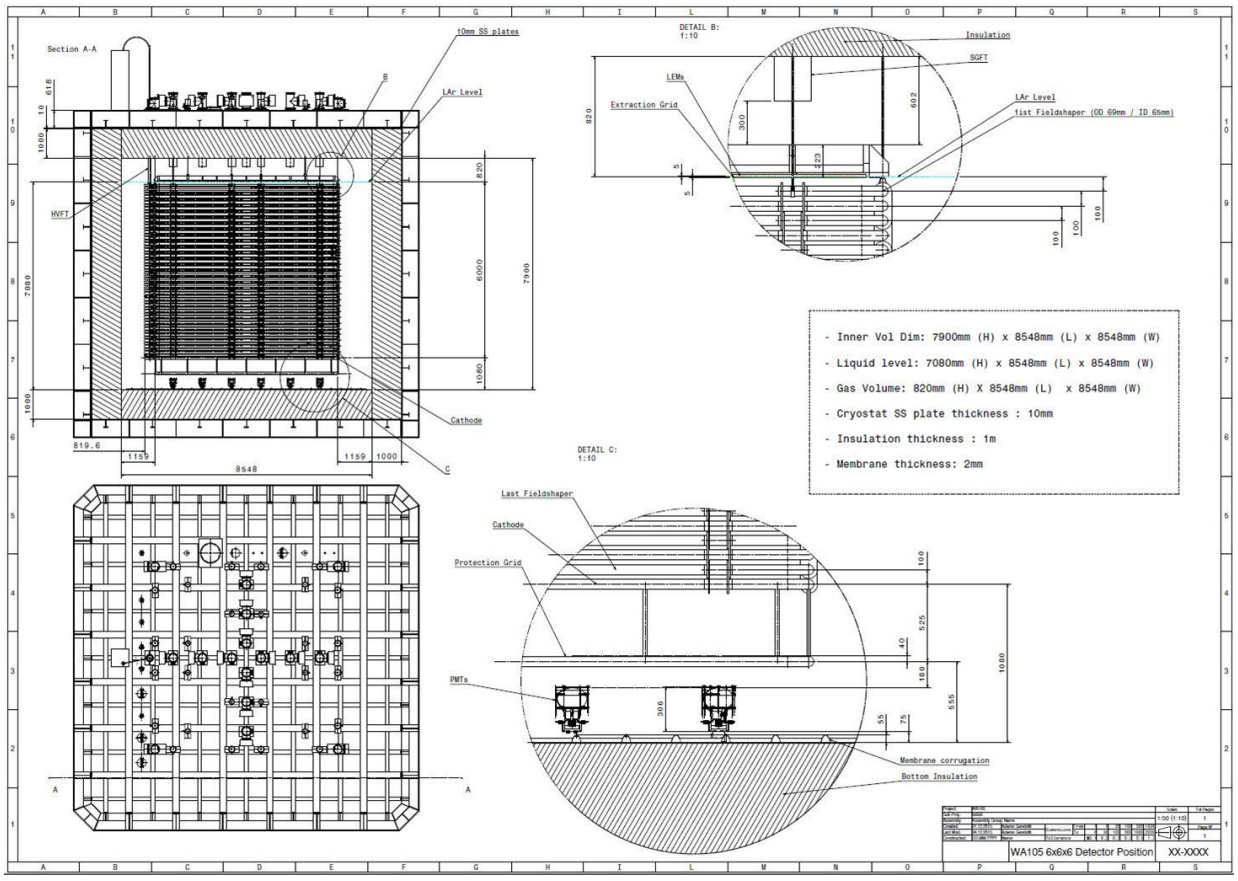

FIG. 26: ProtoDUNE-DP TPC integration within the cryostat.

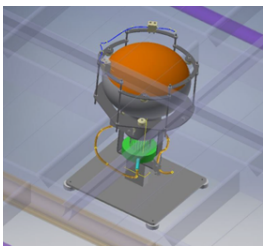

FIG. 27: Hamamatsu R5912mod02 photomultiplier with its mechanical support for the installation on the cryostat membrane floor.

linearity is independent from the base used; the dark current rate is smaller in the PB than in the NB, the PB saturates at higher frequencies than the NB, and less cables are required in the installation for the PB. The performance at cryogenic temperature of the PMT has been measured as expected: dark current is higher, gain is lower than at room temperature; and linearity and saturation with frequency present the same behaviour. In addition, a decrease in the PMT gain after applying 1900V to the PMT or high frequency light has been observed at cryogenic temperature.

A systematic QC procedure for the photomultipliers procurement is being set up with a cryogenic vessel for tests in batches of 10 PMTs (see Figure 29).

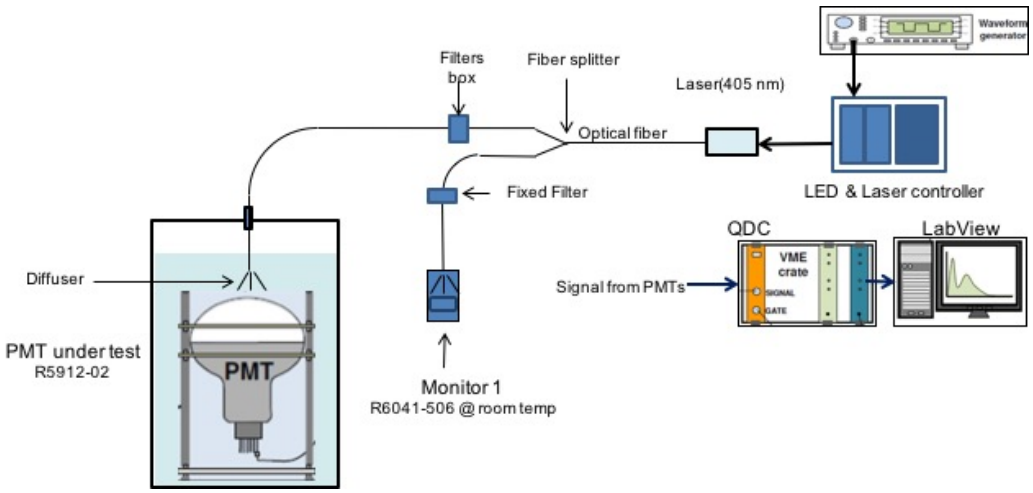

FIG. 28: Light distribution system for the photomultipliers characterization tests.

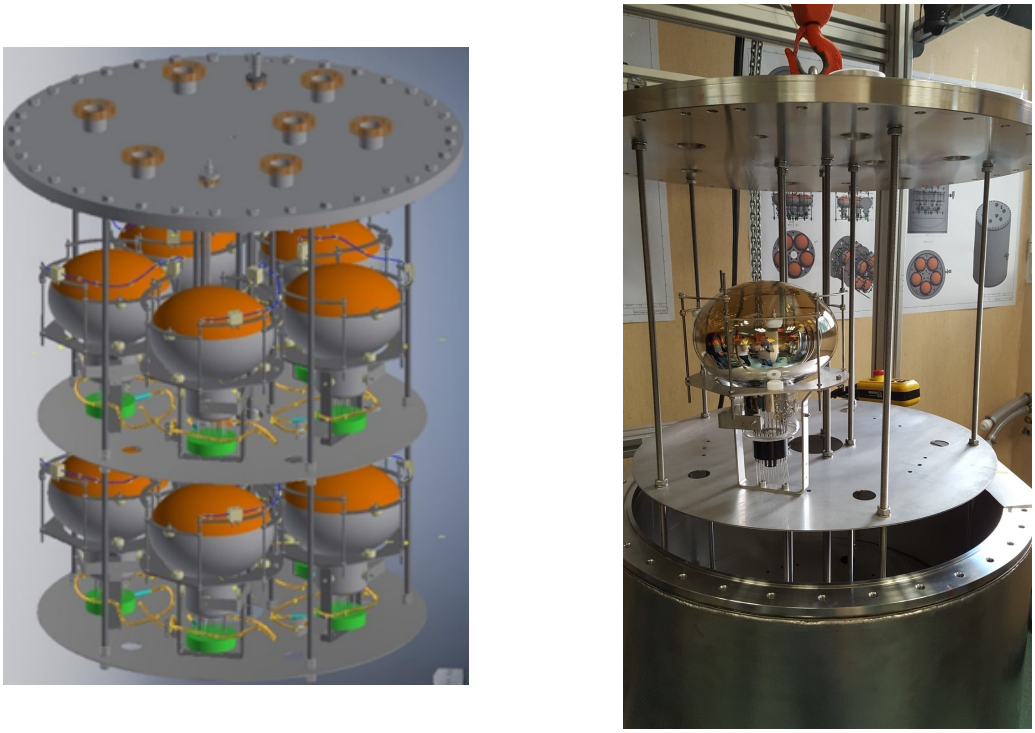

FIG. 29: Cryogenic setup for PMTs QC tests for batches of 10 photomultipliers.

4.2.2 The CRP design

The Charge Readout Planes (CRP) are the basic readout components of the future 10 kton dual-phase detector modules as well as of the DLAr. This common design is based on CRP modules of 3×3 m^2 suspended from 3 points in order to be accurately aligned with respect to the LAr surface. The CRP includes a submersed extraction grid at $1cm$ from the bottom face of the LEMs. The extraction grid and the LEMs bottom face define the electric field which is exploited in order to extract the electrons from the liquid to the gas phase. The liquid argon level should be across the $1cm$ gap in

between the grid and the LEMs. The suspension system allows adjusting the position of the gap with respect to the liquid level as well as the parallelism of the CRP plane with respect to the liquid surface. Each DUNE Far Detector 10 kton module will include 80 of such units which will be pre-assembled and transported underground in ad-hoc transportation boxes. The DLAr will provide a full scale test of this concept by having its anode plane segmented in 4 of these 3×3 m^2 CRP units. Each CRP integrates 36 LEM-ANODE sandwiches of 50×50 cm^2. Figure 30 shows the integration of these 4 CRP planes in order to cover the $36m^2$ readout surface of DLAr. The installation procedure at EHN1 will be mimicking as much as possible the DUNE underground installation procedure. Also the assembly and QA/QC procedures should as well represent a complete implementation test of the production chain foreseen for DUNE.

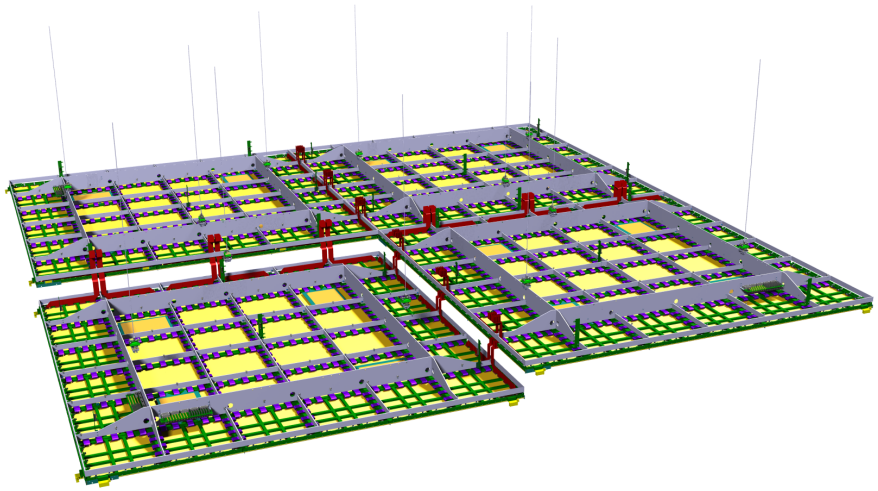

FIG. 30: Four 3×3 m^2 CRP planes covering the $6 \times 6m^2$ readout surface of DLAr.

An important aspect of the CRP design concerns the planarity requirement of $\pm 0.5mm$ over the 3×3 m^2 CRP surface. These planarity requirement must be met even in presence of a potential temperature gradient in the gas phase above the LAr level and of gravity effects on the CRP structure associated to its flexibility and on the way it is suspended. The CRP is subject to thermal contractions when put at cold. Differential contractions effects may occur because the structure includes composites materials and also because of the thermal gradient present in the argon gas, implying a different shrinking at various heights with respect to the liquid argon level. These differential effects may induce deformations and non-planarity conditions.

The design of the CRP satisfies the planarity requirements mentioned above by exploiting a main structure built in Invar which then supports a G10 frame integrating the LEM-anode sandwiches. The G10 structure has a thermal expansion behavior very similar to the one of the LEM/anode sandwiches Figure 31.

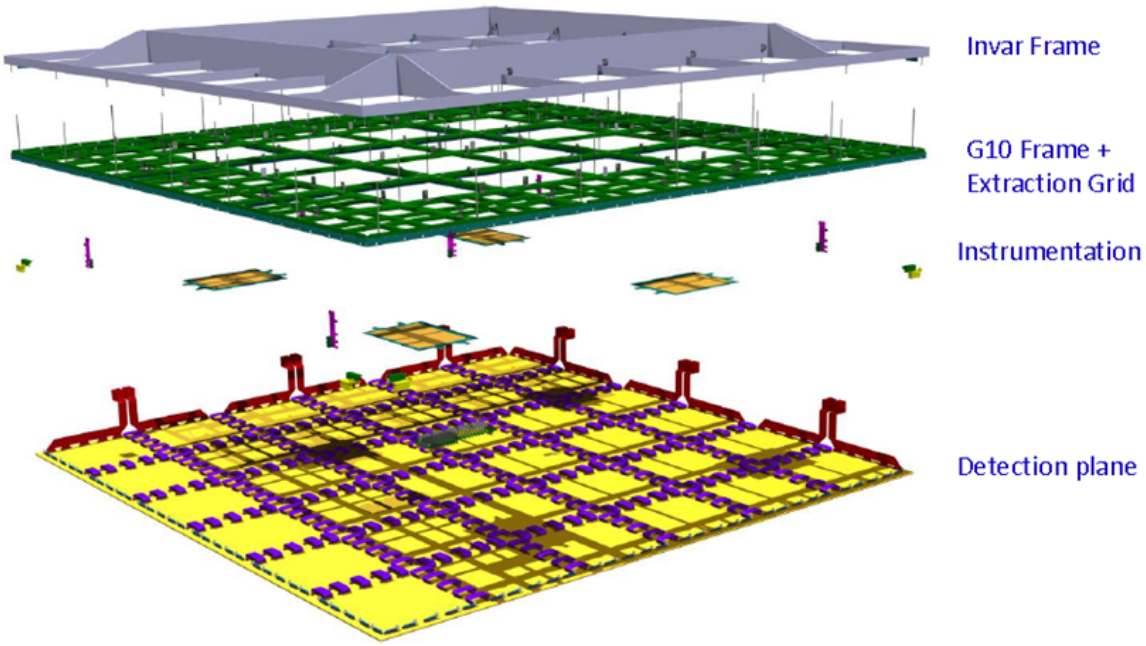

FIG. 31: Exploded view of a CRP plane structure.

The Invar frame has little sensitivity to differential shrinkage effects related to the thermal gradient in the gas. The connection among the Invar and G10 frames integrates sliding decoupling mechanisms (Figure 32) in the fixation points. The decoupling mechanisms ensure the mechanical support from the Invar structure and a fixed vertical positioning of the two structures, while allowing for horizontal movements of the G10 frame related to the differential in thermal shrinkage. The G10 frames supports as well the submersed extraction grid.

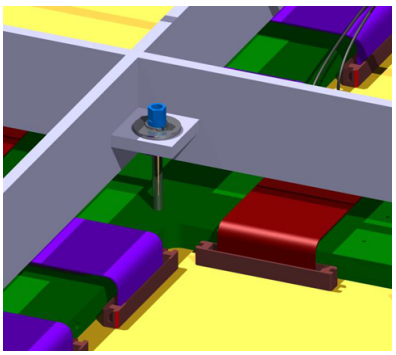

FIG. 32: Decoupling mechanism for linking the CRP G10 frame (green) to the Invar main frame (gray). This mechanical support defines the vertical separation and link among the two frames but it is free to move horizontally in order to allow for the different thermal shrinkage.

The CRP structure executive design has been thoroughly optimized by taking into account simulation results and a campaign of dedicated cold bath tests (see Figure 33, Figure 34). Open cold bath tests in liquid nitrogen accompanied by digital photogrammetry measurements and a full slow control

instrumentation (temperature probes, strain gauges) have been systematically performed. They allow directly studying the CRP structure of the LAr-Proto and the behavior of the structural elements to be employed in order to build the DLAr CRP structure in order to assess differential effects in thermal contraction and to test the design of the decoupling mechanism.

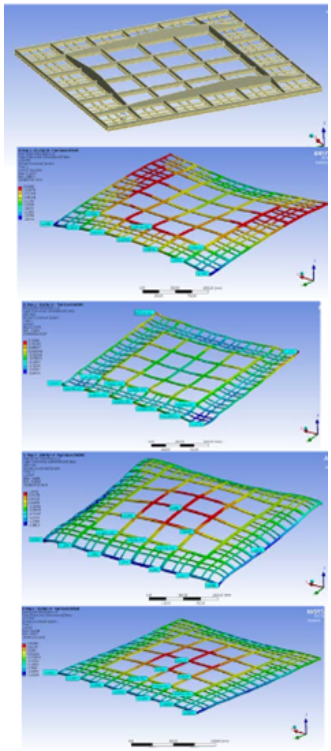

FIG. 33: Simulations of the CRP non-planarity deformations related to thermal and gravity effects.

FIG. 34: Cold bath test of CRP structures with and without decoupling mechanisms. In absence of decoupling the different thermal contraction coefficients of the two materials in the sandwich generates non planarity effects.

The executive design for the integration of the grid of submerged extraction wires in the CRP G10 frame was as well finalized while minimizing the dead space in between CRPs put side by side. The wires of the extraction grid are supported from vertical printed circuit boards attached to the G10 frame. The dead space in between the active areas of different CRP modules is limited below $1cm$ (see Figure 35). Several solutions for the wires supports with vertical printed circuit boards and wires brazing were tested in order to optimize the final design.

The feedtrhoughs for the CRP suspension include the support for the motorization and allow for an horizontal adjustment of the hanging point in order to compensate for the thermal shrinkage of the G10 frames and ensure a minimal dead space in between CRP modules (see Figure 36) by getting them closer. The design of the CRP assembly chain and of the related tooling was as well part of the CRP executive design finalization.

The LEM and anode printed circuit boards are integrated in the CRP support structure and are

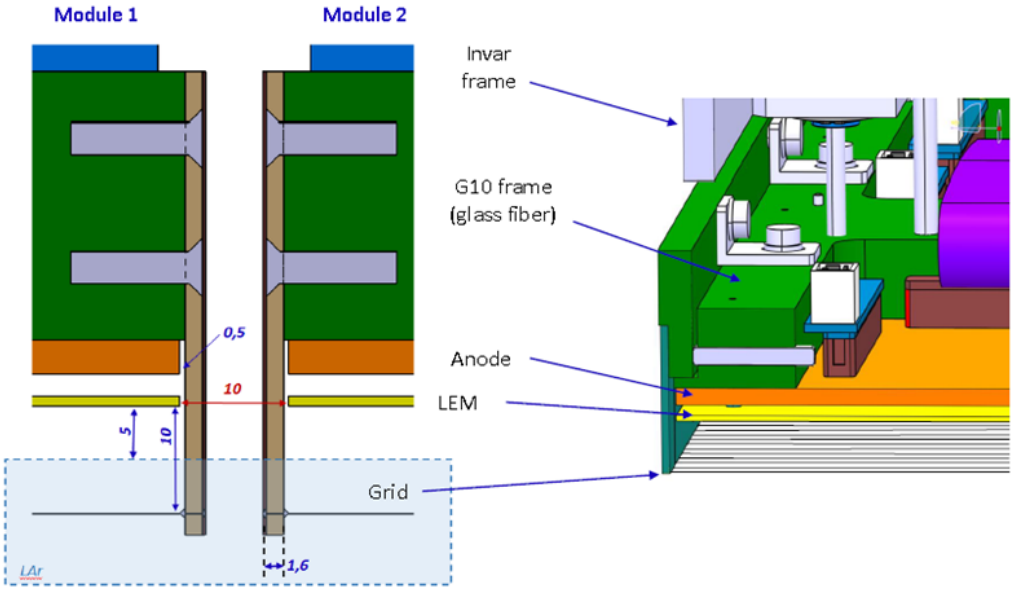

FIG. 35: Integration of the extraction wires grid in the CRP frame design.

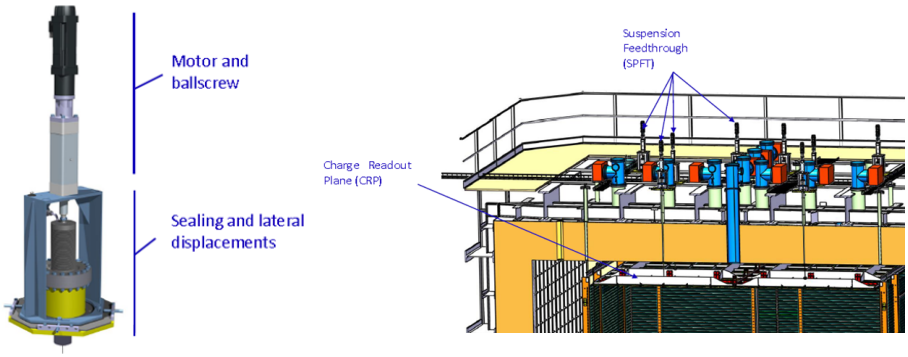

FIG. 36: Design of the CRP suspension feedthrough and 3D view of the CRP suspension feedthroughs on the cryostat roof.

other basic detector elements for which large production and systematic QA/QC procedures have been organized. The cleaning and commissioning procedures and the definition of the tooling for the LEMs tests have been benefiting of the continuous experience accumulated during the last year with the LAr-Proto. These studies allowed to finalize these QA/QC procedures for the LEM and anodes procurements in view of the DLAr instrumentation as well as the production and procurement plans. The production of the LEM has been organized by taking into account two printed circuit board production companies which already produced batches satisfying the requirements which are described in a detailed specifications document used for tendering.

4.2.3 The cathode design

The R&D activity on the transparent/resistive cathode made of an array of PMMA plates with a conductive coating made of Indium Tin Oxyde (ITO) and conceptual design for PMMA plates integration in cathode structure were completed in 2016. PMMA plates have ITO coating on both sides and can incorporate on the upper side a TPB wavelength shifter layer deposited by evaporation. This setup can then provide the shifting of the UV $128nm$ scintillation light to visible $420nm$ light and the transparent transmission of this latter light to the photomultipliers located at the bottom of the tank below the cathode. In this case it is not anymore necessary to have a TPB coating at the level of the photomultipliers, as foreseen in the baseline design. Uncoated photomultipliers are insensitive to the UV scintillation light produced in the LAr volume below the cathode. This design by construction nicely limits the fiducial volume for the light readout to the one above the cathode surface. PMMA resistive plates can be assembled in segmented large area transparent cathodes which provide as well sparks protection and shielding against bubbles coming from the bottom of the tank.

The R&D work performed in 2016 assessed stable conditions for the ITO coating and for its conductivity at room and cryogenic temperatures. ITO coated PMMA plates produced by the industry with dimensions up to $850 \times 600\ mm^2$ were tested on small prototypes in order to characterize the technology and the stability of the materials (see Figure 37). No mechanical or electrical problems were encountered also in presence of repeated thermal cycles. Tests demonstrated the stability of the ITO coating and of its optical properties and transparency to light as well as the mechanical properties of the plates, in order to optimize their thickness. The final size of the plates to be used for the construction of the cathode was eventually chosen to be $650 \times 650 \times 10\ mm^3$. The support structure to integrate these PMMA plates was designed as well as the system allowing for the electrical contacts of the plates (see Figure 38). The infrastructure for the TPB evaporation coating of the plates was set up.

During the LBNC review of October 2016 some comments were raised on the fact that the PMMA transparent cathode, despite all the successful R&D program and the tests carried on, was introducing some elements of novelty in the $6 \times 6 \times 6\ m^3$ design and possibly also some risks which would not be retired by the $3 \times 1 \times 1\ m^3$ operation, since that detector is using a standard mesh cathode.

Following the recommendations of the LBNC Committee, during the month of November 2016 it was decided not to implement the PMMA transparent cathode in the $6 \times 6 \times 6\ m^3$ but to reactivate the baseline cathode design. The baseline design is based on a pipes mesh, which had been extensively studied in the LAGUNA-LBNO design study and which was present already at the level of the WA105 TDR.

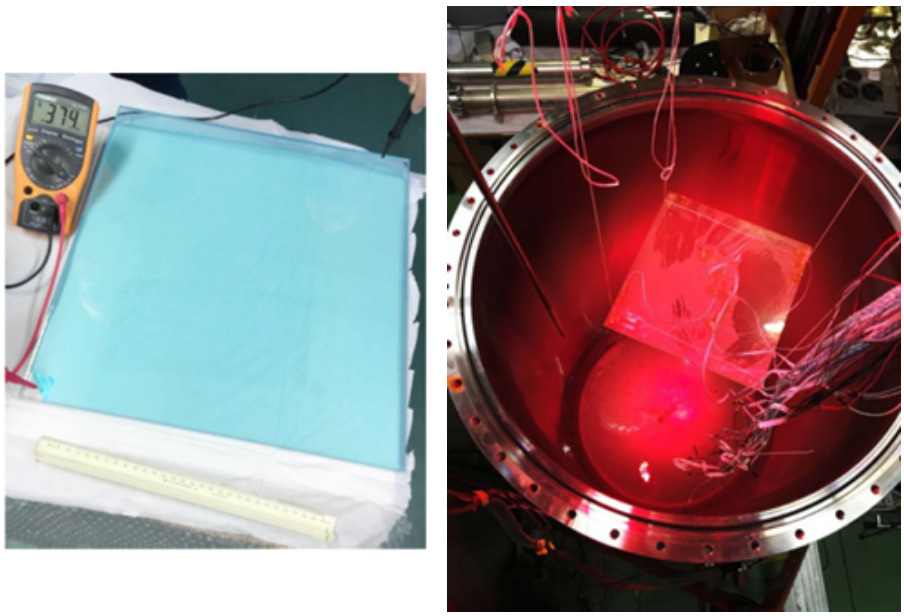

FIG. 37: Industrially produced PMMA transparent resistive plate with ITO coating and their tests at cold

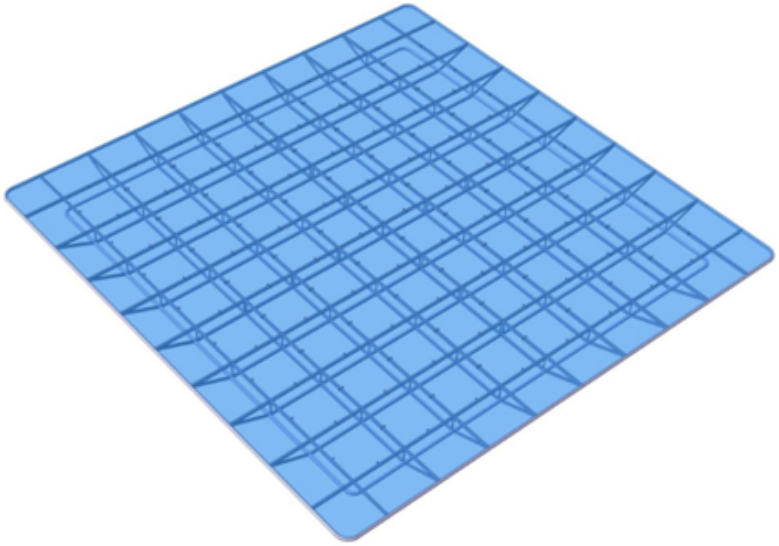

FIG. 38: Integration of the PMMA ITO coated plates in the transparent cathode structure.

In order to complete the executive design on time by the end of November 2016, the PMMA cathode mechanical structure was re-adapted to the pipes mesh design by introducing some minimal changes. The structure was studied for the PMMA plates integration was adapted by inserting at the place of the plates $20mm$ diameter stainless steel pipes with $105cm$ pitch (see Figure 39). Full electrostatic simulations were performed in order to check again that the local electrical field in proximity of the cathode was not exceeding $30kV/cm$ when operating at $600kV$ voltage. The nominal voltage value for ProtoDUNE-DP operation is $300kV$. The goal of $600kV$ corresponds to a possible second operation phase of ProtoDUNE-DP at higher electric field in order to have the same maximum HV foreseen the

$10kton$ DUNE Far Detector.

Also the installation procedure in the cryostat and the PMTs mechanical arrangement on the cryostat floor, which had been already studied for the same mechanical structure hosting the PMMA plates, were kept unchanged. Similarly the design of the protection ground grid in front of the photomultipliers was completed. This one is based on $2mm$ wires embedded in a stainless steel frame made of squared pipes of $40/20mm$ size with beam-line corners, similar as the main pipes used for the cathode structure (see Figure 40). Both the cathode and protection grid design are based on basic elements of $3 \times 3\ m^2$ which are pre-assembled and then transported and mounted inside the cryostat by using transportation boxes similar to the ones for the CRP transportation

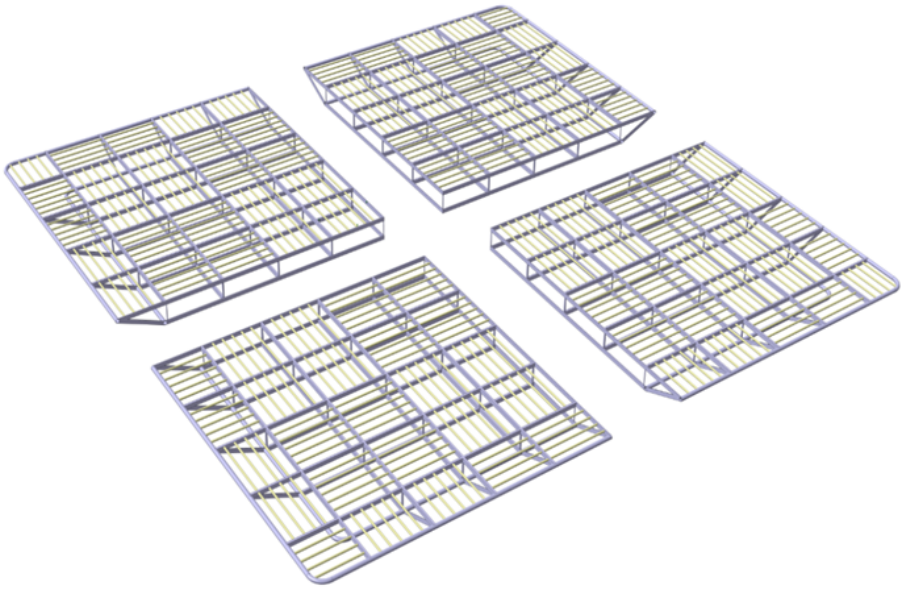

FIG. 39: Exploded view of the final cathode structure, with the baseline design based on the pipes mesh.

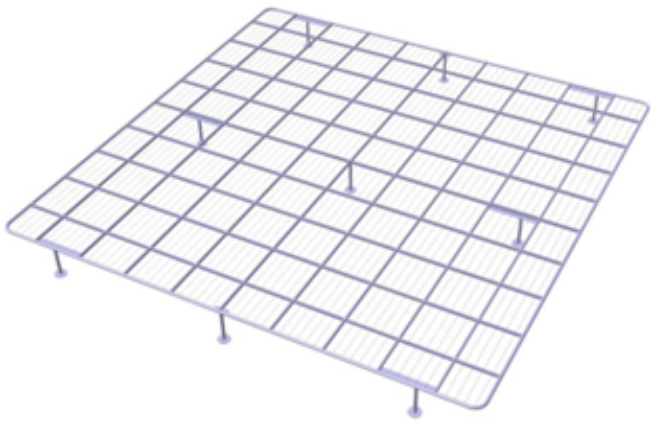

FIG. 40: Design of the ground grid placed below the cathode, in front of the photomultipliers array.

These modifications allowed to complete the cathode executive design by November 2016. The

reactivation of the baseline design of the cathode has been introducing a simplification of the $6 \times 6 \times 6$ m^3 design and it has been retiring some risks, following the LBNC committee comments. The design and electrostatic calculations of the full HV system including the feedthrough, the field cage and the connection to the cathode have been finalized as well.

4.2.4 Field cage design

The executive design of the field cage, based on common structural elements with the single-phase ProtoDUNE field cage was completed as well at the end of November 2016. This solution offers the possibility of building the field cage out of a light structure with profiles which can be customized in order to reduce the intensity of the electric field in their proximity. These profiles are also completely open in order not to trap air inside and to facilitate the evacuation of the impurities during the gas purge phase of the cryostat filling.

The R&D activity conducted in the framework of CERN Neutrino Platform demonstrated the possibility of building the field cage out of extruded aluminum open profiles. A small scale prototype fully demonstrated the validity of this design and of the choice of aluminum as a conductor. Aluminum showed no negative effects related to the surface conditions (see Figure 41) compared to stainless steel. Another dedicated setup operating in the ICARUS $50liters$ cryostat demonstrated the absence of long-term effects (related to possible Malter effect in liquid argon) such as charging-up related to the oxidation of the uncoated aluminum surface. The use of aluminum profiles for the field cage construction was then validated by the DUNE Technical Board for the two ProtoDUNEs, the application of a conductive coating to the extruded profiles can be performed at production with a modest cost increase and it offers an additional safety factor.

FIG. 41: Prototype built at CERN in order to test the field cage design based on the extruded open aluminum profiles

The extruded aluminum profiles are integrated in panels kept together by FRP I-beams. The dimensions of the panels have been optimized to the dual-phase detector geometry. Three sub-modules panels including 33 profiles with $60mm$ pitch are integrated in a vertical module of $6238 \times 3017\ mm^2$ hanging from the roof of the cryostat (see Figure 42). The bottom sub-module, which is supporting the cathode, includes, differently than the other two sub-modules, 32 profiles plus the cathode.

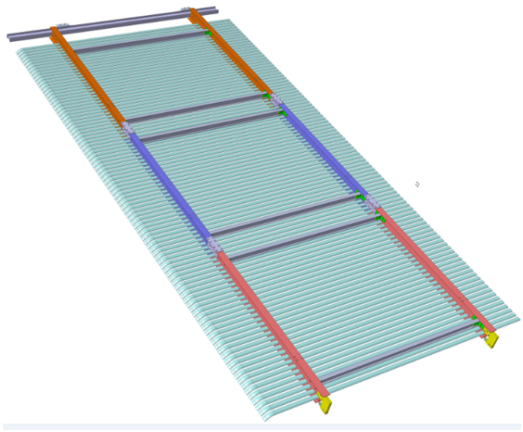

FIG. 42: One of the eight vertical modules composing the field cage. Each vertical module is composed by three sub-modules respectively including 33, 33 and 32 extruded aluminum profiles. The three sub-modules are assembled in vertical modules inside the cryostat

In total there are 98 profiles per vertical module and two vertical modules per detector face. In total 8 vertical modules compose the field cage (see Figure 43). The sub-modules are built in a clean room and then installed inside the cryostat. The field cage construction proceeds by assembling the sub-modules in vertical modules chains which are progressively built and lifted towards the roof of the detector by using ropes suspended from the field cage hanging feedthroughs, one row at the time.

Unlike the single-phase design, the profiles of different sub-modules are not terminated with insulating caps but connected together. The profiles at the same height, belonging to different vertical modules, are electrically connected in order to form equi-potential rings. This connection is performed by using clips which are mounted during the field cage assembly. There are straight connections at the middle of the field cage faces and corner connections as well. The profiles are bent at 45 degrees in order to ensure a smooth connection at 90 degrees in correspondence of the field cage corners (see Figure 44). The bending of the profiles is performed at production, before the assembly of the panels, by using a dedicated tooling which has been tested and proven to produce a smooth bending.

Detailed electrostatic simulations have been performed in order to optimize the shape of the extruded profiles and of the clipping profiles (see Figure 45). A dedicated test setup at CERN allowed to test and optimize the design of the clipping connections and the design of the printed circuit boards with the electrical elements (see Figure 46).

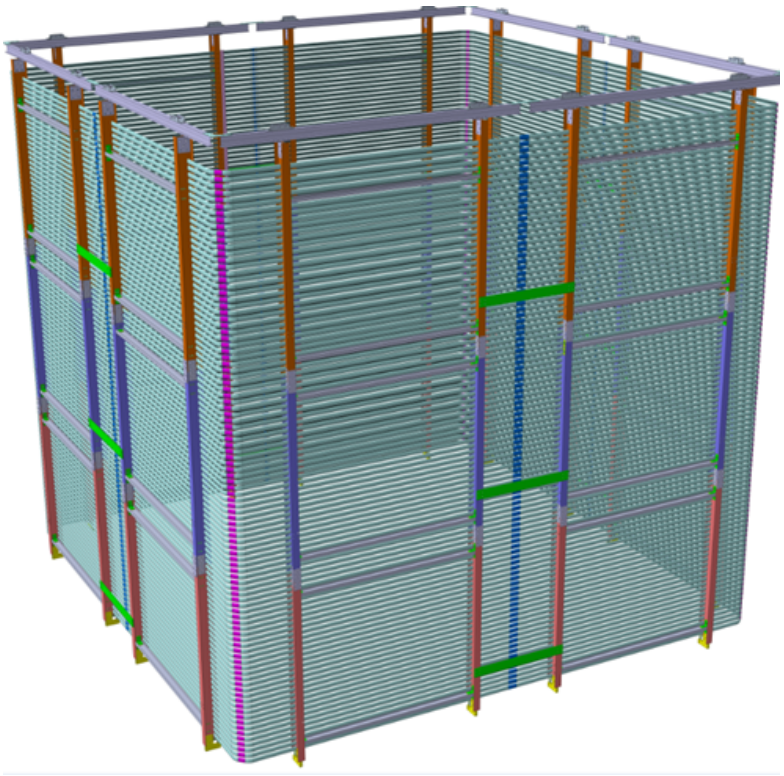

FIG. 43: 3D view of the 8 vertical modules composing the field cage

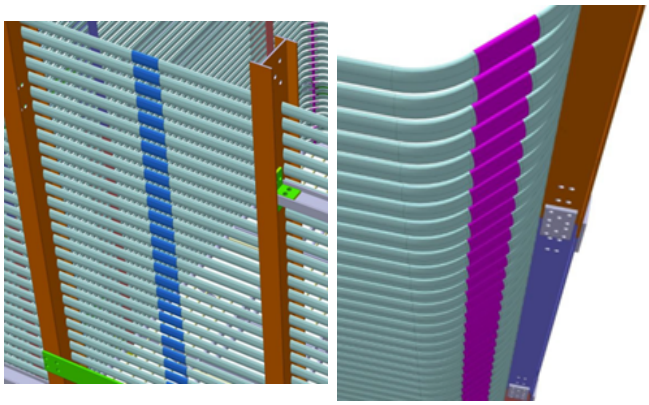

FIG. 44: Details of the clipping profiles used to ensure continuity of the extruded profiles belonging to different vertical modules at the center and in the corners of the field cage.

The HV distribution among the field cage rings is provided by printed circuit boards (see Figure 47) mechanically integrated in the field cage assembly. Each PCB interconnects 11 profiles. The basic circuit, corresponding to a stage in between every pair of profiles, includes a set of two resistors of $2GOhm$ connected in parallel and mounted in parallel with a chain of three varistors (ERZV14D182) which are connected in series . The total resistance of each single stage is $1GOhm$ and the voltage drop corresponds to $3kV$ when operating the cathode at $300kV$.

The CERN group will work on the construction of the field cage for both the single and dual phase

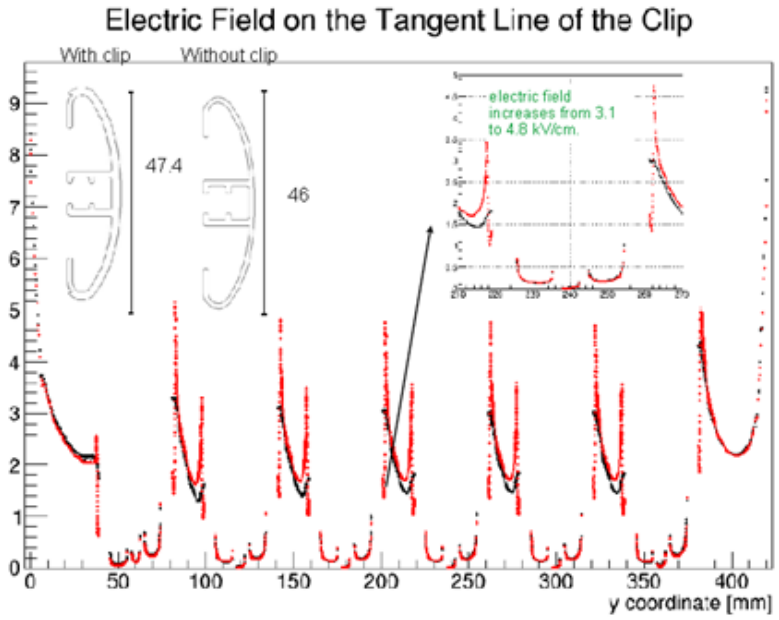

FIG. 45: Simulations of the electric field in proximity of the extruded field cage profiles and of the clipping profiles (blue and purple)

FIG. 46: Mechanical mock-up used at CERN to test the shape of the clipping profiles and the functionality of the field cage electrical elements, as well as the trial fit and cleaning of all sub-module elements

ProtoDUNEs by producing the aluminum profiles and contributing to their assembly work at CERN. The contribution from the U.S. (University of Texas Arlington) has been defined for what concerns the procurement of the field cage FRP profiles and of the electrical elements. A global view of the detector including CRPs, field cage, cathode and photomultipliers can be seen in Figure 48.

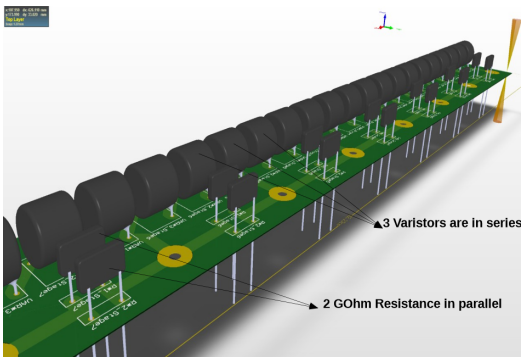

FIG. 47: One of the printed circuit boards containing the electrical elements of the field cage voltage divider. Each PCB interconnects 11 field cage rings

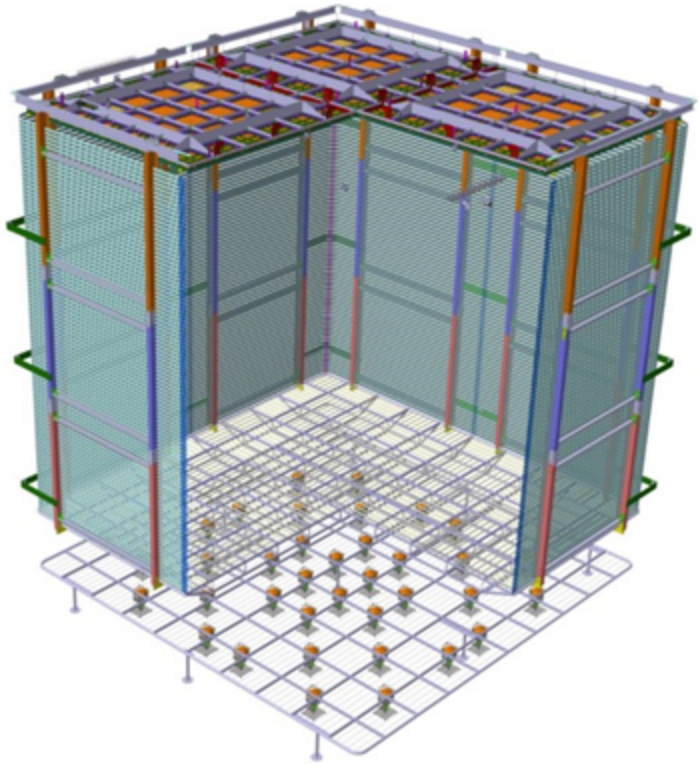

FIG. 48: Global view of the ProtoDUNE dual-phase detector elements including CRPs, field cage, cathode and photomultipliers.

4.2.5 Drift high voltage and HV feedthrough design

The high voltage system of DLAr has been already tested in LAr-Proto. The $300kV$ power supply, which will be used to generate the drift field during the first phase of WA105 operating at $0.5kV/cm$, was purchased from Heinzinger. The HV feedthrough capable of withstanding this voltage was already designed and constructed and was deployed in the fall 2016 on the LAr-Proto. Given the fact that LAr-Proto has a shorter drift space ($1m$ vs $6m$ for DLAr), a test setup with a dedicated cryostat (see Figure 49 was set up in order to perform the HV tests up to 300 kV which are needed to fully qualify

the feedthrough also for DLAr. During the HV tests the pressure in the dewar was kept stable at 1.05 bar and O_2 impurities measured in the gas were less than $0.1ppm$. This major milestone of a successful operation of the HV system at $300kV$ was achieved in September 2016 [7].

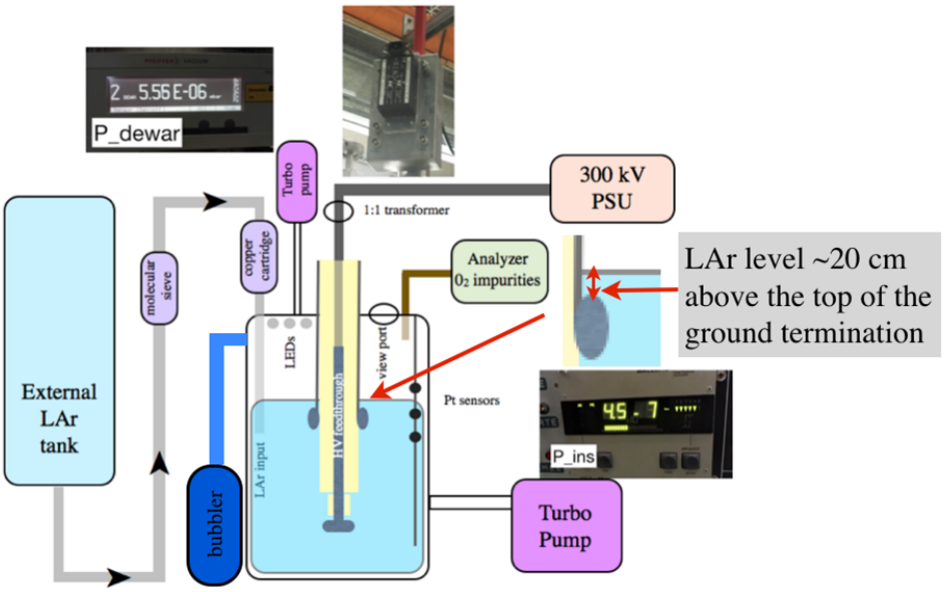

FIG. 49: Dedicated cryostat setup in order to tests the HV feedthrough at $300kV$.

The HV FT design activity and the configuration of the test setup were accompanied by dedicated electrostatic simulations in order to identify the regions with the highest fields and therefore most critical for the possible production of sparks related to formation of gas bubbles in the liquid argon. As shown in Figure 50 the highest field values are localized around the feedthrough neck, where the found conductor ends.

The procurement of the HV power supply and of the HV feedthrough are a point of synergy with ProtoDUNE single-phase which benefits of all these HV developments performed for the dual-phase.

4.2.6 Front end readout electronics design

The charge readout electronics for the DLAr entered in production phase by the end of 2015. The final version of the double-slope cryogenic ASIC amplifier (16 channels; 1200 fC dynamic range; slope kink at 400 fC, equivalent to 13 m.i.p for a LEM gain of 20) was submitted to CMP in September 2015 and tested in January 2016. Some improvements were introduced in the design of the MOSCAP capacitor which is used in the feedback branch of the operational amplifier in order to achieve a double-slope regime. A new differential driver was integrated in the ASIC as well. The entire cryogenic amplifiers ASIC production needed for DLAr, a total of 700 chips including spares, was performed in

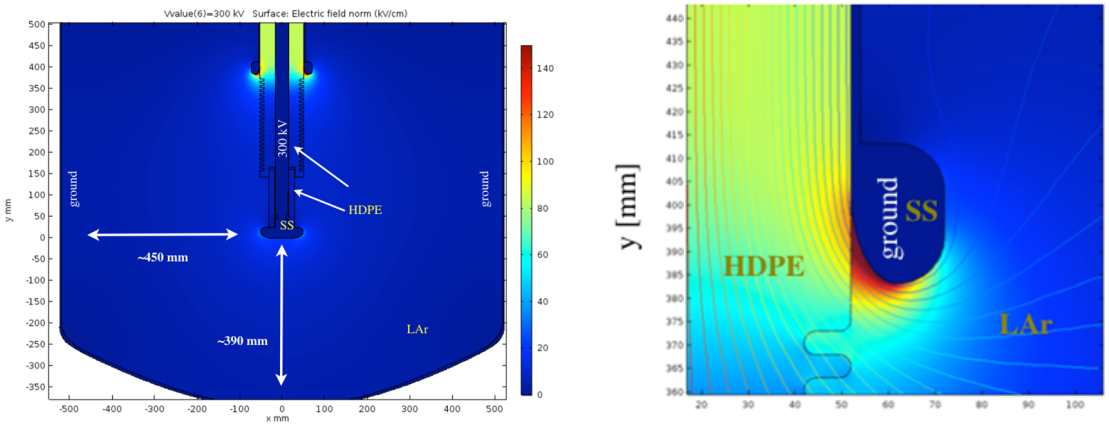

FIG. 50: Electrostatic simulations of the HV feedthrough test at $300kV$ in the dedicated test setup (left), the highest field region corresponds to the feedthrough neck where the ground conductor stops (right).

the September 2015 0.35um CMOS run at CMP with a purchase option on the entire batch of circuits upon satisfactory tests on an evaluation batch of 25 circuit to be conducted in January 2016. These evaluation tests were then satisfactory and led to the availability of the complete set of circuits needed to instrument DLAr.

Figure 51 shows the final version of the double-slope ASIC cryogenic amplifier mounted on a test card. Figure 52 reports the noise characterization of this version of the ASIC, measured before a final shaping stage implemented on the microTCA digitization cards. This characterization has been performed at different temperatures as a function of the input capacitance.

FIG. 51: Final version of the double-slope cryogenic ASIC amplifier submitted for production in October 2015 and tested at the beginning of 2016.

The design of the front-end cryogenic cards hosting the ASIC amplifiers to be inserted in the signal chimneys was completed by May 2016. Each card hosts 4 ASIC chips for a total of 64 channels per card as well as passive components before the preamplifier input. These components include for each channel a bias resistor, a decoupling capacitor and a surge arrestor component made by a diode pair. The surge arrestors for protection against LEM sparks were selected after a long qualification

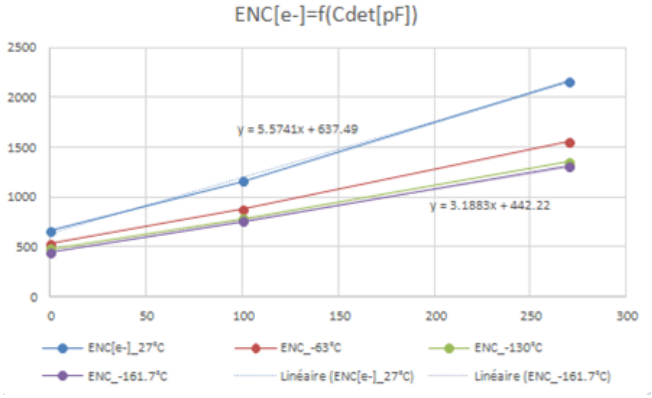

FIG. 52: Noise characterization of the final version of the double-slope cryogenic ASIC amplifier.

campaign with intensive sparking stress tests. All these passive components are rated for HV operation. A preproduction of 22 front-end cards was performed in order to equip the LAr-Proto detector which uses 20 cards in 4 signal chimneys for the readout of 1280 channels (see Figure 53). These cards were installed on the LAr-Proto detector in September 2016 and are fully operational since that time. The full production of the remaining 100 analog front-end cards needed to equip DLAr is being launched with the 2017 budget. The insertion and extraction operations of the front-end cards in the signal chimneys they have been routinely performed without problems in the fall 2016 on LAr-Proto (see Figure 54).

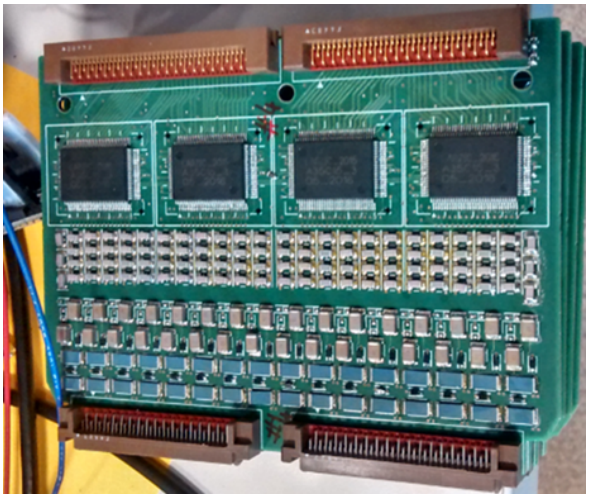

FIG. 53: 64 channels front-end cards, hosting 4 ASIC cryogenic amplifiers, already operational on LAr-Proto

The conceptual design of the front-end microTCA digital electronics was completed in 2015 basing on a 64 channels AMC demonstrator digitization card produced at the beginning of 2015. This card was containing already the final ADC circuitry, based on the ADCs AD5297, plugged as mezzanine card on a Bittware SA4M microTCA development kit. This demonstrator circuit allowed to correctly dimension the FPGA and the firmware for the final AMC digitization cards. The DAQ scheme and data

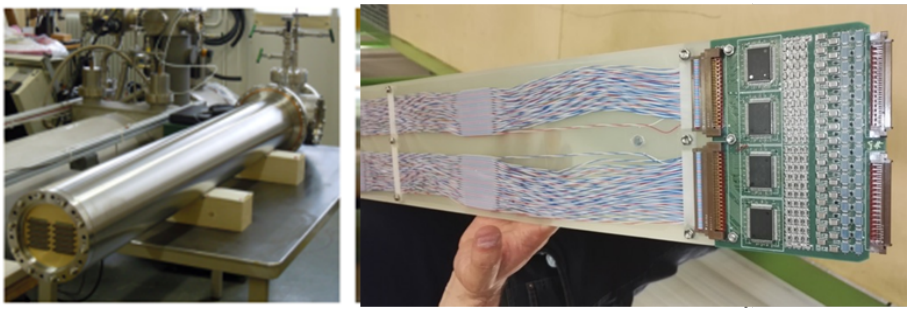

FIG. 54: Analog front-end card mounted on an insertion blade for installation in a signal chimney on LAr-Proto

transmission over 10 Gbit/s Ethernet were fully tested as well. The experience with the demonstrator card led to freeze the design of the final microTCA cards and to start their production by the fall of 2015. All the main components for the final cards such as the FPGA (Cyclone V GX, 120 pieces), the dual port memories (IDT70V3339, 240 pieces) , and the ADCs (AD9257BCPZ-40, 8 pieces/AMC card, 1040 pieces) were purchased in the final quantities needed for the entire DLAr production. The routing of the final PCB of the microTCA digitization cards was completed on May 2016 and, similarly as for the production of the front-end cards a preproduction batch of 22 cards in order to equip LAr-Proto was available in August 2016 (see Figure 55).

4.2.7 DAQ system design

The DAQ system of LAr-Proto, including 20 digitization cards in 4 microTCA crates was fully commissioned by the beginning of December 2016 and it is still operational on LAr-Proto at the moment. Figure 56 shows one of the 4 microTCA crates installed on LAr-Proto and Figure 57 provides an overview of the installation after installing the VHDCI cables which are used to transmit the analog signals in groups of 32 channels from the warm flanges of the signal chimneys. The operation of the system on LAr-Proto provided also some direct experience on the global grounding and noise conditions of the experiment. Figure 58 shows (red points) the RMS noise as a function of the channel number in the final configuration with all electrical connections in place from: the slow-control system, HV system and CRP motorization system. The noise conditions correspond to a RMS noise averaged on all channels of 1.7 ADC counts. Measurements were taken also with all electrical connections disconnected, but the ones of the analog front-end electronics and DAQ. In that case the RMS noise averaged on all channels was corresponding to 1.5 ADC counts (black points in Figure 58), quite close to the nominal noise of the amplifiers in warm conditions. The slightly worse performance with everything connected is related to small residual grounding issues. The grounding scheme for the $6\times6\times6$ m^3 will be different than the one of the $3\times1\times1$ m^3 since all the slow control electronics will be referred only to the cryostat ground and insulated with respect to the external environment, this scheme should provide better

grounding conditions. In any case the noise conditions achieved with the $3 \times 1 \times 1\ m^3$ installation are quite good and close to expectations with a very robust S/N ratio. The expected signal corresponding to a charge of $30fC$ at the preamplifier input (m.i.p deposited charge of $3fC$ per strip and LEM gain of 20, corresponding to an effective gain of 10 with equal sharing of the charge among the two collection views) is around 200 ADC counts.

The full production of the remaining 100 digitization cards needed to equip DLAr will be launched with the 2017 budget in order to have the cards available for installation by October 2017.

FIG. 55: 64 channels microTCA digitization cards. A preproduction sample of 20 cards is currently operational on LAr-Proto.

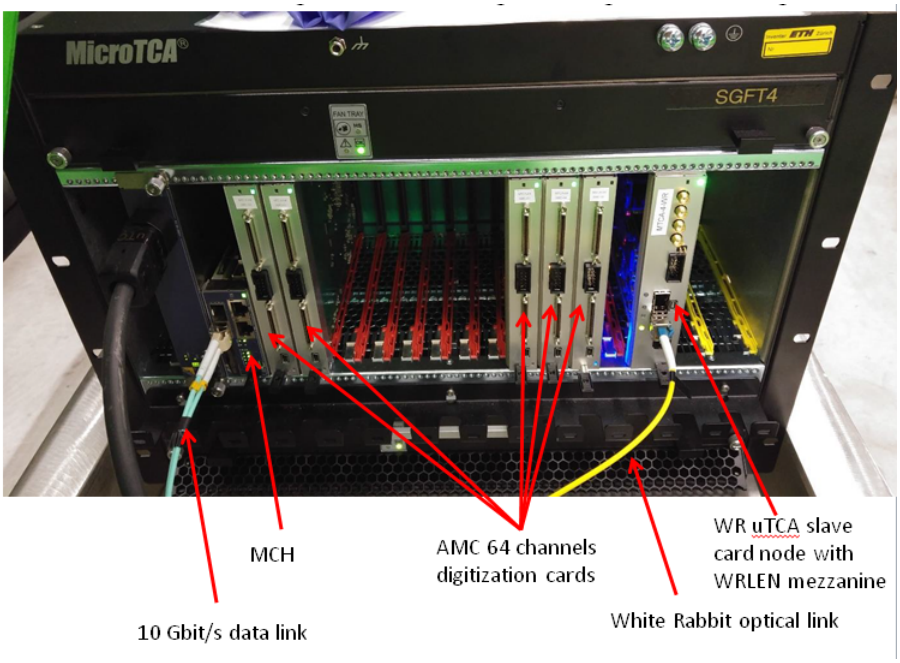

FIG. 56: Picture of a microTCA crate operational on LAr-Proto, taken just before connecting the VHDCI signal cables going to the warm flange of the signal chimney. Each microTCA crate in LAr-Proto hosts 5 AMC digitization cards and the White-Rabbit slave node for timing/triggering. The number of AMC cards per crate in DLAr will be 10.The data and timing/trigger connections go only via optical fibers.

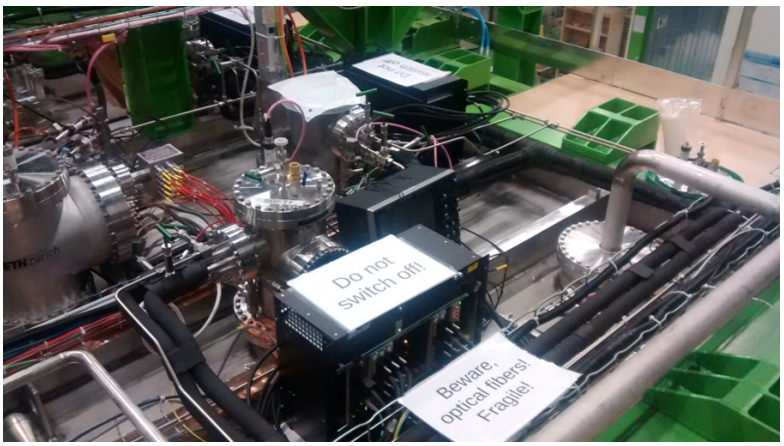

FIG. 57: Overview of the front-end installation on LAr-Proto.

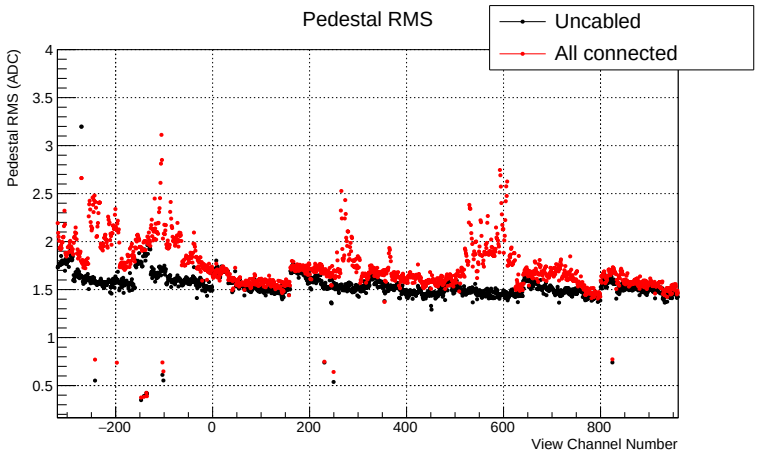

FIG. 58: Distribution of the RMS noise as a function of the readout channel number: (black) with slow control and HV connections uncabled, (red) full system cabled.

The time and trigger distribution system based on the White-Rabbit (WR) standard was also defined in 2015. It is based on commercial components from Seven Solutions (WR Grand Master switch, time tagging cards SPEC and FMC-DIO and slave cards WR-LEN). The WR-LEN slave cards have been adapted to microTCA format by developing a specific card and their firmware was reprogrammed accordingly in order to generate the synchronization/clock and trigger signals needed by the microTCA digitization cards.

These microTCA White-Rabbit cards were produce in June 2016 (see Figure 59). A timing/trigger distribution protocol was defined in order to distribute these two signals on the backplane of the microTCA crates to the AMC digitization cards. Signals from the beam counters and cosmic ray counters can be timestamped with a slave White-Rabbit card. These timestamps can be then made accessible via the White-Rabbit data network to all the AMC digitization cards. The same treatment can be performed for the timestamps corresponding to the start of the beam spills which are tagged

with a different trigger id. The microTCA digitization cards can then be aware if they are taking data during or outside of the beam spills and can therefore adopt different triggers priorities in these two cases. The entire timing system for the DLAr was procured in 2016. A subset including the GPS timing source (Meinberg M6000), the White-Rabbit Grand Master, 4 microTCA slave clock cards and the trigger PC with the time-tagging cards was installed on LAr-Proto and became fully operational in November 2016. It is currently being exploited for the LAr-Proto data taking. Figure 60 shows the rack hosting the timing system already deployed on the LAr-Proto including the GPS receiver, the White-Rabbit grand master and the trigger PC.

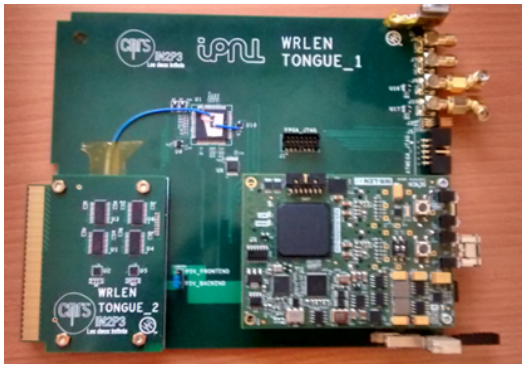

FIG. 59: microTCA White-Rabbit slave card for timing and triggers distribution

FIG. 60: Full timing/trigger system already deployed on LAr-Proto including the GPS receiver, the White-Rabbit grand master and the trigger PC hosting the White-Rabbit time-tagging card

Figure 61 provides a general overview of the integration scheme of the DAQ/ timing-trigger distri-

bution system of ProtoDUNE dual-phase.

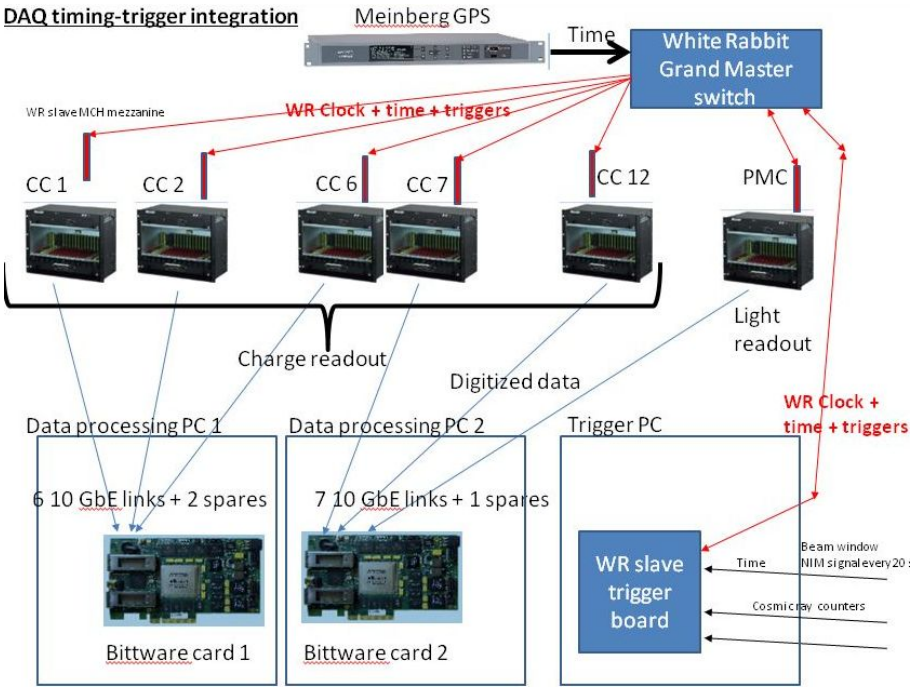

FIG. 61: General DAQ/timing/trigger integration scheme of ProtoDUNE dual-phase

The event building Back-end cards are connected to the online storage and processing facility which was described in details in the 2016 yearly SPSC report.

A reduced scale test version of the online storage and processing facility (see Figure 63), including 300 cores and 240 TB disk space, has been already implemented on the LAr-Proto in order to perform tests and optimize the software and hardware design for the final DLAr implementation of the online storage and processing facility. This smaller scale test system, including a batch system capable of reconstructing in real time the events from the DAQ and of performing a measurement of the purity and gain and a distributed local storage based on EOS had been fully commissioned with simulated events in December 2016. In January 2017 the online storage and processing facility of LAr-Proto was systematically transferring the commissioning data of the noise measurements to the central CERN EOS system for offline analysis. The event format for the $3 \times 1 \times 1\ m^3$ uncompressed data foresees the storage of 335 events per file, in files of about $1GB$ size. The architecture of the already implemented online storage and processing facility and its evolution to the DLAr version are discussed in details in the offline and computing session.

The event building software and run control interface were developed for the LAr-Proto operation (see Figure 62).

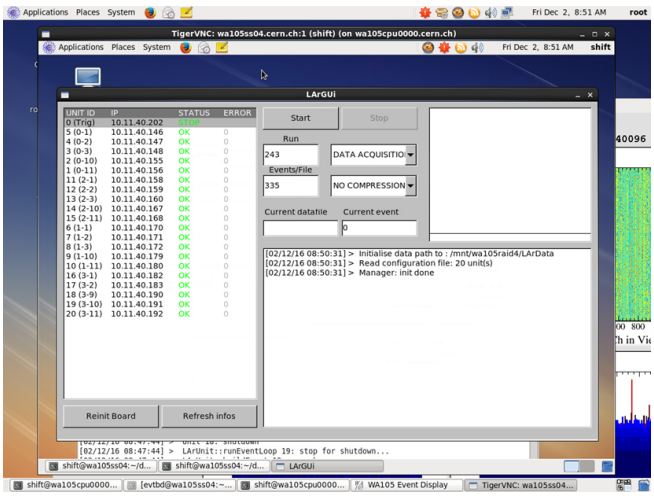

FIG. 62: Run control interface to event builder operational for LAr-Proto.

FIG. 63: Reduced scale version of the online storage and processing facility already operational for LAr-Proto.

4.2.8 Light readout design

The Light ReadOut (LRO) electronics implies the digitization of 36 photomultipliers. This front-end electronics is based as well on the microTCA standard. The digitization cards have a trigger mezzanine card which is based on the PARISROC ASIC (see Figure 64). The digitization scheme is based on an adaptation of the microTCA developments performed for the charge readout DAQ system.

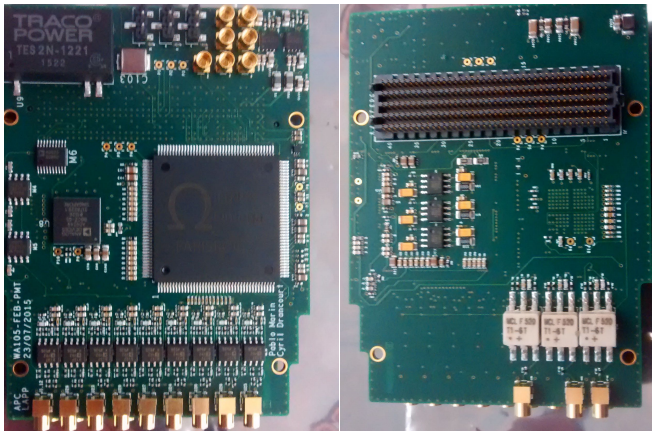

FIG. 64: Light readout front-end mezzanine card.

The LRO is fully integrated in the general microTCA DAQ scheme defined for the charge readout, including the timing and trigger distribution scheme. During beam spills the LRO electronics will produce data with 400 ns time granularity in the 4 ms windows before and after each beam trigger in order to allow for the reconstruction of the drift coordinates of the cosmic ray tracks which are overlapped to the beam events. The cyclic memory buffers on the LRO digitization cards have enough depth in order to implement this readout scheme. Outside beam spills the LRO can be used in self-triggering mode or in conjunction with triggers generated by the large area cosmic triggers. The LRO electronics design is being finalized in view of its deployment in the DLAr and it is not currently used in the LAr-Proto, where the light readout system is very simple and essential, given the dimensions and the purpose of this detector. A new version of the mezzanine card is currently designed, the routing of the circuit is finished and the software is being written. The production is expected for end of April, 2017.

4.2.9 Slow control design

The slow control system successfully developed for the LAr-Proto has been scaled up for its application for DLAr. The equipment used for the slow control readout of LAr-Proto will be transported to EHN1 at the end of the LAr-Proto operation and integrated in order to set up the final system for DLAr. This task is under the responsibility of the CERN group which is in charge of the installation of the slow-control systems for both ProtoDUNEs. The slow-control synergy as the one based on the HV system has been helpful to the single-phase Proto-DUNE.

4.3 Installation procedure and general schedule

The activity in 2016 focused on finalizing the executive design of the DLAr, taking into account what was learned from the prototyping activity for the LAr-Proto and by considering all the aspects related to the design of the $10kton$ dual-phase detector modules at SURF. The DLAr will allow performing a final test of the detector elements foreseen in the $10kton$ design, implementing a construction chain and procedures which could then be extended to the production needed for the $10kton$, including all the QA/QC procedures. This part of the design activity was conducted in collaboration with the DUNE Far Detector working group and the LBNF management.

The Charge Readout Plane (CRP) is the basic element of the dual-phase design. It integrates the $50 \times 50\text{cm}^2$ LEM-Anode sandwiches and the extraction grid on a support frame which is hung on a suspension system allowing to adjust its height and planarity with respect to the LAr surface. The CRP design for the DLAr was adapted in order to include the $3 \times 3\text{m}^2$ CRP modules defined in the DUNE Conceptual Design Report for the 10 kton dual-phase detector. The DUNE 10 kton module is foreseen to include 80 CRPs in order to instrument a detection surface of $12 \times 60\text{m}^2$. Similarly the DLAr will use four (4) $3\times3\text{m}^2$CRPs. The DLAr will therefore implement all the production procedures of the CRPs and will validate their operation as a final engineering test for the $10kton$.

Following these developments we have then defined a construction procedure in the EHN1 area which mimics as much as possible the underground installation procedure at SURF. For the $10kton$ far detector modules, in order to minimize the underground work and simplify the installation, the CRP planes will be completely pre-assembled and quality controlled at the production sites. The CRP modules will be then transported to SURF, down to the underground site in customized boxes of $3.2 \times 3.2 \times 0.5\text{m}^3$. These boxes will be inserted in the cryostat via a vertical TCO, thanks to a rail system fixed on the exoskeleton structure. The TCO is externally surrounded by a clean room buffer and a SAS for the introduction of the box. The rail manipulation system will include a tool in order to rotate the transportation box from the vertical to the horizontal position. Once the box is in a horizontal position it can be transported with a platform equipped with wheels just below the CRP installation position. One can then proceed from this position to the hanging of the CRP. The connections of the CRPs to the electronics can be performed once the CRP has almost reached its nominal height. The TCO and clean room buffer scheme have been integrated in the conventional facility definition of LBNF.

For the installation of DLAr the CRPs will be pre-assembled in the clean room in building 185, used so far by WA104 for the T600 refurbishing. This clean room will became available in April 2017. It is a clean room class 10k with inner dimensions of $20(l) \times 5(w) \times 4.8(h)\text{m}^3$. This location provides

all the necessary space for the CRPs assembly, metrology and quality controls and their insertion in the transportation boxes. Figure 65 shows a sketch of the CRP assembly chain foreseen to be installed in the clean room of building 185.

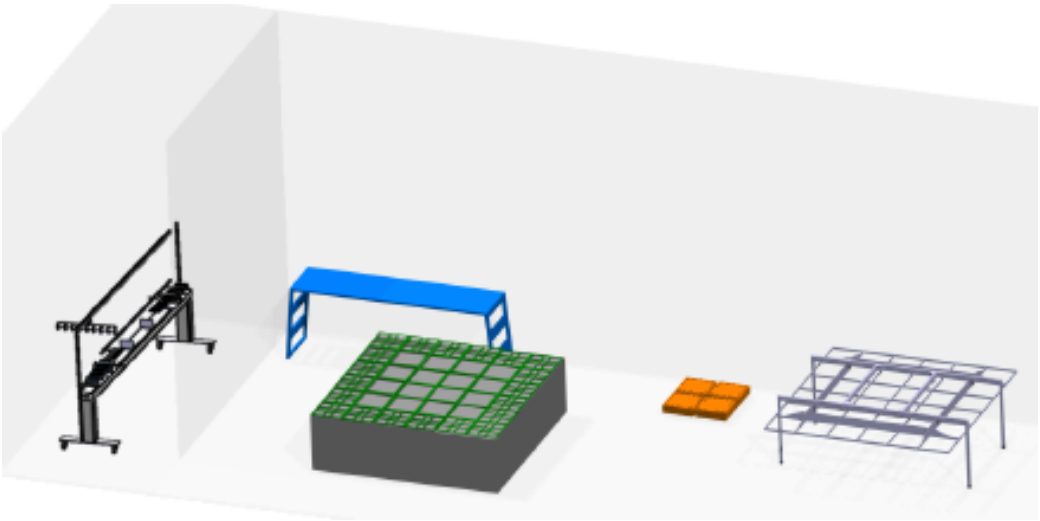

FIG. 65: CRP assembly chain in the clean room of building 185.

The cryostat of WA105 will be connected via its TCO to a Clean Room Buffer(CRB) of about $6(l) \times 5(w) \times 4(h)\mathrm{m}^3$ built inside the EHN1 pit area (see Figure 66). The TCO dimensions and its position on the cryostat face relative to the pit shape were optimized by taking into account this detector assembly scheme. Also the CRB at EHN1 is designed for a vertical transportation of the boxes containing the detector elements via a SAS on its roof. The CRPs will be as well introduced vertically in the cryostat with a transportation rail and then rotated, as foreseen for the final installation in the $10kton$. Figure 67 shows details of the integration to the cryostat exoskeleton of WA105 of the installation rail for the CRP boxes.

Once the CRP have been installed and connected to the flat cables coming from the signal chimneys, the installation of the field cage which is hanging as well from the top of the detector is performed. Some temporary installation ropes going through the field cage suspension feedthroughs allow progressively to assemble the field cage sub-modules in the final vertical modules by operating from the cryostat floor. The last steps of the installation consist in the mounting of the cathode and of the ground grid. The ground grid is suspended in a temporary position in order to allow for the PMTs installation on the cryostat floor and then released to its final position once the PMTs have been installed and cabled.

The WA015 installation schedule has been revised by taking into account the latest input from the CERN Neutrino Platform on the the final availability of the clean room in hall 185 and of the cryostat for detector installation as well as the impact of the LAr-Proto operation delay. Other important elements of this schedule revision are the executive design of the CRP field cage and cathode, which

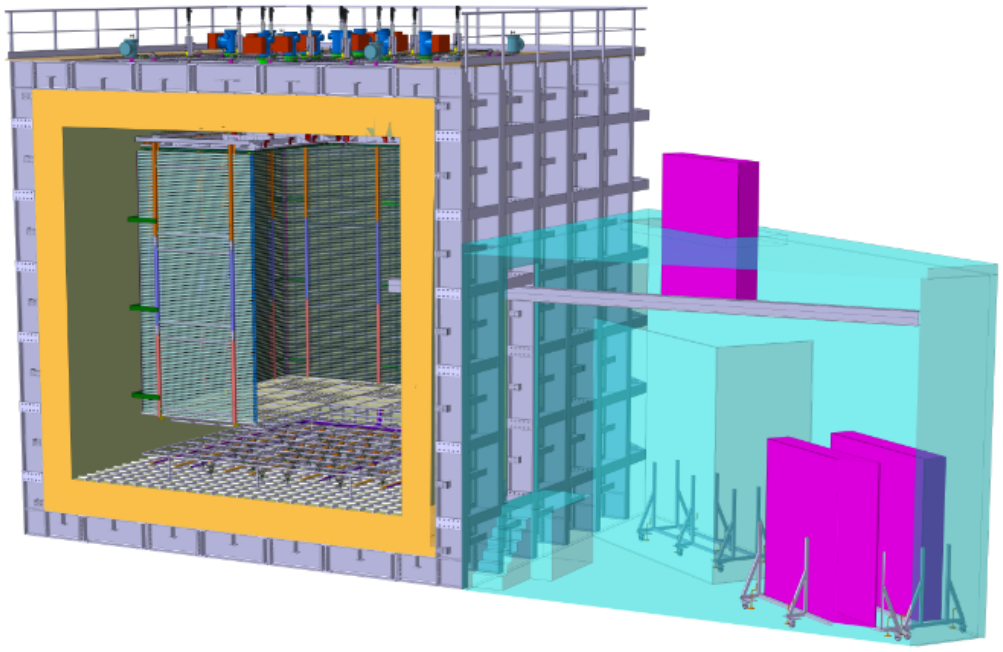

FIG. 66: Clean Room Buffer connected to the dual-phase cryostat TCO.

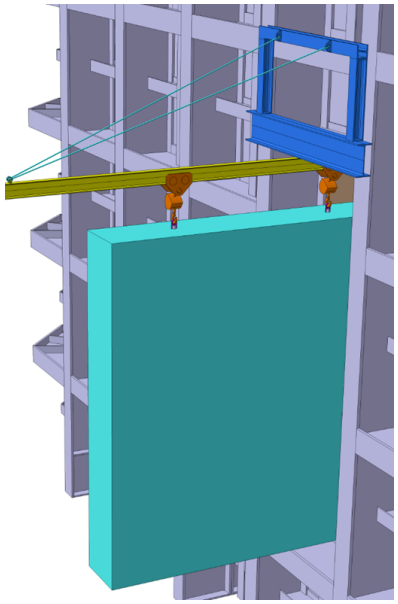

FIG. 67: Installation rail for the insertion of the CRP boxes in the WA105 cryostat via the TCO

was finalized in the fall 2016, and the detailed construction/installation sequence related to it and the experience acquired during the integration of the LAr-Proto detector. This revised schedule foresees the completion of the detector installation by February 2018. The main milestones of the schedule for what concerns the detector installation are reported below

- Start of CRP production/assembly: 10/3/2017

- Access to clean room in Hall 185: 11/4/2017
- Access to cryostat/clean room buffer in EHN1 to start the detector installation: 1/6/2017
- First CRP installed: 8/8/2017
- All CRPs installed and cabled: 8/11/2017
- End of readout electronics installation 1/12/2018
- End of drift cage and cathode installation: 15/1/2018
- End of PMTs installation: 5/2/2018
- End of beam-plug installation: 14/2/2018
- Detector fully installed and cabled, ready to seal TCO: 19/2/2018

The full WA105 installation and commissioning schedule is separately available as support document for this report.

By taking into account the final beam-line simulations, mentioned above, and this refined schedule, the beam-requests for 2018, already formulated in the 2016 SPSC yearly report, are maintained also in this report. They correspond to a total beam time allocation for protoDUNE dual-phase on the H2 beam line of 59(positive) and 59(negative) days, or about 17 weeks of running in 2018. Running with cosmic rays is foreseen in 2019, as also discussed in the previous report.

Possible needs for operation during LS2 and the possibility of operation beyond LS2 for both ProtoDUNE detectors have been as well presented in a document sent by Mark Thomson to the SPSC in February 2017 in the framework of a discussion concerning ProtoDUNE-SP [13]. The considerations presented in that document are applicable to both ProtoDUNE-SP and ProtoDUNE-DP detectors by describing the motivations for a possible operation after the end of 2018 and the related benefits to the DUNE project connected to completion of the ProtoDUNEs physics program with the beam-line operation after LS2 and to the mitigation of risks for long term operation of the detectors. The needs for a possible completion of the physics program will be dependant on the beam time which will be really exploited in 2018 with respect to the requests formulated.

5 Software and data analysis developments

5.1 Overview of software and computing

Over the last year, a significant refinement of the ProtoDUNE dual-phase simulation and reconstruction tools has been conducted to ensure the necessary requirements for the data analysis of ProtoDUNE

dual-phase are satisfied.

In this chapter, progress on the development of the simulation and the reconstruction software (Section 5.2 and Section 5.3), readiness of online processing and monitoring system (Section 5.4), and the status of the implementation of the dual-phase Liquid Argon TPC detector concept in LArSoft (Section 5.5) are described.

5.2 Progress in charge signal simulation and reconstruction

5.2.1 Electric field map

While nominally a uniform homogeneous field of 0.5 kV/cm strength is assumed, a mechanism to simulate effects of field non-uniformities has been developed by using finite element analysis calculations in COMSOL. An arbitrary field configuration based on the numerical calculations using COMSOL can be specified via a list of 3D nodes (voxels) each corresponding to a volume element inside the active TPC. These define a specific field value in that region as well as the drift time, position at the anode, and the magnitude of the diffusion pre-calculated in advance. We have prepared field maps that include field distortions induced by accumulation of Ar^+ inside the active TPC volume and are studying the methods to measure and calibrate these effects with the cosmic ray muons.

Detailed COMSOL simulations for the LAr-Proto and DLAr detectors have been performed with different configurations: nominal applied electric field set at 0.5 kV/cm and 1 kV/cm and ion back flow rate (IBF) from the charge multiplication in LEMs at 0% and 10%. The three-vector components of the electric field are stored on a grid of $10 \times 10 \times 10$ cm^3 voxels for the LAr-Proto detector, and $20 \times 20 \times 20$ cm^3 voxels for the DLAr detector. The electron path and drift time to the anode from a given voxel is computed using path integration with steps of 1 mm. To smoothly vary the field values the components of the electric field are linearly interpolated between nearby voxels.

The drift trajectories of electrons produced near the cathode and the mean value of the z component of the electric field are shown in Fig 68 for the DLAr detector. In these plots, the underlying field map was calculated assuming a nominal field strength of 500 V/cm and 10% IBF rate.

Results of the COMSOL field calculation after they are translated to the field map are utilised in the WA105 software. Figure 69 shows the CRP projections of a 3 GeV/c muon crossing the DLAr detector which were simulated with different field configurations.

Similar to the anode position and the arrival time, the magnitude of the transverse and longitudinal diffusion at CRP for electrons originating at a given point in the detector are obtained from the path integration along the entire electron drift trajectory. Figure 70 illustrates the sizes of the simulated diffusion effects at the CRP for electrons produced near the cathode of the DLAr detector.

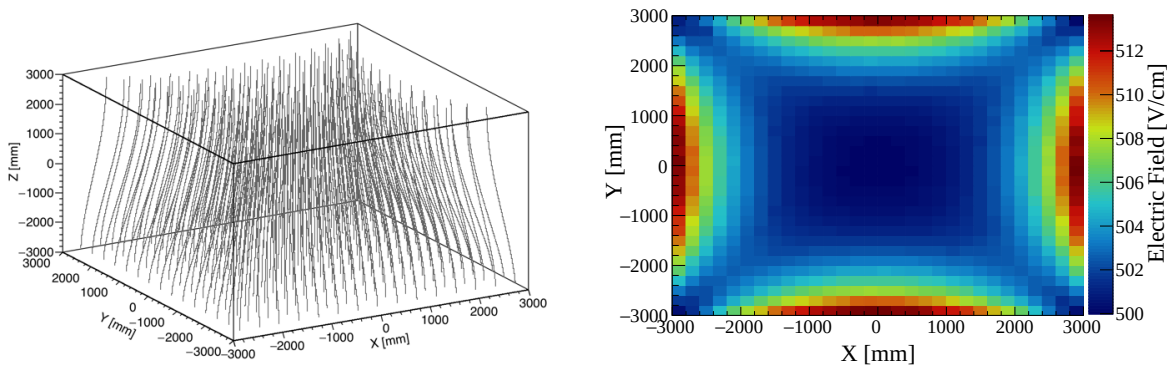

FIG. 68: Left: Drifting electrons trajectories from the cathode to the anode when a 500 V/cm field map is used assuming 10% ion back flow. Right : x-y mean electric field along z for the same field map settings. Both plots are done for the DLAr detector.

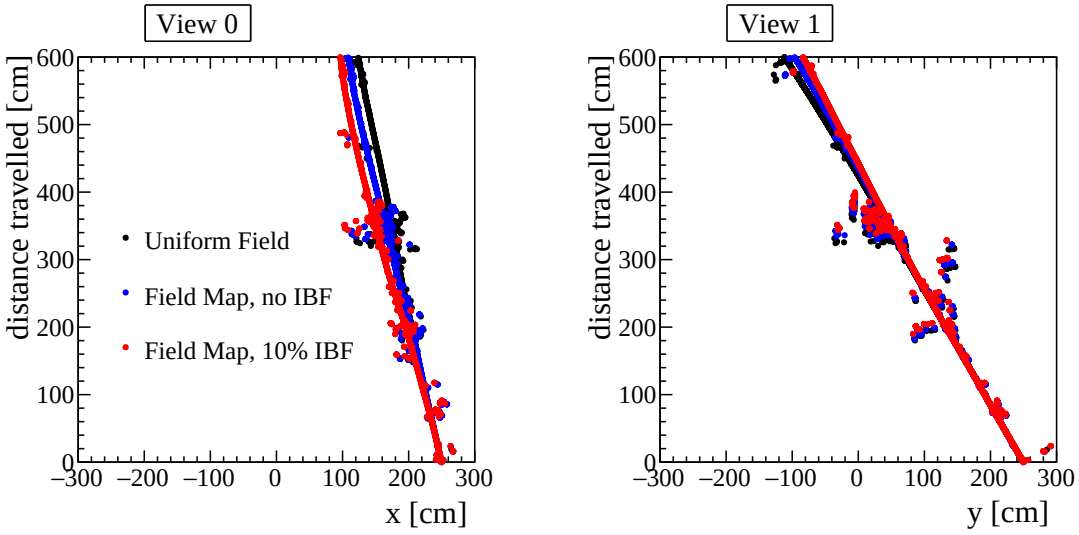

FIG. 69: 2D projections of a 3 GeV/c muon crossing the DLAr detector. Dots represent reconstructed hits. In black, when a uniform field of 500 V/cm is assumed. In blue, when the field map is used with no ion back flow. In red, when 10% of ion back flow is assumed.

5.2.2 LEM field simulation

Similar to the LAr-Proto CRP, the one of DLAr is built from 50×50 cm^2 LEMs that have a 2 mm of unplated FR4 clearance around the border followed by 2 mm wide copper guard ring as illustrated in Fig. 71. These areas along with the 29 holes for the mechanical fixation and two annular clearances for the high voltage pin connections distort electric fields in the vicinity impeding the collection of ionization electrons. To evaluate the collection efficiencies with the actual layout of the LEM PCB, a dedicated simulation has been developed. ANSYS engineering software for finite element analysis is used to perform calculation of the electrical fields in and around the LEM. These fields are then exported into the Garfield++ toolkit for the simulation of the electron drifts.

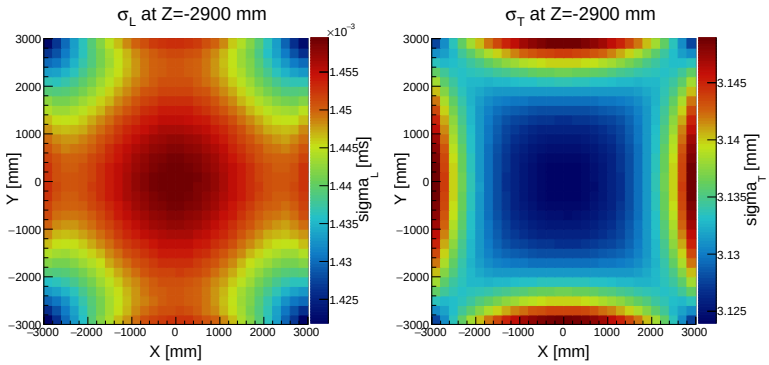

FIG. 70: Size of the longitudinal (left) and transverse (right) diffusion at the CRP simulated for electrons produced 10 cm above the cathode.

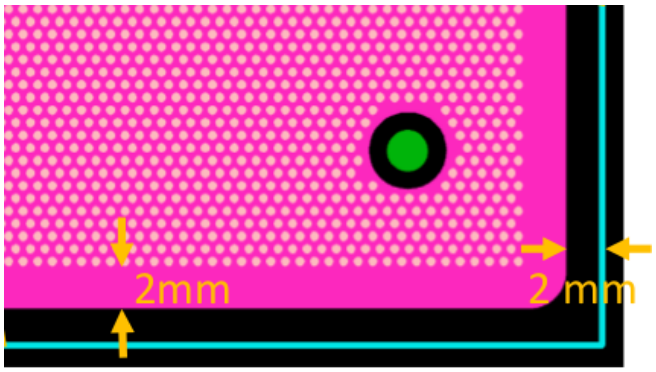

FIG. 71: A view of the LEM corner showing the 2 mm FR4 clearance followed by 2 mm of Cu guard ring. One of the holes for the mechanical fixation is also visible.

Fig. 72 shows a layout of the 2D model of the LEM that includes the unplated FR4 border and the Cu guard. The electrons originating below the dead areas do not enter the amplification region in the holes (see Fig. 72 right) and are lost on the bottom surface of the LEM. On the other hand, electrons arriving from positions within the active area enter the amplification region in the holes and, after undergoing the avalanches (not shown in Fig. 72), are collected on the anode.

The LEM electron transparency probability as a function of the distance from the LEM border (x = 0) is shown in Fig 73. All electrons arriving at the bottom face of the LEM within ~ 6 mm from the border enter the amplification gap and the induction region and, therefore, could be detected. However, the transmission probability is only about 10% for those electrons arriving around the region defined by the outermost set of the LEM holes.

A full 3D simulation of LEM electric field including the regions defined by areas around the fixation holes and the high voltage pins is under development. The resultant collection efficiency will be used to refine charge simulation in order to evaluate the effects of these dead regions on the reconstruction and detector performance.

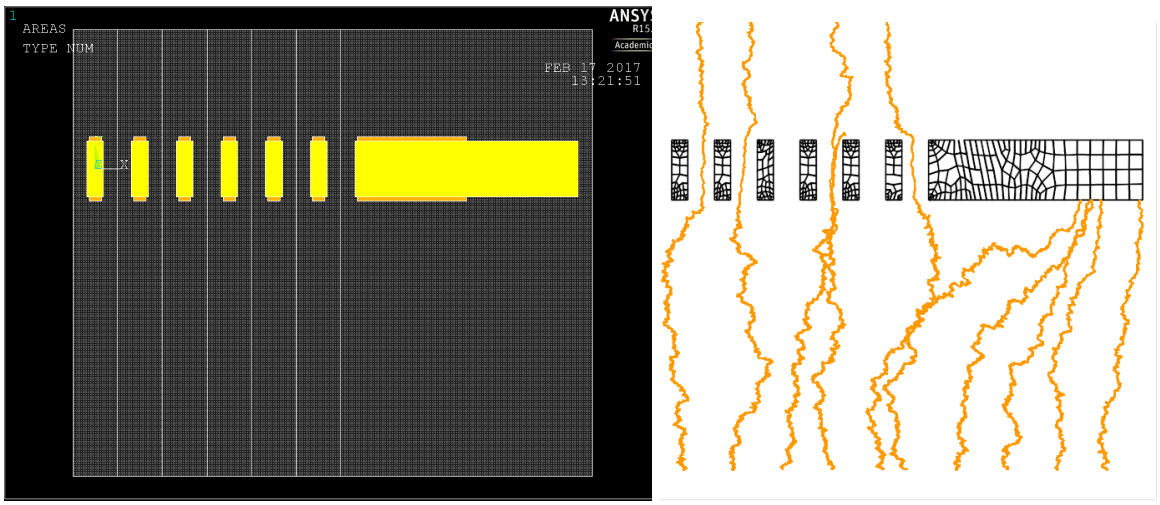

FIG. 72: Left: a 2D view of the LEM border with a first few holes. Right: illustration of the drift paths for electrons originating at different positions below the LEM.

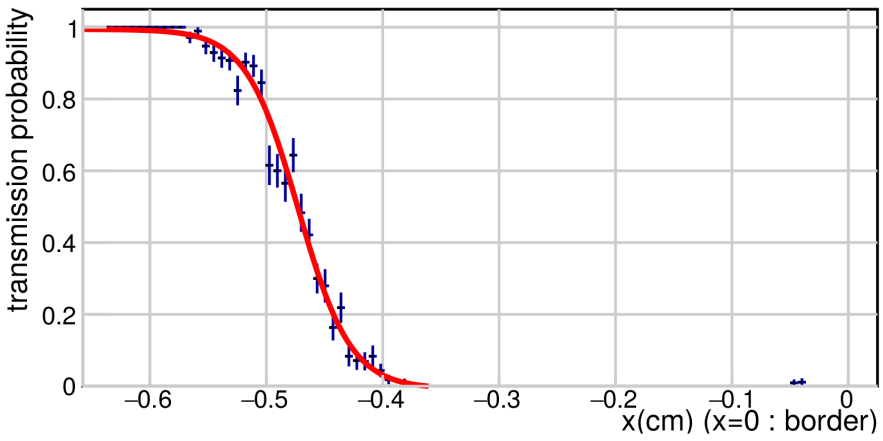

FIG. 73: Probability of electron transmission to the induction region above LEM as a function of the distance from the LEM border.

5.3 Progress in light signal simulation and reconstruction

The photon transport to the PMTs is performed by relying on pre-calculated map to avoid prohibitively long tracking of large number of vacuum ultraviolet (VUV) photons, especially caused by the high flux of cosmic muons for WA105 on-surface operation (~ 100 muons per event). This light map contains an overall acceptance factor and the parametrized information of the photon arrival time distribution from a given space point to each PMT. It is calculated once for a given detector geometry by performing a CPU-intensive tracking of a large number of photons from different positions in the detector to the PMT array.

To produce pre-calculated light maps, the photon propagation in the liquid argon to the PMTs

is performed by a dedicated software, LightSim, based on GEANT4. The VUV photon propagation includes absorption and Rayleigh scattering processes. Scattering length $\lambda_R = 55$ cm in liquid argon is assumed [14] [15]. All the components of the WA105 detector which affect the light propagation are implemented as shown in Fig. 74. Absorption on stainless steel components (electric field cage, cathode supporting structure, etc.) is assumed to be 100%. The effect of the wavelength-shifting TPB coating on PMTs is also taken into account.

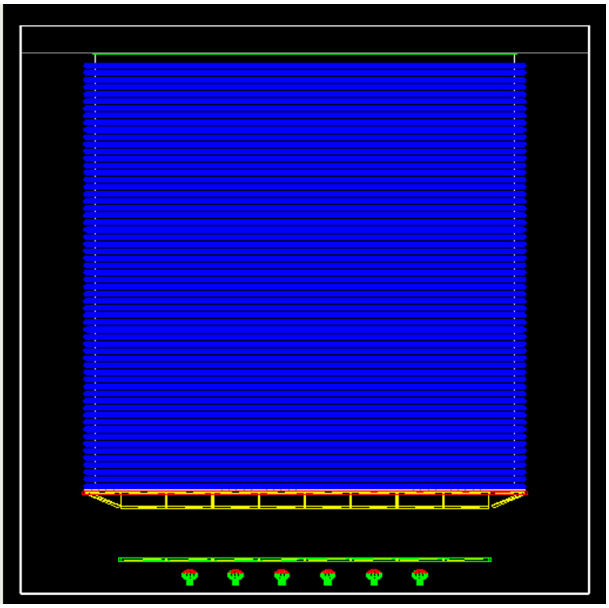

FIG. 74: Components of the WA105 detector impacting the light propagation and implemented in LightSim. Mainly : electric field cage in blue, cathode supporting structure in yellow, ground grid in green

The liquid or gas argon volume is divided into voxels for which a large number of photons ($\sim 10^8$) are generated and tracked across the detector down to the PMTs (Fig 75.a). No photon absorption in the liquid argon itself is assumed for the production of light map. Each light map contains the parameters describing the distribution of the photon travel time from a given space point to a given PMT as well as an overall acceptance factor. The arrival time distribution is parametrised with a shape of Landau function which reproduces well the simulated photon travel times as shown in Fig 75.b.

The light signals induced by the cosmic muons are studied with WA105 Software that utilizes the light map information to calculate the number of photons and the distribution of their arrival times for each PMT from a given energy deposition point. The absorption of the VUV photons in LAr is taken into account there by applying a weight for each photon based on its travel distance to the detector D_t:

$$w = \exp(-D_t/\lambda_{abs}),$$

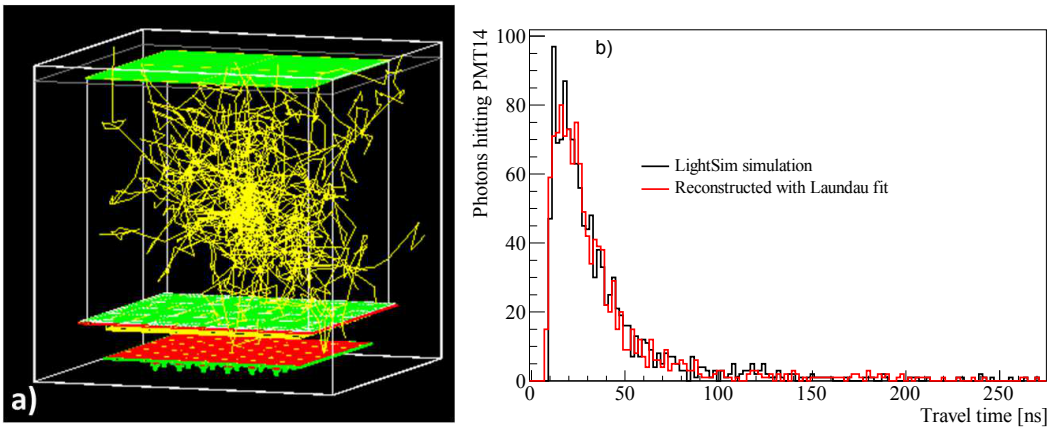

FIG. 75: a) Light propagation: Rayleigh scattering effect on the photon trajectories. b) Example of photon travel time distribution: comparison between LightSim results and a reconstructed distribution that uses the landau fit parameters.

where λ_{abs} is the absorption length.

Figure 76 gives an example of light signals summed over all PMTs in a $[-4\text{ ms}, 4\text{ ms}]$ time window around the beam trigger due to the cosmic ray background. The light yields have the contributions from the primary scintillation, S1, and the secondary, S2, from the electroluminescence in gas. The S1 contribution is shown in red in the figure. The algorithm to reconstruct muon arrival times and the total rate of the background events based on the identification of the primary S1 peak over the S2 background is under development.

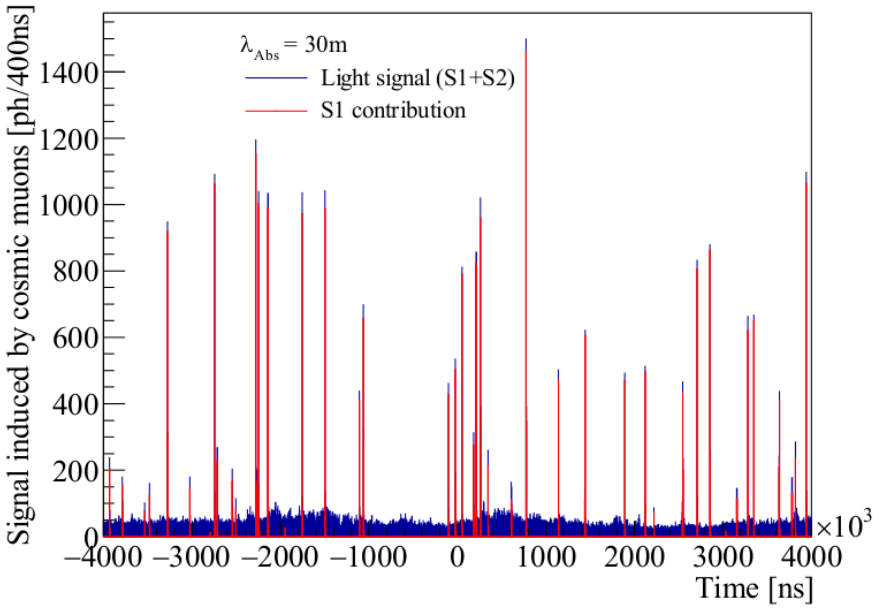

FIG. 76: Light signals generated by cosmic background events summed over all PMTs in the $[-4\text{ ms}, 4\text{ ms}]$ readout window. The contributions from S1 only is shown in red. Attenuation of length λ_{abs} = 30 m is assumed.

The LightSim is also used to find optimal configuration for the layout of the PMT array on the cryostat floor given the constraints imposed by the membrane corrugation pitch and the piping clearances. Two layouts have been studied: one with the detectors uniformly spaced and the other with PMTs non-uniformly spaced but covering a larger area (Fig. 77). Both give similar results in terms of the number of photons reaching PMTs (Fig. 77 right).

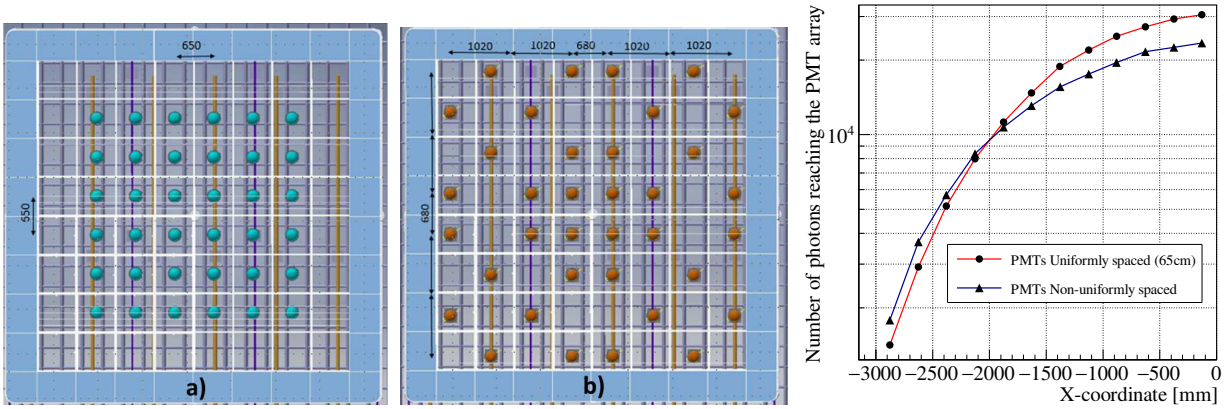

FIG. 77: Two PMT layouts and comparison of the total number of photons reaching the PMT arrays for each configuration. The photons are generated around 2m above the cathode and for various position in x.

5.4 Online processing

5.4.1 Online farm

The online storage and computing facility is a key element of the ProtoDUNE dual-phase DAQ scheme: it is foreseen to store raw data before pushing them to EOS and CASTOR in the IT division, to perform fast event reconstruction for online purity analysis and detector gain monitor, and to perform online quality data checks. The motivations to have an online processing and computing farm, the functionalities to be implemented and the requirements to be fulfilled are described in details in the 2016 annual report to the SPSC [16] .

In September 2016 a reduced scale farm has been setup for LAr-Proto. It exploits 4 dedicated storage servers, for a total size of 192 TB, and a system of batch workers including 7 CPU units corresponding to 112 available processors. The system includes also a meta-data server a batch manager and a configuration server.

TORQUE is used as resource manager of the batch system. The file-system deployed on the storage server is EOS; this has been chosen accordingly to systematic performance studies carried on a test-bench setup in April 2016 on several distributed storage file-systems [16]. EOS is of course accessible from the batch nodes. The reconstruction code together with the needed external libraries have been

installed to build the working environment. The whole setup was validated by reconstructing the same reference sample of Monte Carlo events on the farm machines and at the computing center in Lyon, and by checking that the results were identical.

A complete data processing scheme has then been developed and implemented. This scheme is mainly based on 4 steps:

1. As soon as a data file is written by the DAQ, it is immediately copied to the local EOS storage area, and it is scheduled for the transfer to the IT division, both to the CERN central EOS and CASTOR. The protocol used for the file transfer is xrootd; to strengthen the reliability of the transfer the check-sum value is computed before and after the transfer. The third party copy option is used.

2. To reconstruct the file, a script is automatically generated and submitted to the batch farm, and results are stored on local EOS as well and scheduled for transfer to CERN EOS. Depending on the raw data file-type (cosmics, pedestals or calibration events) a different processing path is followed.

3. Once the reconstruction results are available, a new script is automatically generated and submitted to the batch system to perform the purity and gain analysis, and to prepare distributions to check the data quality. A method to measure purity from muon tracks has been explicitly developed for the online analysis: it is based of relative attenuation of 2D tracks, the knowledge of the event T_0 is not needed for this task which is independent from the starting point and the direction of the track. Two measurements of the liquid argon purity level are obtained, one for view 0 and one for view 1, allowing to estimate a systematic error on the lifetime estimation. Results from purity measurement based on a Monte Carlo sample of 2000 muon tracks crossing horizontally LAr-Proto are presented in Figure 78. The code developed for benchmarking [16] is then used to build the distributions used to monitor the data quality.

4. The monitoring task is then used to display these distributions. An example in shown in Figure 79: the number of hits reconstructed for each strip, and the reconstructed charge per strip (for both view). These distributions are obtained using a Monte Carlo sample of 335 muon events.

In order to keep these four steps respectively synchronized, a set of "bridge" directories has been put in place. This structure allows each processing phase to be immediately notified when a new file is available for treatment while keeping at the same time a minimal impact on the whole system.

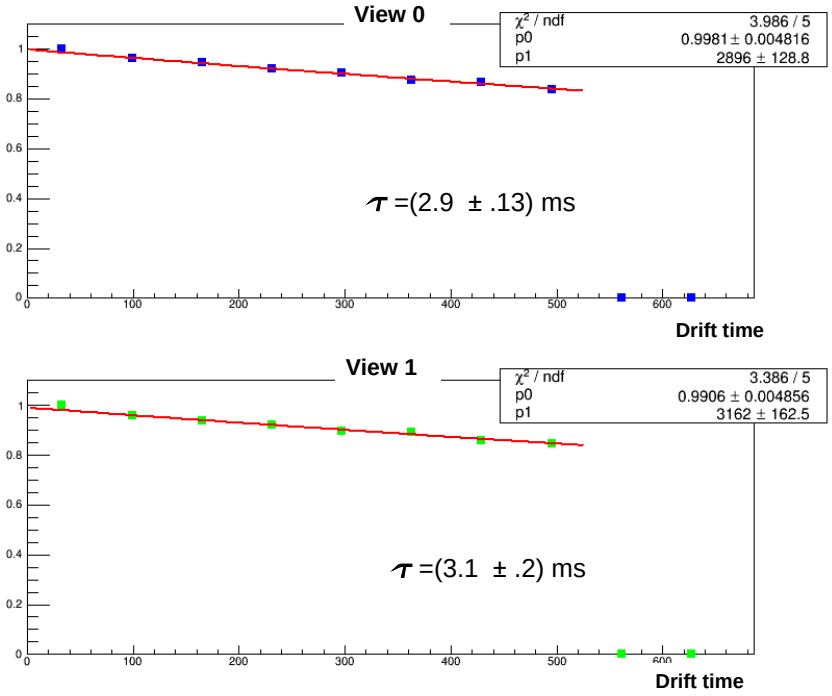

FIG. 78: Results from the online purity measurement. The two red lines represent the relative signal attenuation as a function of the drift time

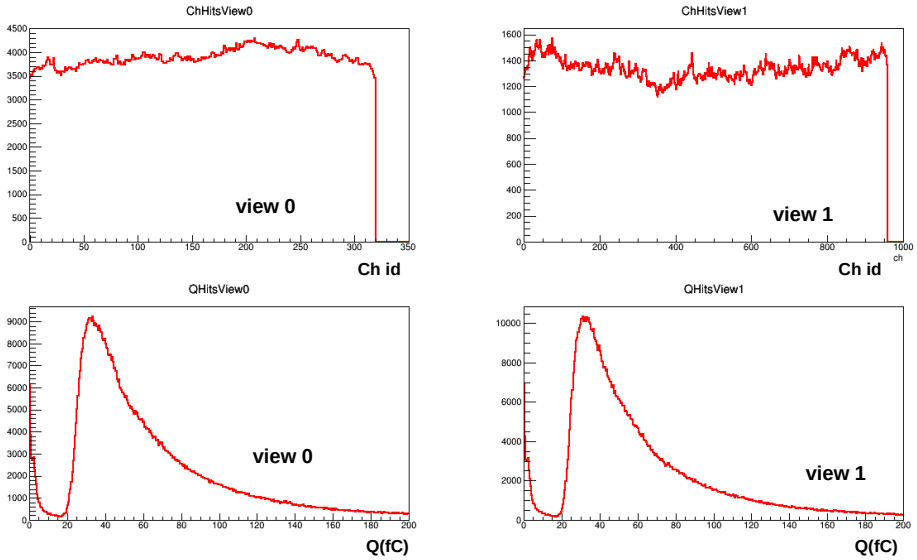

FIG. 79: Example of distribution used to check data quality obtained from a Monte Carlo sample of 335 muon events. The number of hits reconstructed for each strip and the reconstructed charge per strip are shown , for both views

To monitor the behavior and the performances of the system, different log files corresponding to each processing step are written. The general information for each run (number of events, running conditions, details of the processing steps) is available in these files. In order to access this information in a quick way, the design of an offline database, with a WEB access, is under development.

The whole data processing chain installed for LAr-Proto is working smoothly without manual interventions since the beginning of January 2107. The processing has been tested on commissioning and technical runs; files for a total volume of $\approx 400GB$ have been pushed to the central CERN EOS and CASTOR.

It is important to mention that this activity has been accompanied in parallel by a complete setup of the offline working environment at CERN on lxplus, since the storage area of the online farm is not accessible to users for offline analysis. The results from the online reconstruction and analysis are copied on CERN EOS, as soon as they become available. The code used for the fast processing on the online farm is available as well on lxplus and the CCIN2P3.

The goal of this online storage and processing farm on LAr-Proto is to validate its design and to setup and extensively test the files transfer to the IT division. This small scale farm is a test bench of the final system. The operational experience gained during the LAr-Proto data taking and by performing mock data challenges with simulated and real data are fundamental for the validation and finalization of the design of the farm for the $6 \times 6 \times 6\ m^3$.

Two mock data challenges have already been performed using simulated compressed and uncompressed data [16]. In both cases the simulated trigger rate was of $\approx$ 30Hz: the batch processing and files transfer ended smoothly. New mock data challenges will be repeated using real data from LAr-Proto. A fully costed implementation of the online storage and data processing system for the $6 \times 6 \times 6\ m^3$ was presented in [16]. The final design of the facility is in progress by taking into account the LAr-Proto experience and some technical evolutions on the network architecture and available hardware, which further improve the original design. This work is performed with the support of the CERN IT division, in the framework of the CERN IT-ProtoDUNE coordination meetings.

5.4.2 Event reconstruction for online monitoring

Hits are reconstructed with *AlgoMultiHit* algorithm [16], which searches for peaks in the data from each channel using a set of thresholds. The deposited charge is obtained by integrating the waveform in the region around the peak value and then normalizing the integral value by the calibrated response of the front-end amplifier. Mathematically a given waveform is treated as the convolution of the current

$I(t)$ induced on an anode strip by the collected charge and the amplifier response $h(t)$:

$$V(t) = I * h = \int I(t)h(t-\tau)\,d\tau \tag{5.1}$$

Since the time integral of $V(t)$ is

$$\int V(t)\,dt = \int (I * h)\,dt = \int I(t)\,dt \int h(t)\,dt, \tag{5.2}$$

by integrating Eq. 5.1 within a suitable time window around the peak value and then dividing by the normalization factor determined from the calibrated response function one can calculate the charge of the hit from the measured ADC signal $S(t)$:

$$Q_{\text{hit}} = \frac{F_{\text{ADC}}}{H} \int_{t_1}^{t_2} S(t)\,dt, \tag{5.3}$$

where the F_{ADC} is the ADC conversion factor in mV/ADC and H is integral of the response function in units of mV/fC $\times$ μs:

$$H = \int h(t)dt. \tag{5.4}$$

The reconstructed hits are clustered in space and time using nearest-neighbour algorithm based on DBSCAN within each 3×3 m^2 CRP sub-module. Splitting reconstructed hits by the submodules and then grouping them into connected clusters allows to reduce the complexity of reconstructing tens of overlapping cosmic tracks to running the track finding on just a few track segments. Those could then be stitched between the four CRP sub-modules to form the complete particle trajectory seen by the detector. This is illustrated in Fig 80. After 2D tracks are reconstructed both views are combined to find complete 3D trajectories.

The tracks are reconstructed using a 2D Kalman filter (KF). Starting from a seed of three hits that have not been yet assigned to other tracks, the filter looks for compatible hits in the nearby channels and updates the predictions with each successful search. A hit is accepted as part of the track if the predicted $\chi^2_p < 10$. This quantity is computed as:

$$\chi^2_p = (m_k - x_k^{k-1})(R_k^{k-1})^{-1}(m_k - x_k^{k-1}) \tag{5.5}$$

where m_k is the measured drift coordinate in channel k, the x_k^{k-1} is the predicted drift coordinate from previous step, and R_k^{k-1} is the predicted covariance residual matrix.

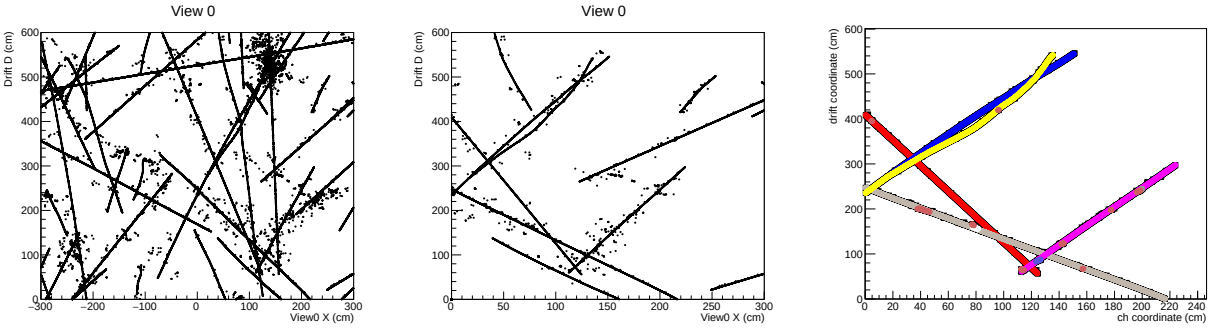

FIG. 80: Left: hits reconstructed in one views of CRP; middle: subsample of hits in 3×3 m^2 unit; right: connected hit cluster with each colour marking the hits attributed to different track segments after the track reconstruction.

The effects of multiple scattering are included as the process noise in the KF formalism with covariance matrix Q:

$$Q = \theta_0^2(1 + \tan^2\theta)^{5/2}\begin{pmatrix} 1 & 1/2\Delta \\ 1/2\Delta & 1/3\Delta^2 \end{pmatrix} \tag{5.6}$$

where Δ is step size (normally the channel pitch of 3.125 mm), $\tan\theta$ is the track slope in the given view, and θ_0 is

$$\theta_0^2 = \left(\frac{13.6 \text{ MeV}}{p\beta}\right)^2 \frac{\Delta}{X_0}. \tag{5.7}$$

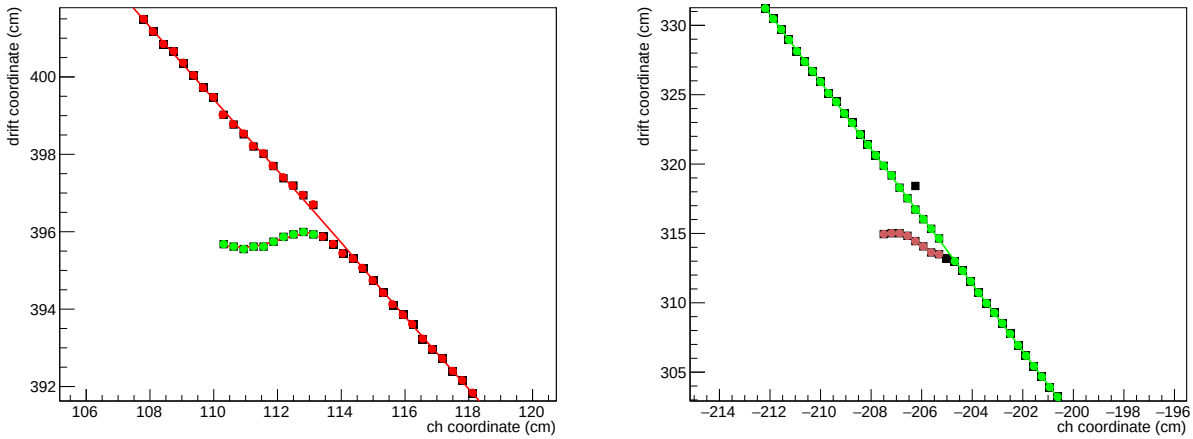

FIG. 81: Examples of track reconstruction in the vicinity of emitted delta rays.

After acquiring a sufficient number of hits, a momentum estimation is made based on the scattering

of reconstructed hit points with respect to a straight line trajectory to determine the value of θ_0. Although this is only a rough approximation to the particle momentum, the primary aim of this calculation is to allow some flexibility to treat trajectories with significant multiple scattering, such as delta ray electrons for example, without requiring changing χ^2_p cut for each track. Fig. 81 shows examples of the reconstruction of the relatively straight cosmic muon trajectories and more curved ones of the delta rays.

5.4.3 Selection of cosmics for online analyses

The analyses for online monitoring of the $6 \times 6 \times 6\text{m}^3$ detector with the cosmic rays acquired within each beam event require knowledge of the time of the arrival of a given cosmic (T_0) with respect to the trigger time. While for the LAr purity monitoring it is sufficient to work with the 2D tracks reconstructed in each view as the measurement relies on the relative attenuation of the charge within a given trajectory, the knowledge of the track T_0 would be still needed to test possible stratification of the impurities within active volume. On the other hand, the monitoring of the LEM gain stability requires the knowledge of T_0 in order to apply corrections for the charge attenuation effects as these are derived based on the drift distance from a given deposition region to the CRP.

It is possible to determine the arrival times for a subsample of the reconstructed cosmic ray tracks based on geometrical considerations. The particles that arrive before the beam trigger and exit the detector from the cathode plane, would appear disconnected at the exit point from that side in the acquired event. Therefore, for these class of the trajectories the T_0 could be calculated from the apparent distance between reconstructed end-point and the cathode. Similarly for cosmics arriving after the beam trigger and entering the TPC volume from the top, the entry point would appear to be disconnected from the CRP side. The T_0 for these trajectories could be obtained from the apparent distance between the reconstructed entry end-point and the actual position of the CRP. The reconstructed T_0 from the two classes of trajectory topologies would then be checked against the cosmic ray arrival times measured with the light readout system and the tracks for which a T_0 match is found would be selected for the analyses.

Fig. 82 shows arrival times with respect to the beam trigger ($t = 0$) in an example event populated with the cosmic ray background. The peaks in black are the true T_0 of all the cosmics entering the TPC volume within ±4 ms time window and would eventually correspond to the measurement performed on the data from the light readout system. The peaks marked in red, overlaid on the arrival time distribution, are those for which the match has been found with the reconstructed T_0 from the track topologies. To find this match a search around T_0^{reco} in a ±5 μs window is made; the size of the time

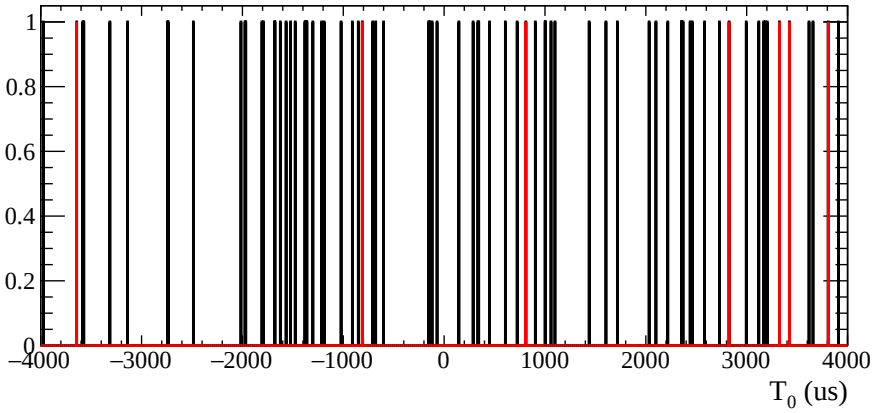

FIG. 82: Arrival times of the cosmic rays inside the detector in the ±4 ms time window around the beam trigger. The peaks marked in red are those for which the T_0 has been reconstructed from the cosmic ray track end-points and matched to the true T_0.

window corresponds to approximately 8 mm uncertainty on the reconstructed end-points.

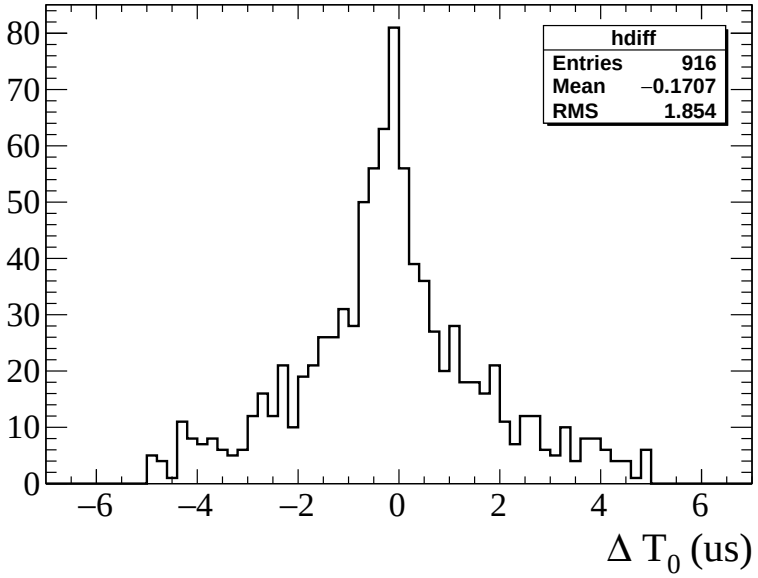

FIG. 83: Difference in T_0 reconstructed from cosmic ray track end-point information and the true value for 100 events that could be acquired in 1 s at the 100 Hz beam trigger rate.

A distribution of $\Delta T_0 = T_0^{reco} - T_0^{true}$ is shown in Fig. 83. The statistics of the histogram corresponds to the cosmics reconstructed from 100 events, which in turn is equivalent to 1 s of data acquisition time with a beam trigger rate of 100 Hz. On average about 9 cosmics could be selected for the online monitoring per event.

5.5 Integration within LArSoft framework

The LArSoft framework is being used and actively developed as a standard platform for simulation, reconstruction, and analysis of data by several single-phase LAr TPC experiments. It has also been adapted by the DUNE collaboration. A significant progress has been made on the implementation of the dual-phase detector design within the DUNE Far Detector Simulation and Reconstruction Working group. A model of the 10kt DUNE dual-phase detector geometry has been developed and the full simulation chain for the corresponding charge readout has been set up within the LArSoft environment. Tests of the LArSoft native reconstruction algorithms on the events generated within this geometry have also been performed.

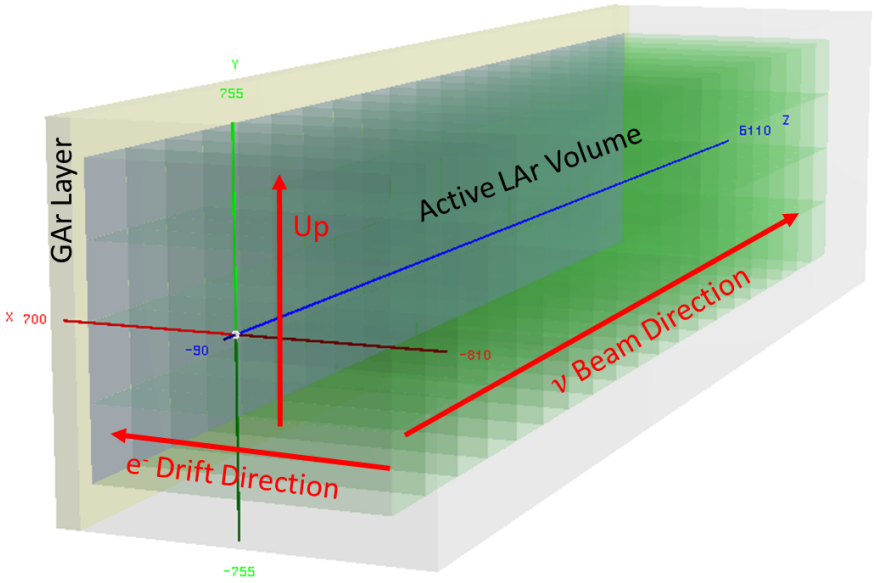

FIG. 84: Illustration of the basic geometry for the 10kt DP TPC implemented in LArSoft. The active volume is in green and surrounding liquid argon buffer volume is in light grey. The drift direction is along x, while the neutrino beam is in the z direction. Each cuboid corresponds to the 3×3 m^2 CRP sub-module with 12 m drift length.

Fig.84 schematically illustrates the first version of the dual-phase 10kt module geometry implemented in LArSoft. The model incorporates the segmentation of the charge readout plane into the 3×3 m^2 CRP sub-units as envisioned in the detector design. In this initial version of the detector geometry, the horizontal x-axis points in the direction of the electron drift, the y-axis is along the vertical, and z-axis is in the neutrino beam direction. Therefore, the charge readout occurs in xz-plane. This unphysical orientation (i.e., the Ar gas layer appears on the side of the detector instead of the top) was due to the internal limitation of the LArSoft framework that required drift field direction to be along $\pm x$-axis. To overcome this problem the geometry service within the framework architecture has been recently substantially extended. Internal assumptions regarding the TPC geometry has been

removed as much as possible and the interface has been generalized to accommodate the requirements imposed by the dual-phase detector. The proper orientation of the dual-phase TPC with the drift along the vertical y-axis has been prepared and successfully tested within the new framework environment. The integration of this geometry description with the event generators and reconstruction algorithms is now on-going.

The charge readout is simulated as a consecutive collection of "wire" planes. This built-in formalism is targeted for the description of the charge readout in a single-phase LAr TPC, where the electron cloud is drifted in liquid argon across the induction views to the collection wires, but does not correspond to the case of the dual-phase detector, where the segmented anode collects charge simultaneously in two orthogonal views in the gaseous phase. Nonetheless, to meet the framework requirement, the CRP anode is modeled as a two thin "wire planes" 0.3 mm thick. A dummy electric field of 4.0 kV/cm ($v_{drift} \sim 3.5$ mm/μs in LAr), the maximal value for which the drift velocity calculation is valid in LArSoft, is applied between the two wire planes in order to allow the drift of electrons from one collection plane to the other. This in effect introduces a small time offset between hits recorded in two collection views given by the electron drift time in the first wire plane:

$$\Delta t = t_{view1} - t_{view0} = \frac{0.3 \text{ mm}}{3.5 \text{ mm}/\mu\text{s}} = 86 \text{ ns}.$$

However, this offset value is small enough compared 2.5 MHz ADC sampling rate (400 ns time bin) of the electronics and at most would correspond to 1 time tick difference in charge arrival times. The evolution of the simplified anode description with the improved handling of detector geometries, recently implemented within the LArSoft architecture and mentioned above in connection to the drift field direction, is foreseen in the future.

The charge amplification performed by the LEMs is modeled in the simulation by scaling true charge recorded on a given readout channel at a given time after taking into account electron lifetime and diffusion effects by the factor that parametrizes the expected gain per each collection view. After multiplying the collected charge by the gain factor the result is convoluted with the front-end amplifier response function and digitized.

The basic checks of spatial and calorimetric reconstruction have been performed with the initial version of the TPC geometry and detector simulation in LArSoft. As a first step the validation of the existing hit finding and hit fitting algorithms in LArSoft was performed. The standard hit reconstruction implemented in LArSoft consists of two steps:

- Deconvolution of the E-field and electronics response,

- Hit finding and fitting with the assumption of Gaussian shape of ionization signals.

The use of the deconvolution for hit reconstruction is motivated by bi-polar nature in the response of induction planes in single-phase LAr TPC detectors. However, due to necessary filtering involved in the deconvolution procedure, the high frequency content (in the Fourier spectrum) of signals can not be recovered leading to loss of information. For the collection view an approach that relies on hit finding and fitting in the time domain (raw waveforms without deconvolution) is also suitable and could be used for the dual-phase detector since both views are operated in collection mode. An implementation of such algorithm hit reconstruction algorithm in LArSoft is under development.

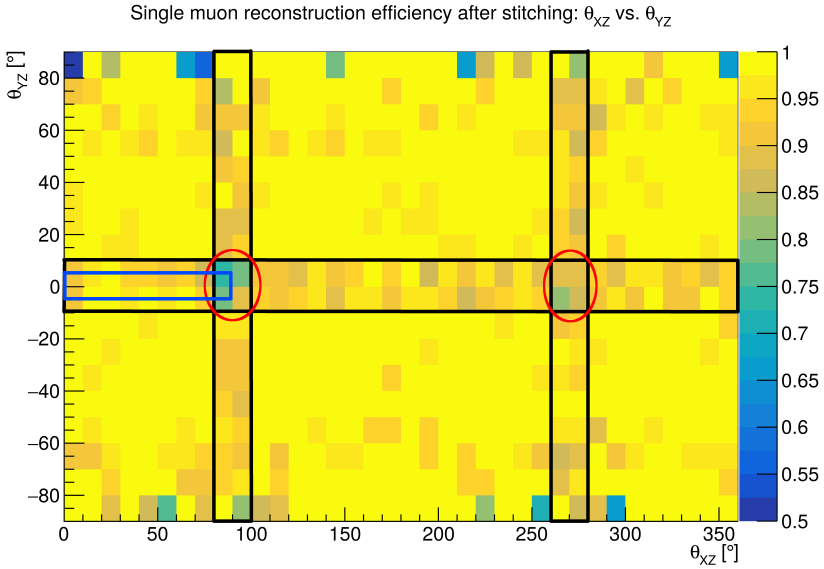

FIG. 85: Trajectory reconstruction efficiency map. There are large errors for large θ_{YZ} due to low statistics. In black boxes muons are seen only in a few channels in one of the views. Red circles show muons along drift directions.

The track reconstruction in LArSoft with the dual-phase geometry has been tested using single muons isotropically emitted within the detector volume. The preliminary results are given in Fig 85 that shows the efficiency of the single track reconstruction algorithm for different muon orientations. The efficiency for single track reconstruction is above 93% with the decreases in the regions corresponding to the problematic directions such as

- isochronous tracks giving a short projection in one of the views,
- tracks with short projection in both views.

No technical problems have been identified within the framework itself.

Studies related to EM shower reconstruction and photon ν_e background rejection are also on-going. As an example, Fig. 86 shows distributions of energy loss from the initial part of the EM cascade

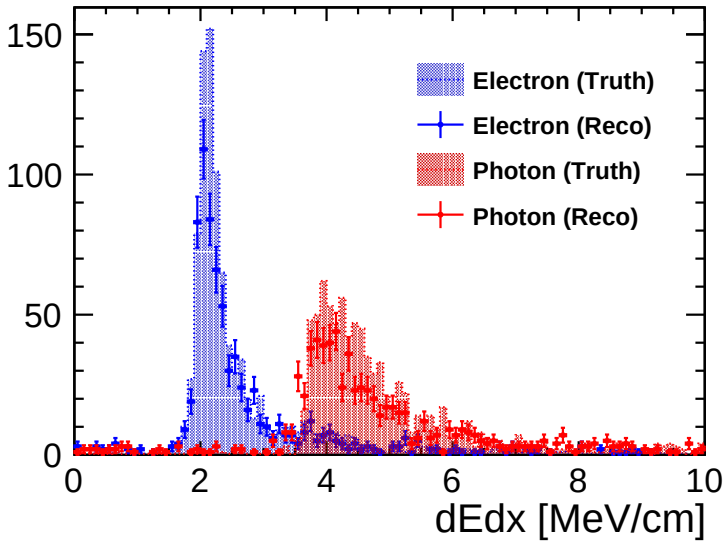

FIG. 86: dE/dx distribution from the initial part of the EM shower for electrons(blue), and photons (red). Points with errors come from the reconstructed direction of the cascade while shaded histograms are obtained with MC truth (cascade starting point and direction) information.

originated by electrons and photons. This dE/dx measured at the beginning of the shower is used to separate the two categories of events.

The CRP readout units of the WA105 detector are identical to those envisioned for the DUNE 10kt module. Therefore, adapting the LArSoft-based simulation developed for the DUNE far detector will not require any substantial effort and allow the WA105 data to be analyzed within the same framework as that used the single-phase prototype.

6 Conclusions

This report documents the large progress achieved since the last SPSC annual review on the dual-phase prototyping activities ongoing at CERN.

Since the end of 2015 WA105 was fully integrated in the DUNE project as dual-phase ProtoDUNE stressing the technological and scientific importance of its programme for the definition of the DUNE 10kt underground modules technology. An EOI call allowed to extend the participation to new groups and to open the way to US participation. Several synergies with single-phase ProtoDUNE have been strengthened during this last year concerning beam instrumentation, high voltage, slow control, field cage and beam-plug, online computing infrastructures and offline computing.

The executive design of dual-phase ProtoDUNE was completed by the end of November 2016. This activity concerned three main detector components such as the Charge Readout Planes, the field cage which is now based on common structural elements as the single-phase field cage and the cathode. The

readout electronics is in production and it has been already implemented on the $3{\times}1{\times}1\,\mathrm{m}^3$ for 1280 channels. A subset of the online storage and processing facility became also operative on the $3{\times}1{\times}1\,\mathrm{m}^3$. The design of the beam-line and of its instrumentation has been completed.

The ProtoDUNE dual-phase cryostat and the EHN1 infrastructure are in an advanced state of installation. The cryostat should become available to start the detector installation by the beginning of June. The clean room in Bldg 185, which has been used by WA104 for the T600 refurbishing, will become available for the pre-assembly of the CRP units of the $6 \times 6 \times 6\mathrm{m}^3$ detector at the beginning of April.

Software and analysis activities also largely progressed with the preparation of a full online and offline environment related to the $3{\times}1{\times}1\,\mathrm{m}^3$ detector data-taking

A major activity in 2016 was the integration of the $3{\times}1{\times}1\,\mathrm{m}^3$ setup in Blg. 182. The $3{\times}1{\times}1\,\mathrm{m}^3$ detector was inserted in its cryostat in July 2016. Its commissioning and operation originally foreseen by the fall of 2016 has been delayed by the installation and commissioning of the cryogenic system and then by a problem occurred on the cryostat. Under responsibility of the CERN Neutrino Platform, the solution to the cryostat problem and the timescale for successful cryogenic commissioning of the $3{\times}1{\times}1\,\mathrm{m}^3$ are on the critical path for further progress on the characterisation of the Dual Phase technology.

Nonetheless, the experience acquired with the $3{\times}1{\times}1\,\mathrm{m}^3$ integration has allowed improving a wide range of technical issues related to the $6{\times}6{\times}6\mathrm{m}^3$ detector. The construction procedures of the $6{\times}6{\times}6\mathrm{m}^3$ have been refined by taking into account the final executive design. A revised installation schedule of the $6 \times 6 \times 6\mathrm{m}^3$ has been defined by taking into account these elements and the latest input from the Neutrino Platform on the installation of the cryostat and the cryogenic infrastructure. Production and installation activities are starting and there are good prospects to have the $6 \times 6 \times 6\mathrm{m}^3$ detector to be ready in 2018, in order to take beam data before the LHC LS2.

The final beam-line simulations are compatible with the beam requests formulated for 2018 in the 2016 annual report to the SPSC. By taking into account this fact and the refined installation schedule the beam requests formulated last year are confirmed also in this report. Similarly as single-phase ProtoDUNE [13], we foresee a continuation of the running activity with cosmic rays during LS2 and a possible continuation of the beam data taking after LS2 in order to complete the beam data sample, address additional issues emerging from the analysis of the data sample collected during 2018 and assess the long term detector stability.

We thank the CERN Management, the CERN Departments, the Neutrino Platform, and FNAL for their support. We thank the CERN IT division for their collaboration and continuous support

concerning the prototype online computing farm for the $3{\times}1{\times}1\,\mathrm{m}^3$ in Blg 182.

[1] **DUNE** Collaboration, R. Acciarri *et al.*, "Long-Baseline Neutrino Facility (LBNF) and Deep Underground Neutrino Experiment (DUNE) Conceptual Design Report, Volume 4 The DUNE Detectors at LBNF," arXiv:1601.02984 [physics.ins-det].

[2] **WA105 Collaboration** Collaboration, G. Balik, "Yearly progress report on WA105/ProtoDUNE dual phase (2016)," Tech. Rep. CERN-SPSC-2016-017. SPSC-SR-184, CERN, Geneva, Apr, 2016. https://cds.cern.ch/record/2144856.

[3] C. Cantini, L. Epprecht, A. Gendotti, S. Horikawa, S. Murphy, *et al.*, "Long-term operation of a double phase lar lem time projection chamber with a simplified anode and extraction-grid design," *JINST* **9** (2014) P03017, arXiv:1312.6487 [physics.ins-det].

[4] C. Cantini, L. Epprecht, A. Gendotti, S. Horikawa, L. Periale, *et al.*, "Performance study of the effective gain of the double phase liquid Argon LEM Time Projection Chamber," arXiv:1412.4402 [physics.ins-det]. accepted for publication in JINST.

[5] **WA105** Collaboration, G. B. *et al.*, "Progress report on LBNO-DEMO/WA105 (2015).". CERN-SPSC-2015-013 / SPSC SR-158 (2015).

[6] D. Mergelkuhl, "Wa105 - 2nd cold test of 1x3 crp frame cern." https://edms.cern.ch/document/1608827/1/TAB3.

[7] C. Cantini *et al.*, "First test of a high voltage feedthrough for liquid Argon TPCs connected to a 300 kV power supply," arXiv:1611.02085 [physics.ins-det]. Accepted for publication in JINST.

[8] https://edms.cern.ch/document/1765625/1. 3x1x1 Cryognic piping and instrumentation diagram.

[9] D. Montanari, M. Adamowski, A. Hahn, B. Norris, J. Reichenbacher, R. Rucinski, J. Stewart, and T. Tope, "Performance and Results of the LBNE 35 Ton Membrane Cryostat Prototype," *Phys. Procedia* **67** (2015) 308–313.

[10] M. Auger *et al.*, "A Novel Cosmic Ray Tagger System for Liquid Argon TPC Neutrino Detectors," arXiv:1612.04614 [physics.ins-det].

[11] M. Auger, A. Ereditato, D. Goeldi, I. Kreslo, D. Lorca, M. Luethi, C. R. von Rohr, J. Sinclair, and M. S. Weber, "Multi-channel front-end board for SiPM readout," *JINST* **11** no. 10, (2016) P10005, arXiv:1606.02290 [physics.ins-det].

[12] V.Boccone *et al.*, *Light Readout for a 1 ton Liquid Argon Dark Matter Detector*. PhD thesis, 2010. http://cds.cern.ch/record/1276774.

[13] M. Thomson, "Protodune-sp operations: Briefing document.". Note sent on behalf of the DUNE collaboration to the SPSC Committee on 22/2/2017.

[14] E. Grace and J. A. Nikkel, "Index of refraction, Rayleigh scattering length, and Sellmeier coefficients in solid and liquid argon and xenon," arXiv:1502.04213.

[15] N. Ishida *et al.*, "Attenuation length measurements of scintillation light in liquid rare gases and their mixtures using an improved reflection suppresser," *Nucl. Instrum. Meth.* **A384** (1997) 380.

[16] **WA105** Collaboration, G. B. *et al.*, "Progress report on LBNO-DEMO/WA105 (2016).".

CERN-SPSC-2016-017 / SPSC SR-184 (2016).